DESIGN AND SYNTHESIS OF METAL ORGANIC FRAMEWORKS FOR ENERGY RELATED APPLICATIONS

by

QIHAN GONG

A dissertation submitted to the

Graduate School – New Brunswick

Rutgers, The State University of New Jersey

In partial fulfillment of the requirements

For the degree of

Doctor of Philosophy

Graduate Program in Chemistry and Chemical Biology

Written under the direction of

Jing Li

And approved by

_____

_____

_____

_____

New Brunswick, New Jersey

October 2014

ABSTRACT OF THE DISSERTATION

Design and Synthesis of Metal Organic Frameworks for Energy Related Applications

by

QIHAN GONG

Dissertation Director:

Jing Li

Metal organic frameworks (MOFs), also known as porous coordination polymers (PCPs), are frameworks composed of metallic centers and multidentate organic ligands. In this thesis, the author focuses mainly on synthesizing new MOFs as yellow phosphors for white light emitting diodes (WLEDs) and the study of their adsorption properties for gas storage and separation.

A critical aspect in the research and development of white light-emitting diodes (WLEDs) is the discovery of highly efficient phosphors free of rare-earth elements. In chapter 2 and 3, the author has designed and synthesized a new type of rare-earth-free, blue-excitable yellow phosphors, obtained by combining a strongly emissive molecular fluorophore with a second linker as a bandgap modulating co-ligand, in three-

dimensional networks. Compound **1** $[Zn_6(btc)_4(tppe)_2(DMA)_2]$ (btc = benzene-1,3,5-tricarboxylate, tppe = 1,1,2,2-tetrakis(4-(pyridin-4-yl)phenyl)ethene, DMA = dimethylacetamide) and compound **2** are both composed of zinc metal center, btc and tppe linkers, but with different structures. Compound **1** contains both primary building unit (PBU) and secondary building unit (SBU), while **2** is constructed on two different primary building units (PBUs). Compound **3** is made of zinc metal center, fdc and tppe linkers (fdc=9-Fluorenone-2,7-dicarboxylate). All three compounds (air stable sample of **1**, outgassed samples of **2** and **3**) emit bright yellow light (540, 535, 540 nm for **1**, **2** and **3** respectively) when excited by a blue light source. These studies show that the title compounds represent a promising series for use in phosphor-conversion WLEDs.

Gas adsorption and separation is another important application of MOFs as mentioned previously. Commensurate adsorption is an interesting phenomenon, in which the location and orientation of adsorbates are commensurate to the crystal symmetry of adsorbents. Commensurate adsorption is helpful to understand the interaction between adsorbates and adsorbents and usually indicates high selectivity of commensurate adsorbed molecules over incommensurate ones. In chapter 4, the commensurate to incommensurate transition of hydrocarbons (C2 to n-C7 alkanes/alkene) adsorptions on Ca(sdb) has been investigated by simulation, adsorption and single crystal analyses, conducted by author and collaborator. The commensurate adsorption of selected hydrocarbons on $[Zn_2(bpdc)_2(bpe)]\cdot 2DMF$ was studied as well in Chapter 4 by both simulation and adsorption methods.

Acknowledgement

Firstly, I would like to thank my advisor Prof. Jing Li. I read a lot of stories about scientists when I was a kid, thus I always wanted to become a researcher in order to make some contributions to the scientific society. However, I didn't understand the real meaning of science and research until I joined Prof. Li's group and had her valuable guidance and advice. She has made every effort to discover new things to improve the industrial processes and benefit society, or carry out in-depth studies of fundamental phenomenon. She is passionate, diligent and earnest as she strives toward her aims. Under her influence, I gradually realized even small progress and discovery need lots of efforts, including comprehensive background knowledge, critical thinking, novel ideas and hard work. I think the spirit I learned from her will benefit my whole life.

Secondly I would like to thank my committee members Prof. Ki-Bum Lee, Prof. Tewodros Asefa, and Dr. Long Pan. Prof. Ki-Bum Lee and Prof. Tewodros Asefa have given me valuable guidance in my OFRP and IFRP, which helped me to improve my research. Dr. Long Pan has provided me with ideas and advices which mean a lot to me.

Also I would like to thank all of our previous and current group members. Specially thank Dr. David Olson and Dr. Haohan Wu who have taught and trained me to operate adsorption equipment. Thanks to Dr. Sujing Wang who trained me in organic synthesis and purification. Thank Dr. Debasis Banerjee and Dr. Kecai Xiong for helping me solve my crystals structures. Also I would like to thank all of the graduate and

undergraduate students who worked with me: Nathan Rudd, Allison Dyevoich, Brianna Mussman and Song Liu.

I would like to especially thank all of my friends in Rutgers. They are Qing Gu, Zhijuan Zhang, Hao Wang, Jingming Zhang, Wei Liu, Yang Fang, Kun Xu, Feng Xu, Dr. Litao An, Dan Su and Amiee Luan. Thanks for all of their help and encouragement.

I am also very grateful to my parents and my sister, my brother-in-law and my nephew for all of their love and support. My parents have sacrificed a lot to support my studies and research in the past twenty years, and I hope they are proud of me.

Lastly I would like to thank my husband, Xiao Zhang, for his constant support and encouragement. It is because of him that I have the faith and courage to overcome the difficulties in both research and life.

Contents

List of tables

List of illustrations

1. Introduction.

Metal organic frameworks (MOFs), also known as porous coordination polymers (PCPs), are frameworks composed of metallic centers and multidentate organic ligands. The discovery of a few coordination clusters, such as $Ni(4\text{-Me-pyridine})_4(NCS)_2$ for gas adsorption in 1969, initiated the idea of using metal-organic coordination bonds to form porous materials.[1] In 1990s, the synthesis of a few new infinite coordination polymers by Prof. Richard Robson popularized the construction of such porous materials via coordination polymerization.[1-3]

Since then, the study of MOFs has experienced an unparalleled growth. The combination of metal ions and organic linker leads to almost unlimited structures. Till now, more than ten thousands of MOFs have been synthesized and studied, while applications of those MOFs have also been discovered and investigated, such as the potential application in the area of catalysis,[4-6] chemical sensing,[7,8], energy storage and conversion,[9-11] drug delivery and bio-imaging[12-14] and optoelectronics (ferroelectronics,[15] non-linear optics,[16] and LEDs[17]). In this dissertation, two important properties (luminescence and adsorption properties) of MOFs will be discussed.

1.1 Synthesis and structure of MOFs.

Conventional methods used to synthesize MOFs include solvothermal process, where the reactions take place in closed vessels under autogenous pressure; and

nonsolvothermal method, in which the reactions take place under ambient pressure.[18] Alternative routes such as microwave-assisted method, electrochemical method, mechanochemical method and sonochemical method have also been used to synthesize MOFs.[18] Different methods will form MOFs with different size and morphologies.

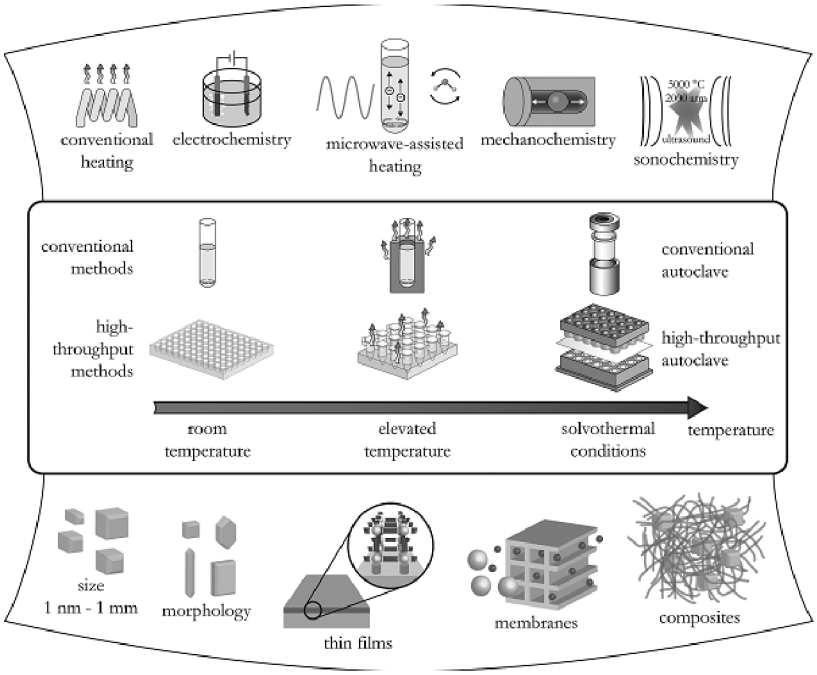

Figure 1. Synthesis method, possible temperatures and final products. Reprinted with permission from Ref 18. Copyright@ (2012) American Chemical Society.

Solvothermal method is important for MOFs synthesis, as it is a powerful technique to grow single crystals, which is critical for MOFs' structural determination and analysis. It is very difficult to interpret the properties of MOFs without knowing their crystal structures. Thus growing single crystals is one of the most important aspects in MOF synthesis. Usually the metal salts and organic linkers are dissolved in

proper solvents and the structure-directing agents or mineralizers are added in the solution to assistant crystal growth. A few parameters will affect the crystal growth including but not limited to 1) the concentration and ratio of the metal salts and organic linkers; 2) the proper major solvent, the solubility of starting material in the solvent is important; 3) the polarity of the solvent, which could be adjusted by adding a smaller portion of a second solvent; 4) the chosen of mineralizers, which are used to increase the crystallinity of the final product; 5) the temperature, reaction time and cooling down rate. In the process of crystal growth, very small aspect of those parameters may affect the size, quality and even phase of the outcome crystals.

Diffusion method at room temperature is another powerful method to grow single crystals. Usually, the starting materials are dissolved separately in two solvent layers in an open tube. After sitting at room temperature for a few days, crystals will grow in the interface of the two layers. Choosing proper solvents for each layer and the concentration of starting material in each solvent are the two major aspects to affect the final product.

Based on different synthesis methods, MOFs with different topologies and dimensions such as one dimensional (1D), two dimensional (2D) and three dimensional (3D) structures could be formed. The structures of MOFs are built up on the metal ion/cluster nodes and organic linkers which connect the nodes. Figure 2 illustrated the possible combinations of metal ions with different coordination sites and the

polydentate organic ligands to form 1D, 2D and 3D MOFs.[19] Figure 3 shows examples of the rigid organic ligands which are polydentate. Both carboxylate linkers and N-terminated linkers are listed. Carboxylate linkers are commonly used in MOFs structures, as the negative charges in carboxylate linkers could balance the positive charges from metal ions. Neutral N-terminated linkers always serve as the second linker besides carboxylate linkers, for example, in pillar-layered MOFs structures.

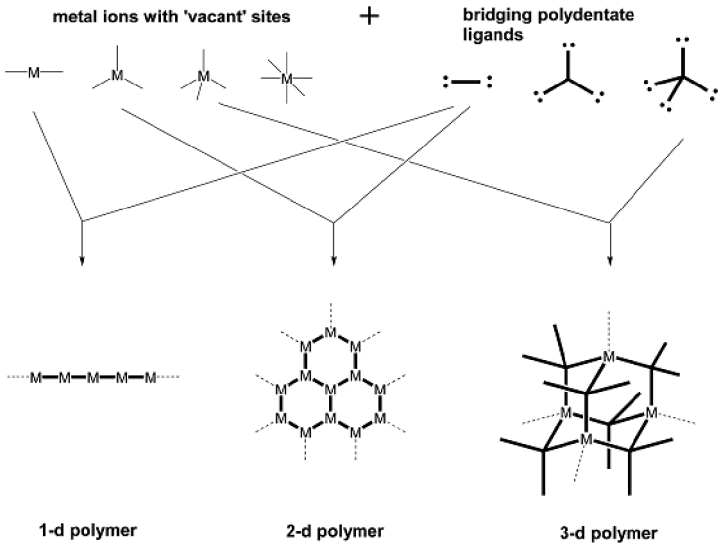

Figure 2. The building block, or 'modular', principle behind forming coordination polymers. Reprinted with permission from Ref 19. Copyright @2003 Royal Society of Chemistry.

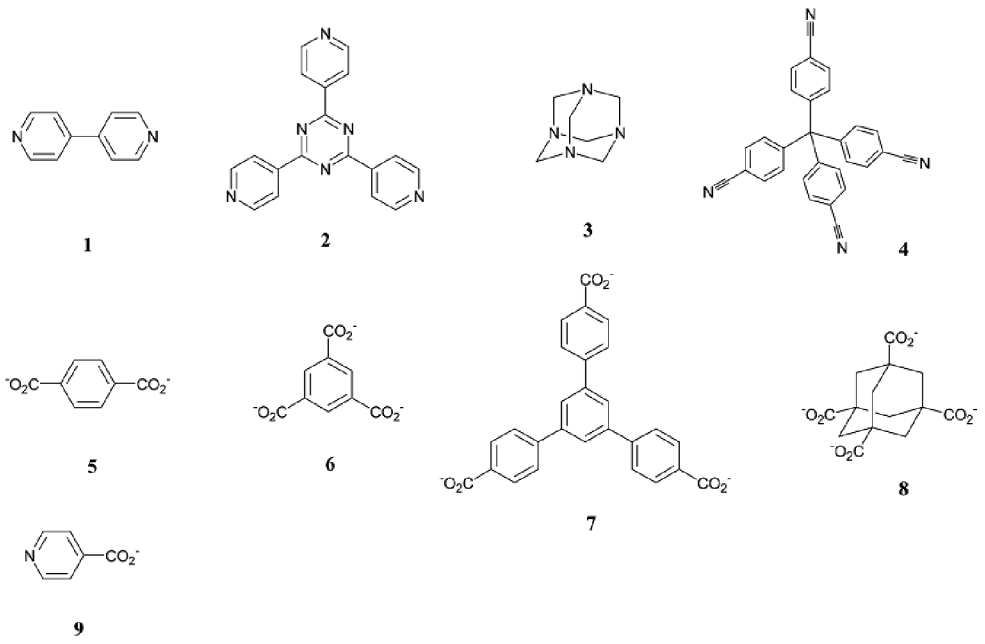

Figure 3. Examples of rigid ligands used in the synthesis of coordination polymers. Reprinted with permission from Ref 19. Copyright @2003 Royal Society of Chemistry.

The metal ions in Figure 2 could be replaced by metal building blocks, including metal ions, metal cluster and metal-organic molecules[20] (Figure 4). As shown in Figure 4, A is the building block composed of single metal ion, also called primary building unit (PBU), B is composed of several metal ions, which is called secondary building unit (SBU), and C is constructed by several SBU and named as super building blocks (SBB). PBU, SBU and SBB are three normal basic building blocks for MOFs, in which paddle-wheel building unit is one of the most common SBU. In a paddle-wheel building unit, the coordination geometry for each metal is square pyramidal. Two metal atoms share four carboxylate groups of the organic ligands located in the equatorial plane to form a

paddlewheel-shaped motif. Each metal atom coordinates to another molecule apically, which could be either a monodentate terminal molecule or polydentate molecule.

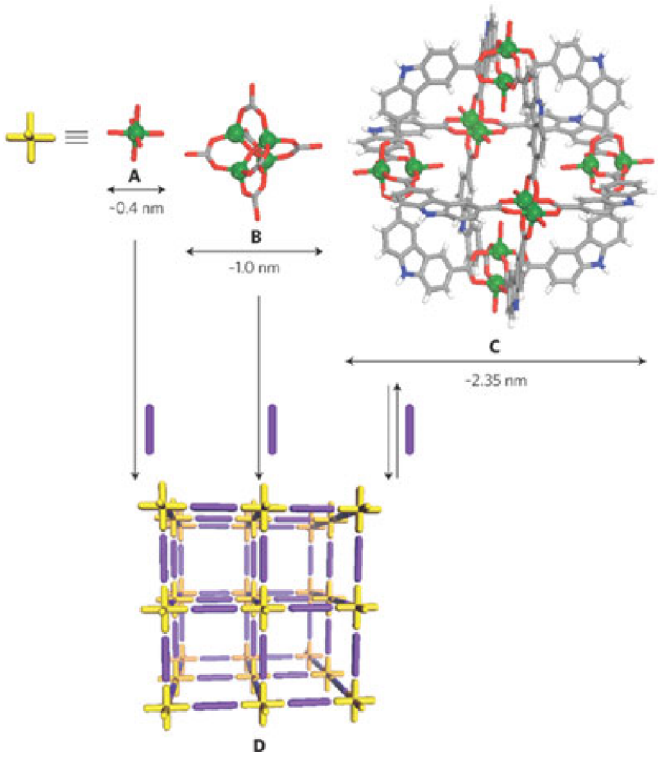

Figure 4. Porous primitive cubic networks (D) can be generated by combining linear ligands (purple spacers) with a diverse range of octahedral building blocks (yellow clusters) such as metal cations (A), metal clusters (B) or octahedral metal–organic molecules (C) (metal, green; oxygen, red; nitrogen, blue; carbon, grey; hydrogen, white). Polyhedral building blocks such as C offer a high level of control over the resulting structure, dimensions of several nanometers and, for the first time, can be assembled in a reversible fashion through a stepwise process. Reprinted with permission from Ref 20. Copyright @2009 Nature Publishing Group.

The as synthesized MOFs generally have pores, also called void space, with solvent occupation, which are named as "guest molecules". The guest molecules need to be removed by either direct heating or evacuation for most applications. However, many

MOF structures collapse upon the removal of guest molecules. Solvent exchange may be carried out to replace the original high boiling point solvents in the pores with low boiling point solvents, so that their removal can be accomplished at lower temperature to achieve permanent porosity while keeping the structure intact.

1.2 Characterization of MOFs.

1.2.1 General characterization methods for MOFs

Single crystal X-ray diffraction study is an essential tool to identify the molecular structure of MOFs. High quality single crystals with sufficient size are required to gain high quality diffraction pattern and then solve the single crystal structure. Synchrotron radiation provides brightest X-ray beams generated by synchrotron to collect higher resolution diffraction patterns for crystals with dimensions larger than 50 μm.

Powder X-ray diffraction (PXRD) measurement is used to confirm the phase purity and integrity of powder material. By comparing the PXRD patterns of powder sample and simulated PXRD calculated from single crystal data, the phase purity and integrity of powder sample could be examined.

Thermogravimetric analysis (TGA) is a measurement to inspect the thermal stability of structures. As mentioned in the previous section, the as-synthesized MOFs usually have guest molecules encapsulated in the pores of structures. The guest molecules leave the structure upon heating, causing the weight loss in TGA curves. The

weight loss percentage can calculated to determine the amount of guest molecules in the structure.

For specific applications, various characterization methods will be applied to study the particular properties of MOFs.

1.2.2 Characterization methods for MOFs with luminescence properties

The luminescence properties can be characterized by several techniques. For example, photoluminescence excitation and emission experiments are the basic characterization methods for luminescent MOFs. The maximum emission from the emission spectrum excited at a certain wavelength is an important parameter to estimate the color of light emitted. The excitation spectrum monitored at a certain emission wavelength provides the optimized excitation wavelength information.

Photoluminescence quantum efficiency is assessed by both internal and external quantum yield. Internal quantum yield is defined as the ratio of the number of fluorescent photons to the number of the absorbed excitation photons. External quantum yield is defined as the ratio of the number of fluorescent photons to the number of the irradiated excitation photons.[21,22]

Lifetime of a photoluminescence process refers to the average time the molecule stays in its excited state before returning back to the ground state. Lifetime is reciprocally proportional to the sum of rate constants of a radiative and nonradiative processes.[23,24]

UV-Vis diffuse reflectance experiments are performed to estimate the absorption capability and band gap of a MOF sample. As MOFs are materials for which solid state properties are mostly considered, UV-Vis diffuse reflectance spectra are used instead of solution based UV-Vis absorption spectra. The obtained reflectance spectra are converted to Kubelka-Munk function,[25,26] which correlates to the absorption intensity, as a function of wavelength. The band gap of the compound can be estimated from the Kubelka-Munk function.

Commission International de I'Eclairage (CIE) coordinates is calculated from a PL spectrum and used to specify how the human eye will experience the light with the given PL emission spectrum.[27] As shown in Figure 5, the outer curved boundary is the spectral (or monochromatic) locus, with wavelengths shown in nanometers.[28] White light corresponds to the point (x, y)= (1/3, 1/3).

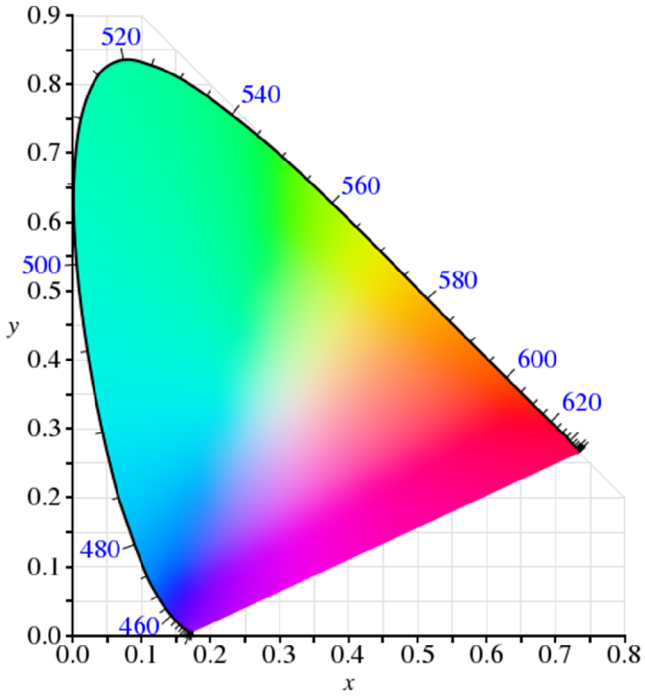

Figure 5. The CIE 1931 color space chromaticity diagram.

1.2.3 Characterization methods for MOFs with gas adsorption properties

MOFs that possess permanent pores, indicated by the integrity of structure after removal of guest molecules usually exhibit interesting adsorption properties and are good candidates for applications in gas storage or separation. In order to study their adsorption properties, surface area and porosity have to be measured first. N_2 adsorption isotherms at 77 K, (or Ar adsorption at 87 K, CO_2 adsorption at 195 K) are usually used to calculate pore size distribution and surface area of the material. According to different adsorption model, the surface area can be calculated using

Brunauer-Emmett-Teller (BET) and/or Langmuir model. The former uses multilayer adsorption model and the latter uses monolayer adsorption model.

To study the adsorption properties of a MOF material adsorption-desorption isotherms of selectedadsorbates are measured. The uptake of a given adsorbate on a MOF adsorbent is a function of the pressure at a specific temperature. The overlap of adsorption and desorption isotherms indicate the process is reversible and have reached equilibrium. The Henry constant, from the linear region of the isotherm, could be calculated according to the Henry equation which corresponds to the interaction of adsorbate and adsorbent at low loading. From the isotherms at different temperature, the steric heat of adsorption could be calculated by different methods, which estimates the interaction between the adsorbate and adsorbent.

Adsorption simulation is another important tool to study adsorption behavior and mechanism in-depth. Cerius 2 software provides a package to simulate single component adsorption on a given crystal structure modeled by grand canonical Monte Carlo (GCMC) simulations. After the single crystal structure of the adsorbent and the optimized molecular structure of the adsorbate are loaded in the software, the adsorption simulation can be carried out at a given pressure and temperature with different force field and equilibrium steps to choose. The simulation data can be used to predict the adsorption uptake, the location and orientation of the adsorbates and the

heat of adsorption, which provide important information to compare to the experimental data, thus help to understand the adsorption process.

1.3 MOFs as phosphors for WLEDs.

Luminescence is an important property possessed by some MOFs which has been intensively explored. Traditional inorganic and organic luminescent materials have been commercialized in various fields such as lighting, display, sensing and optical devices.[29-31] The inorganic luminescent materials are usually rare-earth ions doped oxides, sulfides, oxysulfides, oxynitrides or nitrides, in which the rare-earth ions provide the narrow emission and high color purity lights.[31] The luminescent properties of inorganic luminescent materials are affected by the atomic structure, homogeneity in composition, particle size, defect, microstructure, and interface.[31] The organic luminescent materials are n-type and p-type electroluminescent organic materials, which have been studied and intended to be applied in organic light emitting diode devices since the invention of OLED in 1980.[30-32] Compared to traditional inorganic and organic luminescent materials, metal organic frameworks are a new type of luminescent material in which both the inorganic moieties and organic moieties may provide source of luminescence. During the process of exploring new MOFs, thousands of new structures with various metal ions, abundant organic ligands and plentiful coordination types have been discovered and synthesized. In order to modify and tune the

luminescent properties of MOFs, the origin of the luminescence of MOFs needs to be studied first.

1.3.1 Origin of the luminescence in MOFs.

Luminescence, contains fluorescence and phosphorescence, is the phenomenon where photons are generated after the absorption of non-heat based energy. The difference between fluorescence and phosphorescence lies in the type of transition, while the spin-allowed radiative transition happens in the former luminescence, the spin-forbidden radiative transition happens in the latter one.[8,23,31] Photoluminescence is the luminescent process which is initiated by the absorption of photons. As mentioned earlier, considerable amount of luminescent MOFs have been synthesized and reported up to date. The origin of luminescence in MOFs is majorly from organic ligands, metal ions and charge transfer between metal and ligands.[23]

In order to obtain rigid structure of MOFs, π-conjugated organic ligands are commonly used to serve as pillars of MOFs. The bulky π-conjugated ligands are usually photoluminescent with emissions arising from the $\pi^* \rightarrow \pi$ or $\pi^* \rightarrow$n transitions. Compared to free ligands, the optical properties of the ligands in MOFs are often different because of the reduced nonradiative decay rate attributed to their stabilization in MOFs.[8,23] The stronger molecular interactions and the arrangement of the ligands in MOFs, and the perturbation from metal ions are all factors that would change the fluorescence properties of the π-conjugated linkers.[23]

Besides the organic ligand-based photoluminescent MOFs, a large portion of luminescent MOFs are metal-centered, especially the lanthanide based luminescent MOFs. Lanthanides ions (Ln^{3+}) are metal ions contain electrons on 4f orbitals. The electronic configurations of lanthanides ions produce a series of special electronic energy levels, which lead to distinguishing transitions between them.

Charge transfer luminescent arises from the transition of excited state, which comes from charge transfer, to the ground state. The following schemes show the general mechanism of two charge transfer forms, metal to ligand charge transfer (MLCT) and ligand to metal charge transfer (LMCT) in an octahedral complex.[33] MLCT involves in the electron transition from a metal ion orbital to an organic ligand based orbital, while LMCT involves in a reverse process. If the MOF emission has a large shift compared to the bulk organic ligand, then the origin of luminescence is mostly charge transfer.

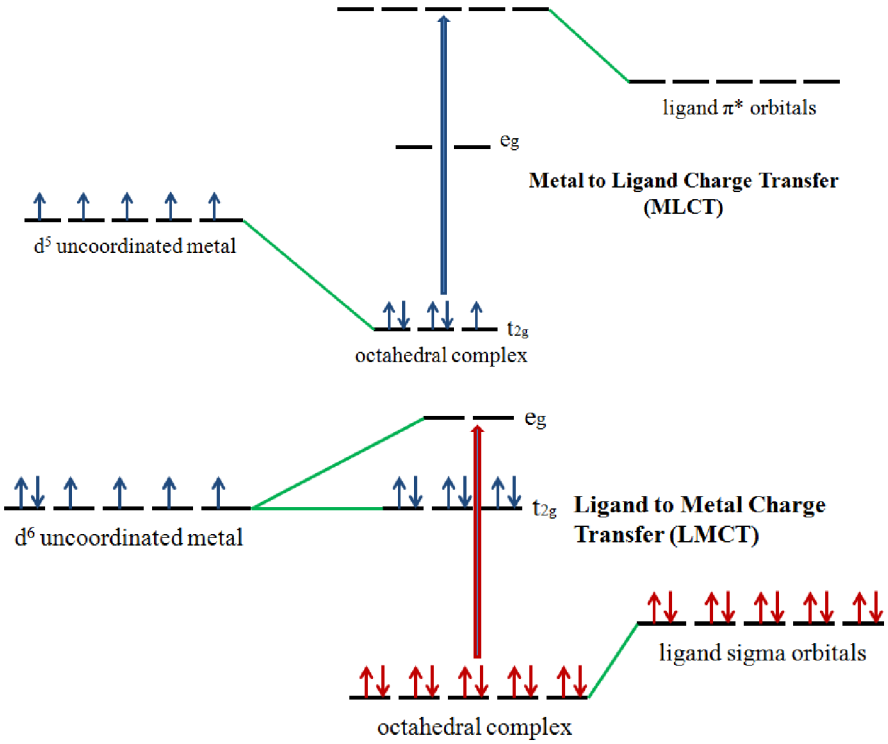

Figure 6. Scheme of ligand to metal charge transfer and metal to ligand charge transfer in an octahedral complex of a transition metal. Reprinted with permission from UCDavis ChemWiKi. Copyright @ Creative Commons Attribution-Noncommercial-Share Alike 3.0 United States License.

1.3.2 Phosphors for light-emitting devices.

Luminescent MOFs have been largely investigated for their applications in various areas such as chemical sensing, light-emitting devices, cell imaging and drug delivery in biomedicine. The tunable emissions from MOFs make them excellent candidates for light-emitting devices.

In 1907, H. J. Round published on the very first light emitting diode (LED) in which light emitted from a silion carbide junction diode. However, it was not until 1962

that the first practical visible spectrum LED was developed, by Nick Holonyak at General Electric.[34] Around 1995, LEDs with high brightness and blue emission were fabricated and the LEDs for general lighting were then developed.[34] Solid-state lighting (SSL) technologies, primarily light-emitting diodes (LEDs) and organic light-emitting diodes (OLEDs), have experienced very rapid growth after that because of their considerable utility in general lighting and display devices.[30,32,35] With smaller size, more robust material, more environmental friendly and super energy saving potential (lower energy consumptions, low maintenance, higher efficiencies, and longer lifetimes), white light - emitting diodes (WLEDs), are gradually replacing incandescent and fluorescent lamps. Table 1 shows the comparison of incandescent lamp, compact fluorescent lamp and LED lamp, in which 1 LED lamp equals 3 CFL lamps or 22 incandescent lamps.[36]

Table 1. Comparison of IND, CFL and LED lamps[36]

	Incandescent lamp (IND)	Compact fluorescent lamp (CFL)	Light emitting diode lamp (LED)
Power (Watt)	60	15	12.5
Luminous flux (Lumens)	900	900	800
Lifetime (hs)	1,000	8,500	25,000
Equivalent lamps	22	3	1

LEDs emit nearly monochromatic light, which is not inherently white light. Common approaches to fabricate WLEDs include (Figure 7): (a) phosphor-conversion (PC), in which white light is produced from the combined emissions of a phosphor coated on and excited by an LED chip. The combinations can be either a yellow-emitting phosphor on a blue LED chip,[37,38] a multicomponent phosphor (e.g. mixture of red-, green-, and blue-emitting material) on a UV (or near UV) chip[39], or a white-emitting phosphor on a UV chip. [40,41] (b) multi-chip combination, where three primary colored LED chips, namely red, green, and blue (RGB) diodes are used to generate white light.[42] And (c) A hybrid method, which uses both phosphor-converted and monochromatic LEDs.[43]

WLEDs composed of blue LED chips coated with yellow phosphors are mostly commercially available, compared to other WLEDs. For example, WLEDs combined with primary colored (red, green and blue) LED chips are far more expensive; and WLEDs composed of ultraviolet (UV) LED chips coated with multi-phosphors (a mixture of red, green and blue phosphors) or white phosphors are associated with lower theoretical efficacy, higher input energy and cost compared to blue chip WLEDs, and possible leak UV radiation.[44,45]

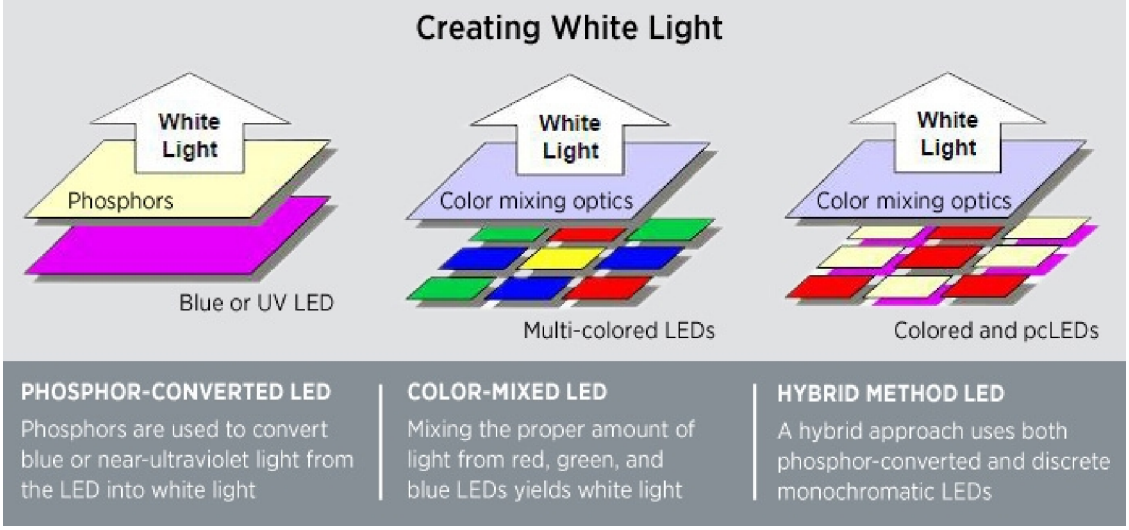

Figure 7. Scheme of creating white light with LEDs. Reprinted with permission from Department of Energy. Copyright @ Department of Energy.

In order to fabricate blue-chips based WLEDs, yellow phosphors excited with blue range light are required. There are only limited numbers of phosphor materials which could meet the requirement of this wavelength conversion. At present time, essentially all commercial yellow phosphors are rare-earth (RE) ions doped oxides, sulfides, oxysulfides, oxynitrides or nitrides (Table 2), in which the RE metals, such as europium, terbium and yttrium play a crucial role in controlling their light color and quality.[34,46] Cerium doped yttrium aluminum garnet (YAG: Ce^{3+}) is one of the well-known commercial yellow phosphors.

Table 2. Yellow Phosphors for LEDs

Host	Dopant	Conc (%)	λ_{em} (nm)	QE (int/ext)
$Y_3Al_5O_{12}$	Ce^{3+}	0.033	536	>90/-
		3.33	558	81/-
$SrGa_2S_4$	Eu^{2+}	0.1	537	57/-
Sr_3SiO_5	Eu^{2+}	7	568	-/68
$Ba_2Si_5N_8$	Eu^{2+}	2	570	75-80/-
$BaYSi_4N_7$	Eu^{2+}	1	520	16/11
$SrYSi_4N_7$	Eu^{2+}	1	534	26/19
$CaSi_2O_2N_2$	Eu^{2+}	2	560	76/-
$SrSi_2O_2N_2$	Eu^{2+}	2	537	91/-
α-SiAlOH	Yb^{2+}	0.5	550	58/26
α-SiAlOH	Eu^{2+}	7	567	71/88
β-SiAlOH	Eu^{2+}	0.3	536	49/33
Ca-α-SiAlOH	Eu^{2+}	5	580	-/44
Li-α-SiAlOH	Eu^{2+}	7	573	57/40

1.3.3 MOFs as phosphors for white light emitting diodes.

As discussed in section 1.1, thousands of luminescent MOFs have been synthesized and reported in the past decades. Among many studies concerning potential applications of luminescent MOFs, their possible utility as phosphors for white light emitting diodes (WLEDs) has also been evaluated by several research groups. For example, the first RE-free, white-emitting MOF phosphor was reported in 2009. Other noteworthy examples include Eu^{2+} and Eu^{3+} doped yellow-emitting homoleptic imidazolates and white-emitting [La(mbdc)(stp)], as well as several LnMOFs that emit white light.

Table 3. Selected optical properties of MOF white and yellow phosphors

Ref	Formula	λ_{ex} (nm)	λ_{em} (nm)	Color	CIE Coordinates	QE (int/ext)
47	$[AgL]_n \cdot nH_2O$	330	566	yellow	-	-
	L=4-cyanobenzoate	349	427	white	(0.33, 0.34)	-/10.86
48	PbL1[a]	365	531	yellow	(0.31, 0.42)	-
	PbL2[b]	320-420	459	white	(0.24, 0.48)[c]	2-3/-
49	Zn(L) (Hbtc)·$(H_2O)_2$[d]	373	424, 539	white	(0.29, 0.34)	-
50	$In(btb)_{2/3}(oa)(DEF)_{3/2}$	365	-	white	-	-
17	$[Ir(ppy)_2(bpy)]^+$@**1**[e]	370	425, 530	white	(0.31, 0.33)[f]	20.4/-
51	Gd-L1-L2[g]	370	-	white	-	-
52	$Dy_{0.02}Eu_{0.05}Gd_{0.93}L$[h]	290	-	white	(0.355, 0.313)	-/-

[53]	Tb^{3+} and Eu^{3+} doped $La_2(pda)_3(H_2O)_5$[i]	312	408, 543, 614	white	(0.327, 0.312)	6.11/-
[54]	Eu^{3+} doped 2-Tb[j]	330	-	white	(0.330, 0.328)	11.4/-
[55]	2- Eu-Ag[k]	310	-	white	(0.42, 0.32)	-
[56]	[3][$Ba(Im)_2$]:Eu^{2+}	365	560	yellow	(0.433, 0.516)	32/-
[57]	$(Me_2NH_2)[RbCd_4(oba)_5]\cdot H_2O$	312	427, 566	white	(0.30, 0.33)	3.1[l]/-
[58]	$[Ln(dpdc)_{1.5}(ip)(H_2O)]_n$[m]	394	-	white	(0.332, 0.334)	1.67/-
[59]	Eu3+ doped [La(mbdc)(stp)] [n]	390		white		12/-

[a] L1= 2,5-bis(2-(methylthio)ethylthio)terephthalic acid
[b] L2=(S,S)-2,5-Bis-(2-hydroxypropylsulfanyl)-terephthalic acid
[c] λ_{ex} = 400 nm
[d] L= N^4,$N^{4'}$-di(pyridin-4-yl)biphenyl-4,4'-dicarboxamide
[e] **1**=$[(CH_3)_2NH_2]_{15}[(Cd_2Cl)_3(tatpt)_4]\cdot 12DMF\cdot 8H_2O$
[f] Measured at $[Ir(ppy)_2(bpy)]^+$ encapsulation percentage with 3.5%
[g] L2 doped $Ln_2(L1)_3\cdot(DMF)_x\cdot(H_2O)_y$ (x , y = 1–2)
[h] H_3L=4,4'-((2-((4-carboxyphenoxy)methyl)-2-methy-lpropane-1,3-diyl)bis(oxy))dibenzoic acid
[i] pda=pyridine-2,6-dicarboxylate
[j] 2-Tb={$[TbOH(H_2O)_6][Zn_2Tb_4(4\text{-}Htbca)_2\text{-}(4\text{-}tbca)_8\ (H_2O)_{12}]$}n·6 n$H_2O$; 4-$H_2$tbca=4-(1H-tetrazol-5-yl)-biphenyl-3-carboxylic acid
[k] 2- Eu-Ag =$[EuAg_3(3\text{-}TPyMNTB)_2(H_2O)(MeCN)]\text{-}(ClO_4)_6\cdot 4Me\ CN$
3-TPyMNTB =tris((pyrid in-3-ylmethyl)benzoimi dazol-2-ylmethyl)amine
[l] IQY measured at 330 nm excitation wavelength
[m] dpdc = 2,2'-diphenyldicarboxylate and ip = 1H-imidazo[4,5-f][1,10]-phenanthroline
[n] mbdc= isophthalic acid; stp= 4-(2,2':6',2''-terpyridin-4'-yl)benzenesulfonate

The examples shown in Table 3 concern mostly white light emitting MOFs, while examples of yellow emitting MOFs are sporadic. The existing examples of yellow emitting MOFs are all UV-excited phosphors thus couldn't be used in the blue-chip based WLEDs. Also, most of them are rare-earth containing compounds with either doped rare-earth elements or rare-earth ions as metal centers.

1.3.4 Rare-earth-free phosphors for WLEDs.

As discussed in Section 1.3.2, the commercial phosphors for WLEDs are almost all rare-earth containing inorganic compounds. Thus the WLEDs market largely relies on the supply of rare-earth elements. However, potential supply risks and high cost[60] (Figure 8) of these critical materials have become an important issue that may impede the widespread usage of WLEDs.

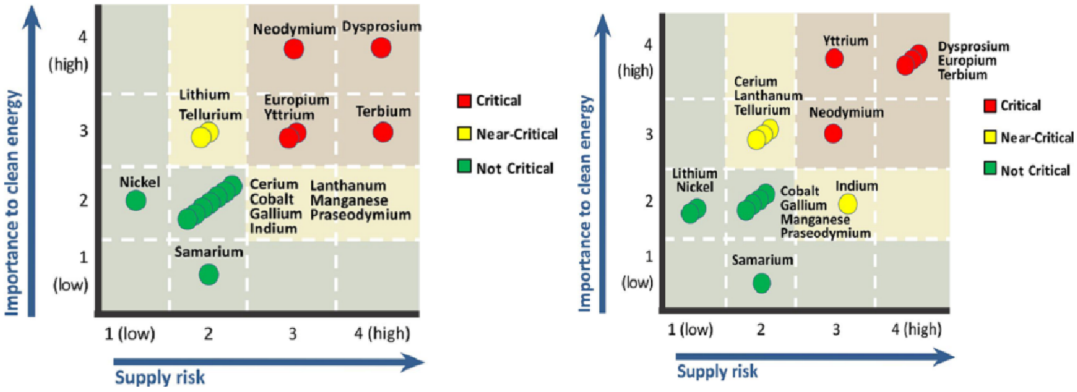

Figure 8. Determinations that some rare-earth-elements are critical for short term (present-2015, left) and mid-term (2015-2025, right). Reprint with the permission from US Department of Energy. Copyright @ US Department of Energy.

1.4 Adsorption in MOFs.

Traditional porous materials such as zeolites, metal phosphates and metal sulphides have been well explored for their applications as molecular sieves or catalysts over the past 240 years.[61] More recently, the adsorption properties[62,63] of MOFs have also been intensively studied, for example, methane storage,[64] H_2 storage,[65,66] CO_2 capture[67,68] and hydrocarbon separation.[69,70]. Compared to the traditional porous frameworks such as zeolites, which have been applied in industry but with limited pore shapes and sizes, MOFs have the advantages of more tunable structures and porosity by combining various metal centers with organic ligands of different shapes, lengths and functional groups.

1.4.1 Adsorption in traditional porous materials.

Adsorption has long been known as a porous solid which takes up relatively large volumes of condensable gas.[71] In 1777, both Fontana and Scheele noted that gas could be taken up by calcined charcoal, while Sheele also found the gas which has been taken up by charcoal could be expelled from it while taking and be retaken on cooling. This initiated the later study and investigation of "adsorption", which was first used by Kayser in 1881 to describe the condensation of gases on free surfaces, phenomenon.[71]

Untill the mid-1990s, only two types of porous solid materials have been widely studied and applied in industry - inorganic and carbon-based materials.[69] Zeolites, a class of crystalline aluminosilicates that were first discovered in the 18th century and

then hydrothermally synthesized in the 1940s[72] with pore size around 4-13 Å, were a type of representative inorganic porous material type.[69] Zeolites have been applied in three major fields including 1) separation and purification; 2) catalysts in petroleum refining and petrochemical industries and 3) liquid waste treatement.[72] Activated carbons are amorphous carbonaceous materials which have higher porosity and specific surface area compared to zeolite obtained by combustion or partial combustion of certain carbonaceous substances.[69,73] Activated carbons have been widely applied in air or water purification, removal of toxins in medicine, and serve as catalysts or catalysts support.[73]

1.4.2 Adsorption in MOFs.

Even though zeolites and activated carbons have been used in industry for decades, some issues remain to be resolved. For example, the natural and synthesized zeolites are limited with only certain structural types, causing limited pore size and shapes. Also, the inner surface of zeolites couldn't be modified to possess different functions. Activated carbons are amorphous materials, thus their structure characterization is difficult which makes it problematic to develop structure and property correlations.

Compared to zeolite and activated carbons, the structure of MOFs can be easily analyzed by single crystal X-ray diffraction method, and their pore size, shape and inner surface functionality can be designed and tailored by choosing different organic linkers and metal centers, thus effectively tuning adsorption properties. For example, in the

study of CO_2 capture from flue gas mixtures, MOFs with more open metal site and Lewis basic sites are proven to possess higher affinity with CO_2 thus are able to have higher separation factor of CO_2 to N_2. This has prompted great effort in making MOFs with high density of open metal sites..

1.4.3 Commensurate and incommensurate adsorption in MOFs.

Typically, adsorption in zeolites and MOFs happens when the pore size of the adsorbent is much larger than the size of adsorbate. The orientations of the adsorbates are usually random in the pore or cavity of the adsorbents. In some cases, when the size and shape of an adsorbate are compatible to the crystal-symmetry and the pore structure of the adsorbent, adsorption becomes ordered with specific orientation. Commensurate adsorption is a term used to describe this phenomenon. By studying this fundamental phenomenon, information on adsorbate-adsorbent interaction and adsorption-desorption mechanism can be obtained.

2. Metal organic framework as yellow phosphor for white light emitting diode

Note: A manuscript resulted from this work is currently under preparation.

As discussed in 1.3, potential supply risks of these critical materials have pushed the search for alternative RE-free phosphors to a level of urgency. Considering the existing MOFs phosphors and the variability of MOFs' luminescent properties, it is highly possible to synthesize MOFs as yellow phosphors with non-rare-earth metal ions. In this chapter, we describe the design and synthesis of a new rare-earth-free yellow phosphor made of metal organic framework, $[Zn_6(btc)_4(tppe)_2(DMA)_2]\cdot 11DMA\cdot 3H_2O$ (**1**·sol). The compound emits intrinsic yellow light upon excitation with blue light with exceptionally high quantum efficiency.

2.1 Design of rare-earth-free yellow phosphors

Our recent studies reveal that optical emission by luminescent MOFs (LMOFs) comprised of Group-12 metals (e.g. Zn) and fluorescent ligands is bandgap associated and typically involves ligand-based electron transfer, or ligand-to-ligand charge transfer (LLCT) processes. The LMOFs often show significantly enhanced photoluminescence (PL) with respect to the constituting ligands themselves.

To design highly efficient RE-free, blue-excitable yellow phosphors, our strategy is, therefore, to construct zinc based LMOFs employing strongly emissive fluorophore

ligands, such as tppe (1,1,2,2-tetrakis(4-(pyridin-4-yl)phenyl)ethane, Figure 9A). At room temperature, tppe has a strong green emission (500 nm) with a relatively high QY (57.2%, λ_{ex} = 400 nm), making it a suitable linker candidate, however to achieve yellow emission, a decrease in the bandgap of the resultant LMOF with respect to the HOMO-LUMO energy gap of tppe is required. We have accomplished this through a bandgap modulation approach, using 1,3,5-benzentricarboxylate (btc, Figure 9B) as a co-ligand.

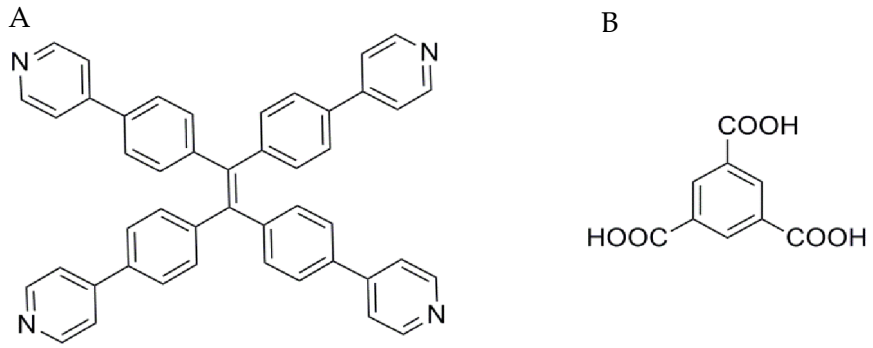

Figure 9. A) Ligand 1,1,2,2-tetrakis(4-(pyridin-4-yl)phenyl)ethane (tppe) and B) 1,3,5-benzentricarboxylate (btc, right).

We have examined the electronic properties of tppe (Figure 10) and H_3btc employing density functional theory (DFT) computations on Gaussian 09. B3LYP was used for all caculations and basis set 6-31+G* was used to optimize ligands. Our theoretical calculations indicate that btc has a LUMO energy that is lower than that of tppe. This will most likely result in a reduced band gap of LMOF built on the two ligands.

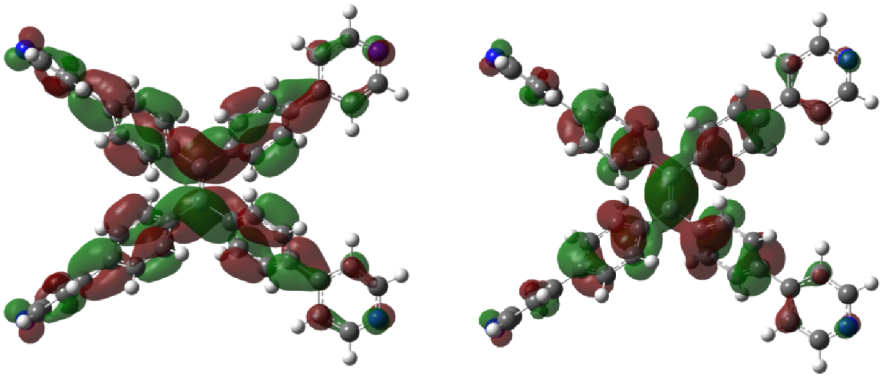

Figure 10. HOMO (left) and LUMO (right) of tppe.

In this work, we have successfully grown single crystals of compound **1** incorporating Zn^{2+}, tppe and btc under solvothermal conditions (Figure 11). Compared to tppe with a HOMO-LUMO energy gap of 2.69 eV, the new LMOF has a smaller bandgap (~2.38 eV) and significantly increased quantum yield (from 57.2% of tppe to 90.7% of compound **1**, λ_{ex} = 400 nm). Upon excitation in the range of 350 to 450 nm,

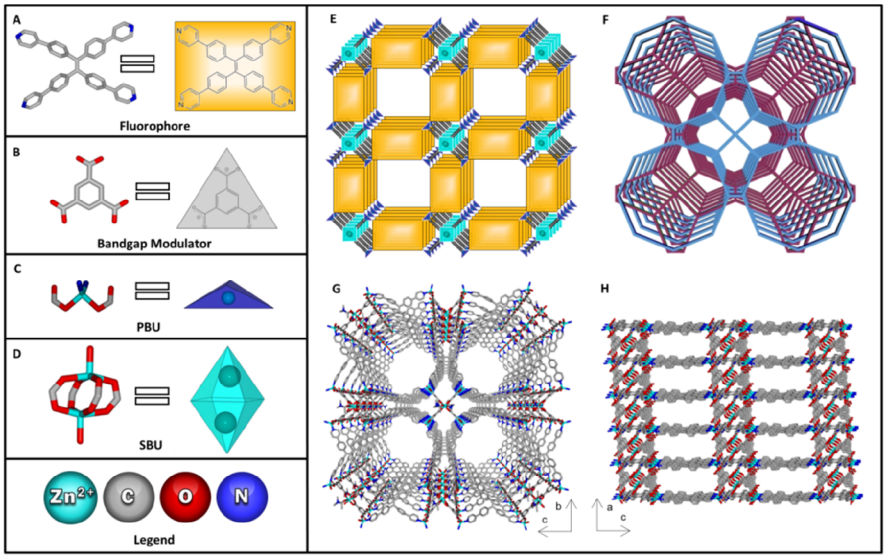

Figure 11. Crystal structure of 1. (**A**) tppe ligand. (**B**) btc ligand. (**C**) primary building unit. (**D**) secondary building unit. (**E**) polyhedron drawing illustrating overall

connectivity. (**F**) topological net of **1**. (**G**) 1D channels in the framework viewed along the *a* axis. (**H**) framework viewed along the *b* axis.

compound **1** emits bright yellow light with an emission maximum at 540 nm; the Commission International de I'Eclairage (CIE) coordinates are (0.39, 0.57), which is in the yellow range. The external QY of **1** accounts for 96% of its internal QY at 400 nm excitation, indicating nearly 100% absorption. To verify its suitability for use in PC-WLEDs a prototype preliminary device was fabricated using **1** coated on a blue LED bulb, which was measured to have a 47.4 lm/W luminous efficacy, a value well above the requirement of commercial LED lamps.

2.2 Synthesis of tppe and Compound 1.

2.2.1 Synthesis of 1,1,2,2-tetrakis(4-(pyridin-4-yl)phenyl)ethane ligand.

1,1,2,2-tetrakis(4-bromophenyl)ethane (**A**) was synthesized according to the reference literature (Figure 12) . 75 mmol (25 g) 1,1,2,2-tetraphenylethene was placed in a watch glass on the rack of a desiccator. 585 mmol (30 ml) bromine liquid was poured in the bottom of the desiccator. The desiccator was closed with a small hole left to release hydrogen bromide formed from the reaction. After 7 days, the yellow solid was collected and recrystallized with dichloromethane/methanol (2:1) to give white crystals. Yield: 37 g, 76%. ^{1}H NMR (Figure 13) ($CDCl_3$, 300MHz, 298K): 6.84 (d, 8H, H ArH), 7.26 (d, 8H, H ArH).

The synthesis method for 1,1,2,2-tetrakis(4-(pyridin-4-yl)phenyl)ethane (**B**) is modified from the original reported procedure (Figure 12) . 2.8 mmol (1.8 g) **A**, 16.68 mmol (2.05 g) pyridine-4-boronic acid, and 0.93 mmol (207 mg) palladium(II) acetate were added into a 250 ml flask. 18.5 mmol (3.93 g) potassium phosphate tribasic was dissolved in 5 ml water and then the solution was added into the 250 ml flask. 100 ml dimethylformamide (DMF) and 1.38 mmol (390 mg) tricyclohexylphosphine were then also added, and the solution was refluxed at 160 °C for 48 hs under nitrogen. After cooling down to room temperature, the product was first vacuum evaporated and then extracted with chloroform for three times. The organic phase was then washed with water and dried with anhydrous sodium sulfate. The final yellow powder product was purified by column chromatography, with $CHCl_3$: MeOH = 30:1 mobile phase; the yield was ~50%. ^1H NMR (Figure 14) ($CDCl_3$, 300MHz, 298K): 8.66 (br, 8H, H -Py), 7.46-7.50 (m, 16H, ArH), 7.25 (br, 8H, H -Py).

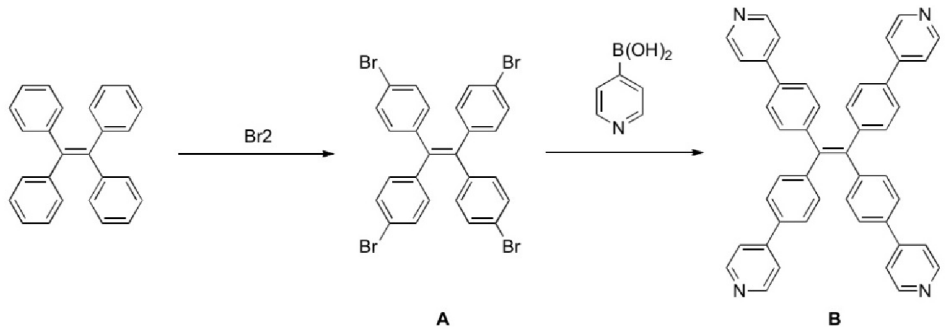

Figure 12. Scheme of tppe (B) ligand synthesis.

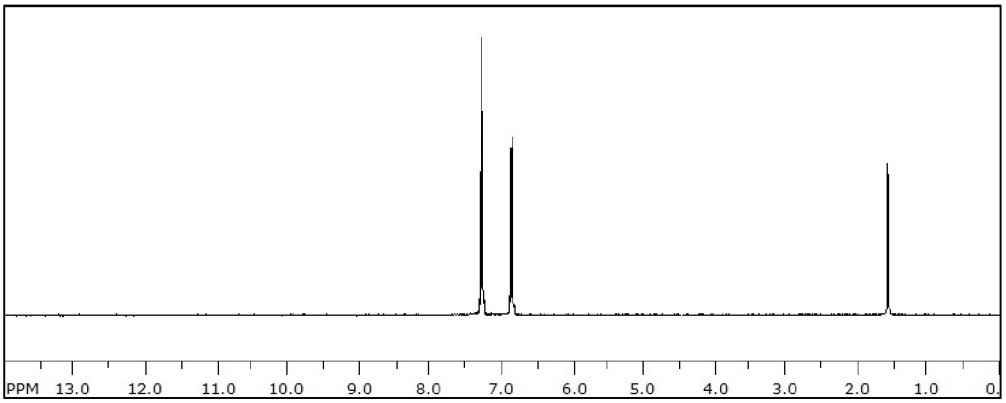

Figure 13. ^{1}NMR of A. ^{1}H NMR ($CDCl_3$, 300 MHz): 6.84 (d, 8H, H ArH), 7.26 (d, 8H, H ArH). Additional peaks: 7.26 (m, $CDCl_3$), 1.6 (m, H_2O).

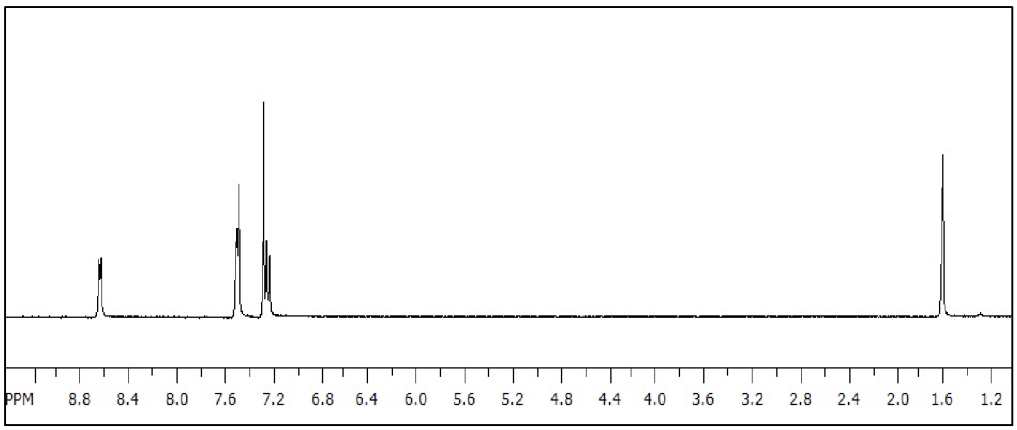

Figure 14. ^{1}NMR of B. ^{1}H NMR ($CDCl_3$, 300 MHz): 8.66 (br, 8H, H -Py), 7.46-7.50 (m, 16H, ArH), 7.25 (br, 8H, H -Py). Additional peaks: 7.26 (m, $CDCl_3$), 1.6 (m, H_2O).

2.2.2 Synthesis of compound 1.

Solvothermal reactions of $Zn(NO_3)\cdot 6H_2O$, tppe, and btc in dimethylacetamide (DMA) produced needle-shaped yellow crystals suitable for single crystal diffraction studies. 0.060 mmol (18 mg) zinc nitrate hexahydrate, 0.040 mmol (8.4 mg) benzene-1,3,5-tricarboxylic acid, and 0.02 mmol (12.8 mg) tppe were dissolved in 15 ml dimethylacetamide (DMA) in a 20 ml glass vial, followed by 0.3 ml tetrafluoroboric acid. The vial was capped and ultrasonicated until the solution became transparent, and then heated in a 150 °C oven for 2 days. Needle shaped yellow crystals were isolated and washed with 10 ml DMA 3 times.

2.3 Single crystal data of Compound 1.

Compound **1** crystallizes in the triclinic space group *P-1* (Table 4) and has the general formula $[Zn_6(btc)_4(tppe)_2(DMA)_2]\cdot 11DMA\cdot 3H_2O$ (**1**·sol). The structure is a new type of three-dimensional (3D) network with two-fold interpenetration. The framework is built on two different building units: a primary building unit (PBU, Figure 15A), and a paddle-wheel based secondary building unit (SBU, Figure 15B). The PBU is comprised of a tetrahedrally coordinated Zn^{2+}, connected to two nitrogen atoms (from two different tppe ligands) and two oxygen atoms (from two carboxylate groups of two different btc ligands); the distance of Zn^{2+} to the other uncoordinated oxygen atoms that share the carboxylates are 2.6 and 2.7 Å, which are too long to be considered as bonds when

compared to typical Zn-O bond lengths (~2.0 Å) found in MOFs. The two Zn^{2+} atoms in the SBU each bond to four carboxylate oxygen atoms from four different btc linkers, and an oxygen atom from a DMA molecule. A btc linker connected to two PBU and one SBU (Figure 15C) and a tppe linker connected to four PBU (Figure 15D). The two types of building units are connected by btc linkers (Figure 15E), forming a 3D net (Figure 15F), and two such identical nets interpenetrate to give rise to the overall 3D framework (Figure 10F). The framework possesses a 1D channel along the *a*-axis (Figure 15G) with a cross section of 6.5 × 6.6 $Å^2$, measured as the closest distance between the two carbons on opposite sides of the internal wall, excluding van der Waals radius. Viewed along the *b* axis, the organic linker tppe is stacked along crystallographic (*bc*) plane (Figure 11H).

A

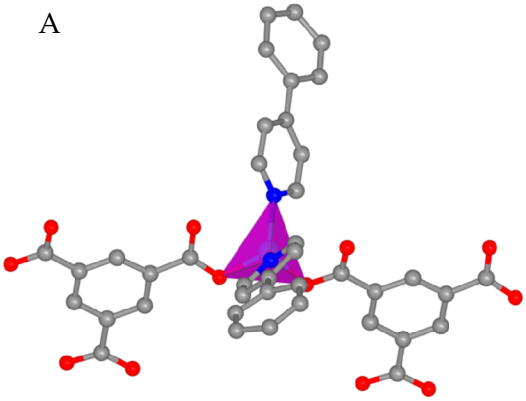

B

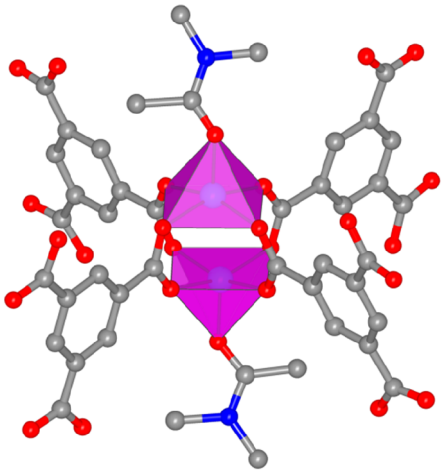

C

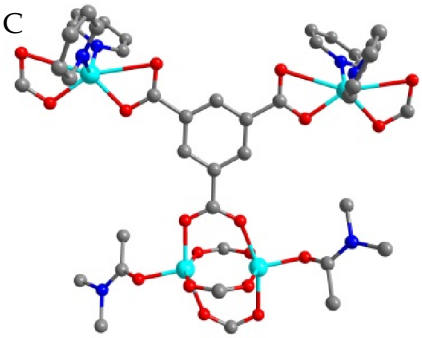

D

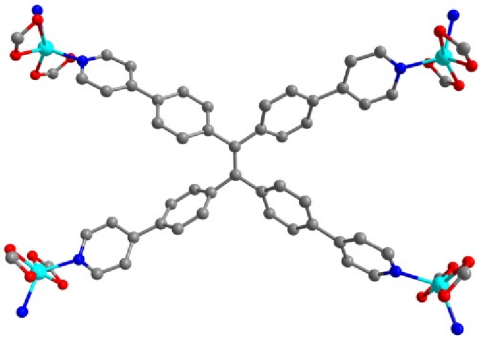

E

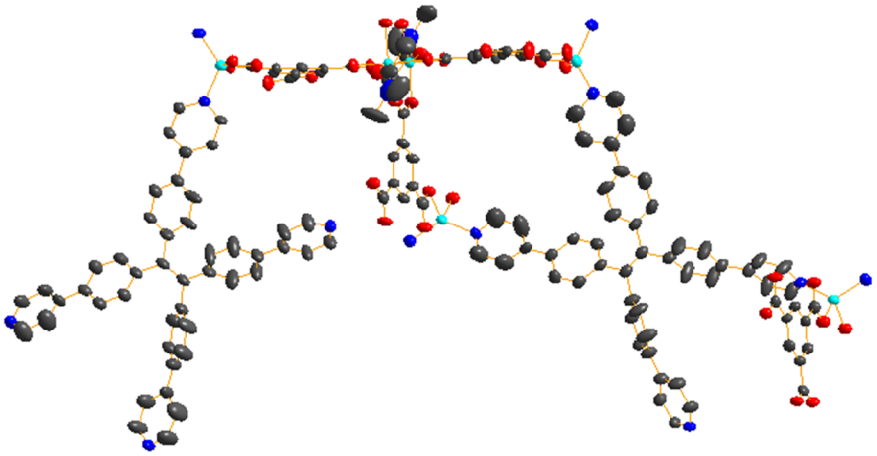

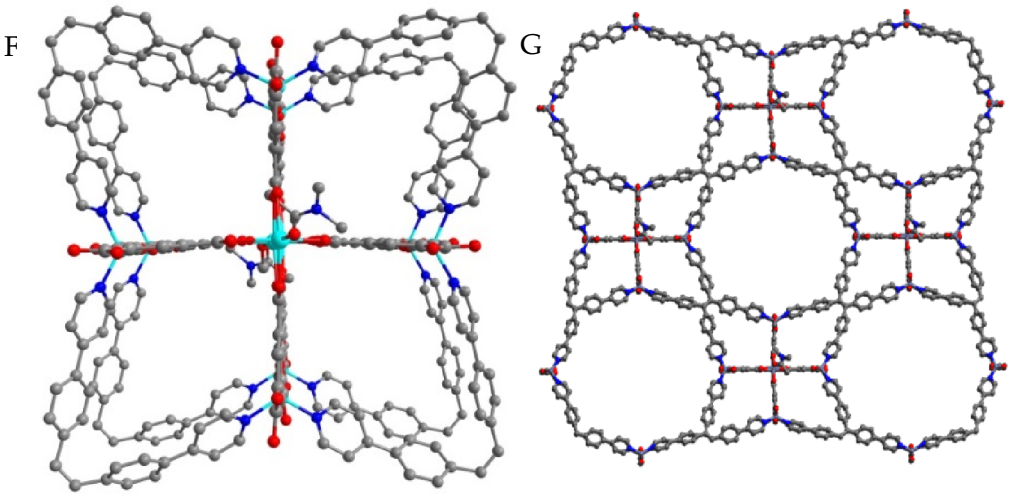

Figure 15. Structure plots of compound **1**·sol: (A) Primary building unit; (B) Secondary building unit; (C) A btc ligand connected to two primary building units and one secondary building unit; (D) A tppe ligand connected to four primary building units; (E) The asymmetric unit of compound **1**. Ellipsoids are shown at the 50% probably level; (F) The connectivity of primary building unit and secondary building unit; (G) 3D dimensional framework viewed along the *a* axis.

The total solvent accessible volume after removal of the guest molecules is 3886.7 $Å^3$ per unit cell, or 44.1% as calculated by Platon, from which a pore volume of 0.437 cm^3/g is calculated. The DMA molecules act as both the terminal ligands (coordinated to the metal centers of the SBU), and as guest molecules. H_2O molecules act as guest molecules and are hydrogen bonded to the carboxylate groups that are not coordinated to Zn and to each other.The point symbol of the framework is {6^2.8^4}2{6^2.8}4 {6^4.8^2}5, with a 4-nodal net topology.

Table 4. Single crystal data of compound 1.

Empirical formula	C176 H190 N20 O39 Zn6	
Formula weight	3601.69	
Temperature	150(2) K	
Wavelength	0.7749 Å	
Crystal system	Triclinic	
Space group	P -1	
Unit cell dimensions	a = 10.1093(13) Å	α= 91.444(2)°.
	b = 29.515(4) Å	β= 93.316(3)°.
	c = 29.532(4) Å	γ = 91.622(3)°.
Volume	8790(2) $Å^3$	
Z	2	
Density (calculated)	1.361 Mg/m^3	
Absorption coefficient	1.115 mm^{-1}	
F(000)	3756	
Crystal size	0.310 x 0.280 x 0.260 mm^3	
Theta range for data collection	2.511 to 25.498°.	
Index ranges	-11<=h<=11, -32<=k<=32, -32<=l<=32	
Reflections collected	79066	
Independent reflections	25209 [R(int) = 0.1030]	
Completeness to theta = 27.706°	79.2 %	

Absorption correction	Semi-empirical from equivalents
Max. and min. transmission	0.858 and 0.611
Refinement method	Full-matrix least-squares on F^2
Data / restraints / parameters	25209 / 6357 / 2486
Goodness-of-fit on F^2	1.030
Final R indices [I>2sigma(I)]	R1 = 0.0824, wR2 = 0.2056
R indices (all data)	R1 = 0.1313, wR2 = 0.2340
Largest diff. peak and hole	1.062 and -0.621 e.$Å^{-3}$

2.4 Density functional theory (DFT) calculations.

Density functional theory (DFT) computations on Gaussian 09 were performed by Zhichao Hu (a group member) on both ligands and LMOF to evaluate their electronic properties. The results are summarized in Table 5 and Figure 16.

Table 5. HOMO and LUMO energies of ligands and compound 1 fragment.

Compound	HOMO (eV)	LUMO (eV)	ΔE (eV)
tppe	-6.003	-2.399	3.604
btc	-8.123	-2.445	5.678
1 (fragment)	-6.012	-2.481	3.530

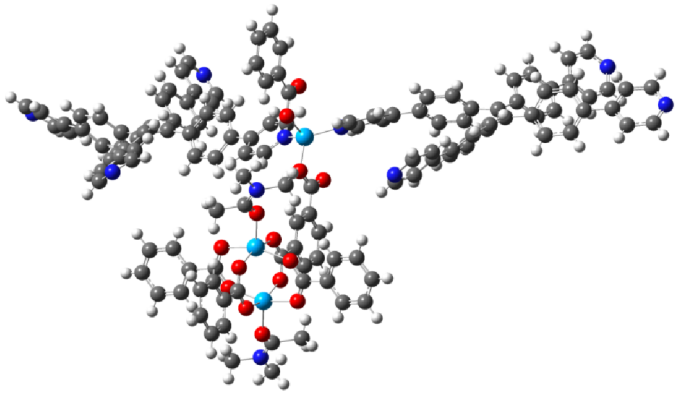

Figure 16. Selected fragment of compound **1**.

2.5 Optical properties of Compound 1.

The optical absorption and PL excitation and emission spectra of powder samples of both tppe and compound 1 (as-made sample dried in air) were measured at room temperature (Figure 17, B and C). The estimated HOMO-LUMO and VB-CB energy gaps of tppe and compound 1 are ~2.69 and ~2.38 eV, respectively, based on their optical absorption spectra collected at room temperature (Figure 17B). The decrease in the bandgap of **1** is consistent with the orbital energies obtained by DFT calculations performed on the individual ligands (tppe and btc) and a fragment of 1 (Figure 17A). These values are also in full accordance with their emission energies. The free tppe ligand emits green light (500 nm) when excited at 360-400 nm, which is due to intramolecular π-π* transitions (Figure 11), while free H_3btc does not emit in visible region. Upon excitation at the same wavelength (400 nm), compound 1 emits yellow light with an emission maximum at ~540 nm and an internal QY of 90.7%, a significant increase compared to 57.2% for free

tppe (Table 6). To the best of our knowledge, this value is the highest among all RE-free and blue-excitable yellow phosphors reported to date. While the highest emission intensity of **1** is achieved at an excitation wavelength of 350 nm (monitored at 540 nm, Figure 17C), it is worth noting that the excitation intensity is relatively flat from its max to ~450 nm, indicating the material can be excited effectively by a range of light sources, including blue light. Indeed, the internal QY was also obtained at excitation wavelengths deeper into the visible region, and were found to be 72.9, 67.9 and 63.9%, at 420, 440 and 450 nm, respectively. The emission red-shift of **1**, with respect to that of tppe, is a result of incorporating btc as a bandgap modulator, which leads to a decrease in the bandgap energy and corresponding emission (Figure 17, A and C, Figure 11, and Table 5). The external QYs of 1 were measured on a QE2000 system and are listed in Table 6. At 400, 415, 440 and 455 nm, they account for 96%, 95.3%, 91.4% and 84.7% of the internal QY values, respectively, indicating high absorption efficiency of the compound (nearly 100%).

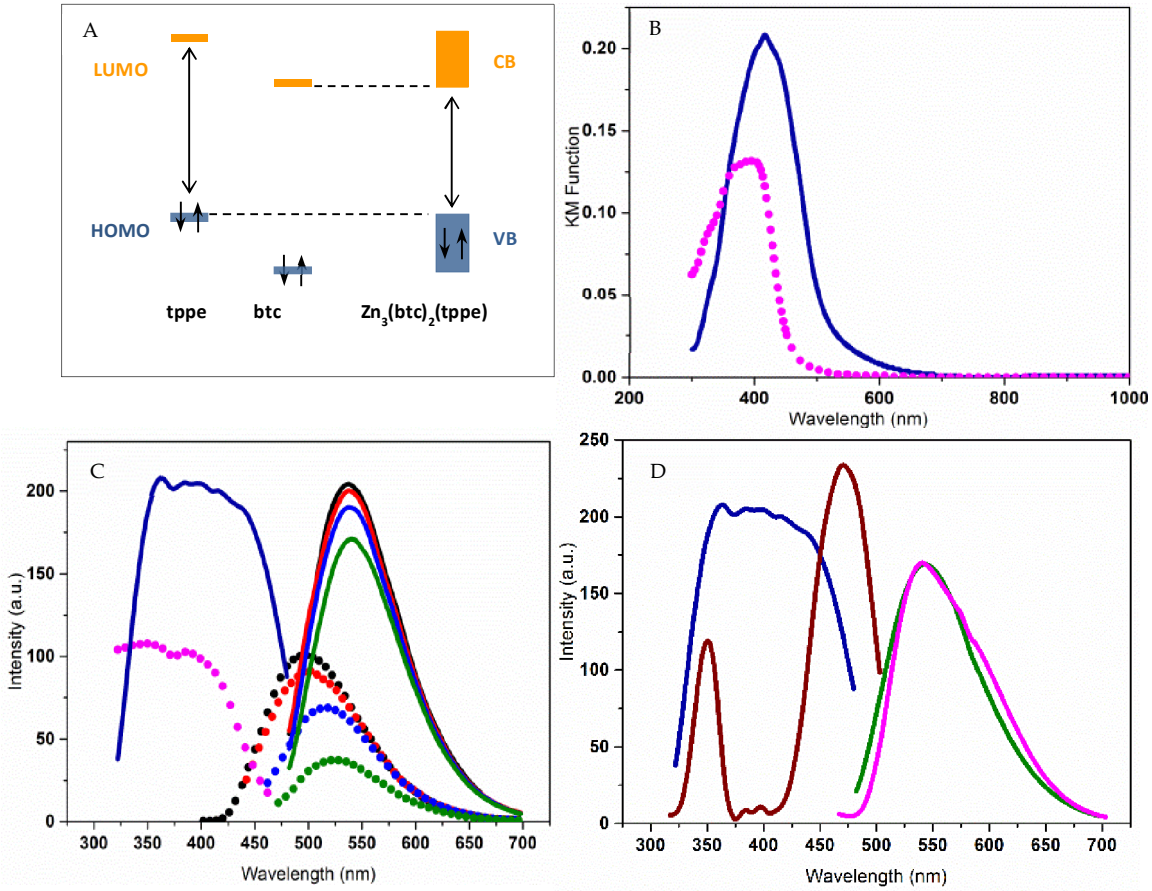

Figure 17. Optical properties of 1 compared to tppe and YAG: Ce^{3+}. (A) Schematic presentation of orbital energies for tppe (left), btc (middle) and compound **1** (right) calculated by DFT method. **(B)** Optical absorption spectra of tppe (dotted line, pink) and **1** (solid line, navy blue). **(C)** Optical excitation (left) and emission (right) spectra of tppe and compound **1**. Excitation: tppe (dotted line, pink) and **1** (solid line, navy blue), monitored at 500 and 540 nm, respectively. Emission: tppe (dotted lines, black and red, excited at 360 and 400 nm, respectively); compound **1** (solid lines, black, red, blue, and green, excited at 360, 400, 420 and 440 nm, respectively). **(D)** Optical excitation (left) and emission (right) spectra of compound **1** and YAG: Ce^{3+} (type 9800, Global Tungsten & Powders Corp.). Excitation: **1** (navy blue) and YAG: Ce^{3+} (dark red), monitored at 540 nm. Emission: **1** (green) and YAG: Ce^{3+} (pink) excited at 440 nm.

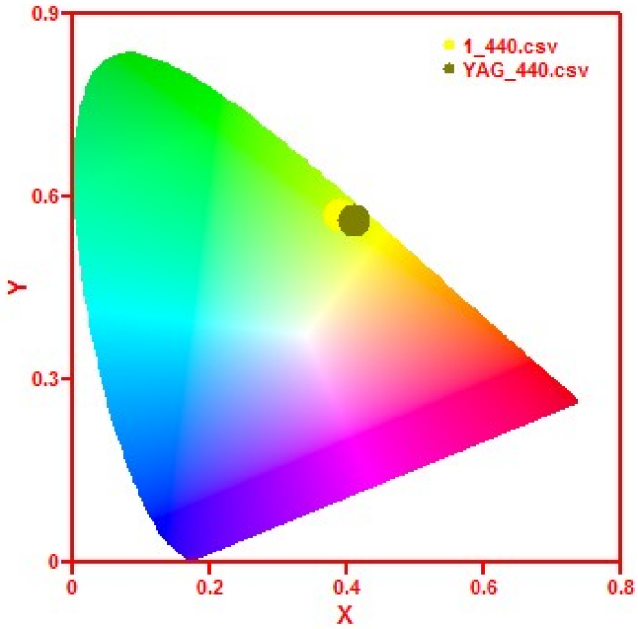

Figure 18. CIE coordinates of compound **1**: (0.39, 0.57) and YAG:Ce^{3+} (0.41, 0.56).

Comparison of 1 and YAG:Ce^{3+}. A comparison between **1** and a commercial yellow phosphor, cerium doped yttrium aluminum garnet (YAG:Ce^{3+}, type 9800, Global Tungsten & Powders Corp.) revealed remarkable similarity in emission properties (Figure 17D, 18 and 19). The Commission International de I'Eclairage (CIE) coordinates of **1** (0.39, 0.57) are well within the yellow range and are very close to those of YAG:Ce^{3+} (0.41, 0.56) (Figure 18). The emission spectra of the two are nearly identical (Figure 17D), and at room temperature, the internal QY of **1** (~90.7%) is approaching that of YAG:Ce^{3+} (95%).

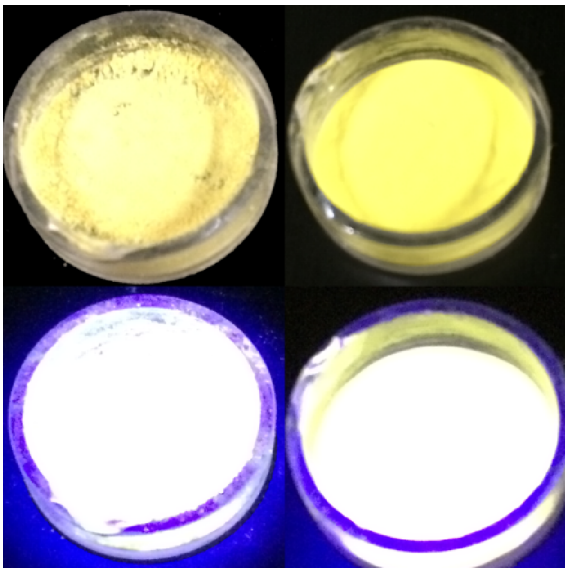

Figure 19. Compound **1** (top left) and YAG:Ce^{3+} (top right) under natural light; compound **1** (bottom left) and YAG:Ce^{3+} (bottom right) under blue light.

2.6 Solution processability study of Compound 1.

The dispersible nature of compound **1** in selected solutions makes it possible to coat the samples on flexible substrates, such as a rope or thin cotton strings, which is not possible with traditional inorganic yellow phosphors such as YAG:Ce^{3+}. We demonstrate this in Figure 19, where dispersed samples of compound **1** were coated on thin cotton strings, and then illuminated under a 12 W blue LED lamp (emission range: 450-470 nm, ABI LED Lighting Company); Figure 20A, C, E show coated/uncoated strings under daylight, and Figure 20B, D, F show the same string under the blue light.

A prototype WLED device was assembled using a 5 mm 455-460 nm blue LED bulb, with sample **1** coated on the surface (Figure 20G). The coating solution was prepared by dispersing powders of **1** in ethyl acetate under ultrasonication for 1 h. The blue LED

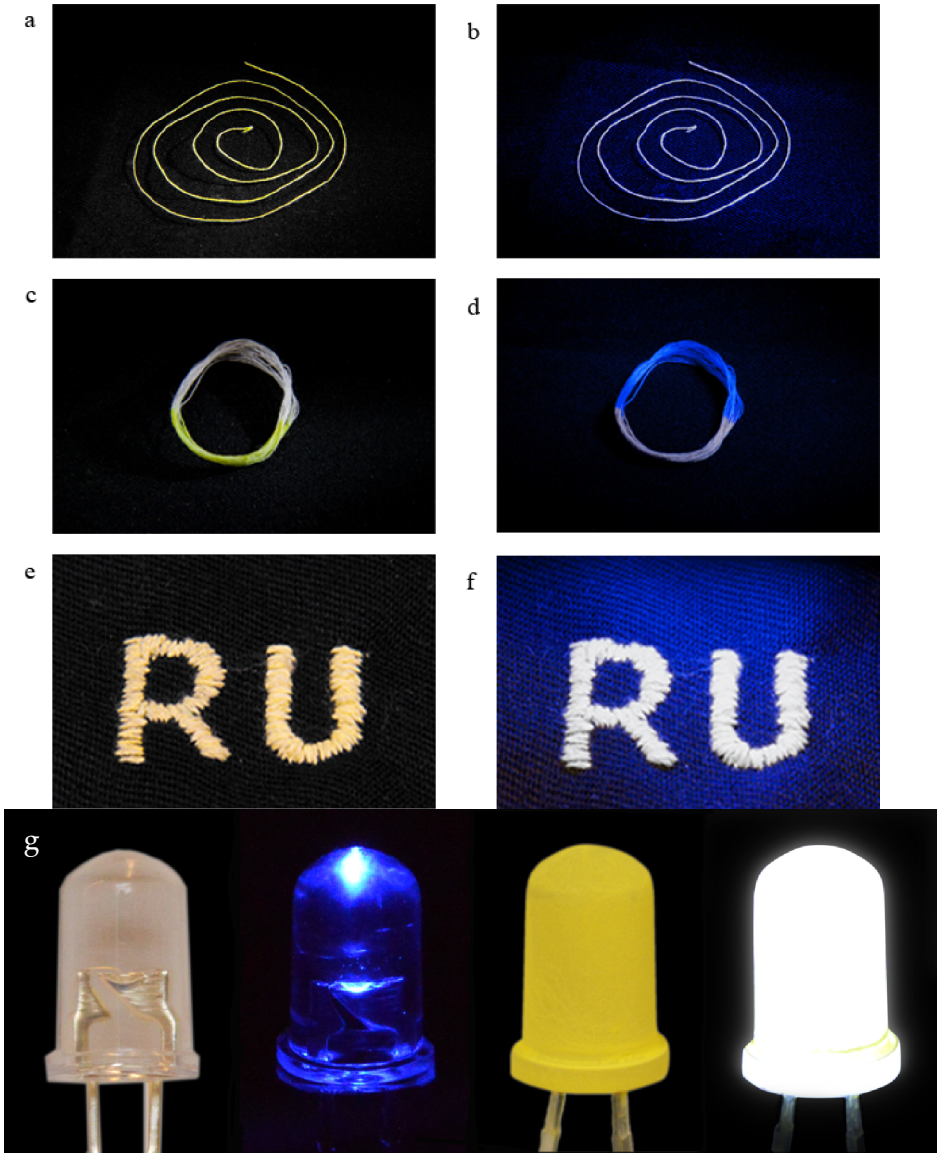

Figure 20. Solution processability of compound 1. (**A-F**) Images of dispersed sample **1** coated on thin cotton strings. Top row: images of samples under daylight. Bottom row: images of samples illuminated by a 450 nm blue LED. (**A**)-(**B**) **1** coated on a single cotton string. (**C**)-(**D**) a wound-up string with the bottom half coated with **1** and the top half uncoated. (**E**)-(**F**) "RU" sewed on black cloth by cotton string coated with compound **1**. (**G**) WLED assembly. Left half: blue LED bulb before (top) and after (bottom) being illuminated. Right half: the same blue LED coated by a dispersed sample of **1** before (top) and after (bottom) being illuminated. Note: The four photographs in **G** have been altered to remove their backgrounds; this alteration is purely for aesthetics and in no way changes the nature of the content provided.

bulb was then dipped into the suspension solution several times until a thin and uniform film formed on the surface of the bulb; bright white light was generated when a 3 V bias was applied. The luminous efficacy of the WLED device was measured to be 47.4 lm/W, well above the requirement of commercial LED lamps (e.g. the minimum requirement for small LED directional lamps 40 lm/W) and can doubtlessly be improved upon, as the device was not optimized for performance.

2.7 Moisture, UV and thermal stability study of Compound 1.

To further verify the suitability of the material for potential use in PC-WLEDs, stability measurements were carried out on **1** and an assembly of **1** with Teflon film for environmental control (**TF@1**, Figure 21). **1** exhibits high moisture stability at room temperature; a sample of **1** was left sitting in air for a period greater than three months, after which time a PXRD measurement verified the material's structural integrity (Figure 22). At excitation wavelength of 455 nm, the internal QY of **1** was measured as 58.1% originally, and 57.6% after three months, with < 1% decrease over this long period of time.

The UV stability of **1** was examined at room temperature. The PL spectra of **1** after being exposed under 365 nm ultraviolet light for 3 ds and 7 ds have been measured. The emission maximum kept at 540 nm, while the PL intensity of **1** decreased 15.3% after exposed under 365 nm UV light for 1 week (Figure 21).

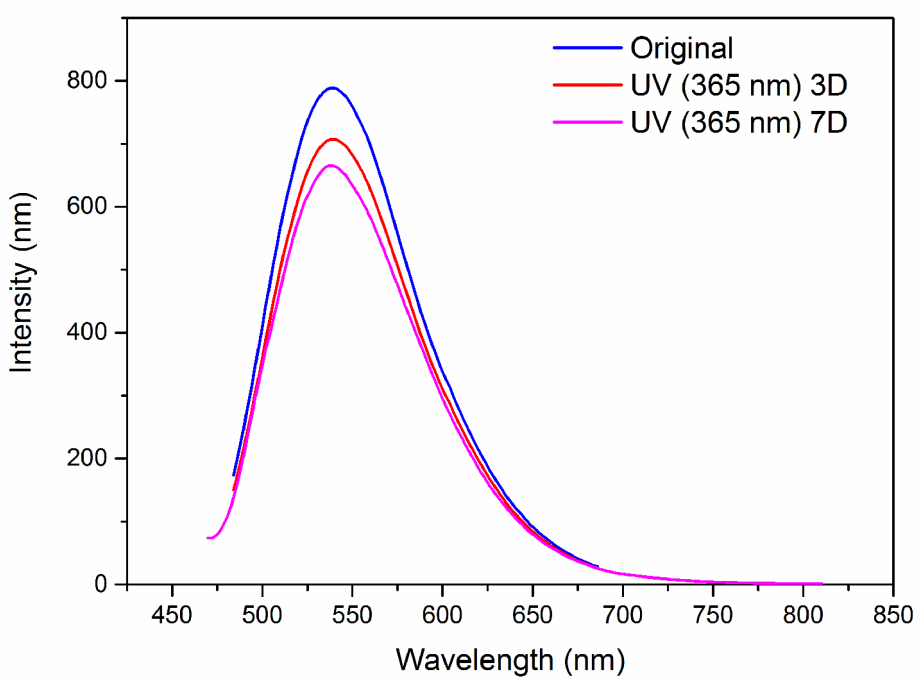

Figure 21. Photoluminescence of compound **1** under 365 nm UV light.

The thermal stability of **1** and **TF@1** (Figure 22) were examined at various temperatures. Thermogravimetric analysis (TGA, Figure 24) shows that **1** undergoes

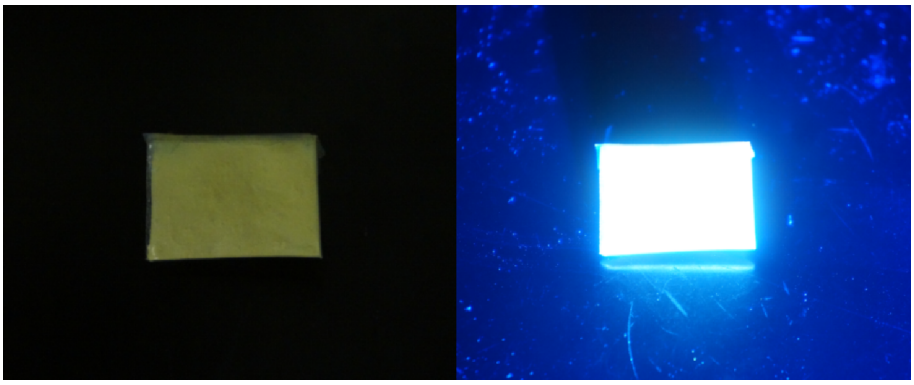

Figure 22. Images of Teflon protected compound **1** under day light (left) and 450-470 nm blue LED light (right).

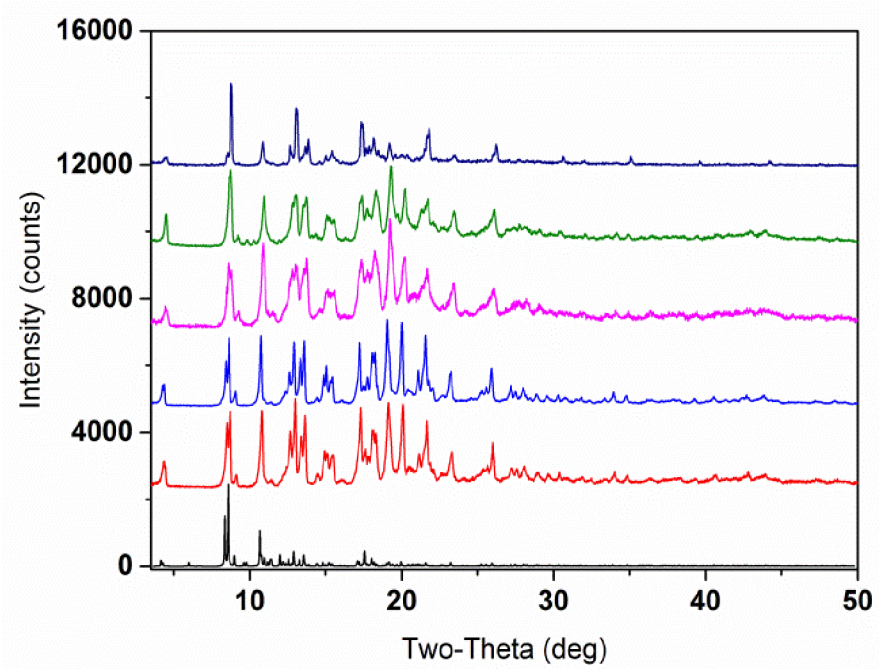

Figure 23. PXRD patterns: simulated from single crystal structure (black), **1**·sol (red), air dried sample (light blue), sample exposed to air for 3 months (pink), **TF@1** after been heated up at 180 °C for 12 hs (green), ethyl acetate exchanged **1** (navy blue).

continuous weight loss from room temperature to ~220 °C, then remains stable until ~300 °C, at which point the framework starts to decompose. PXRD and PL data were collected after **TF@1** were heated at different temperatures for a given period of time (e.g. 12 hrs), which show the material is both thermally and optically stable up to 180 °C (Figure 25, Table 6). Decreases in PL intensity and QY are less than 3.5% and 6.7%, respectively, upon heating at 150 °C for 12 hrs (Table 6).

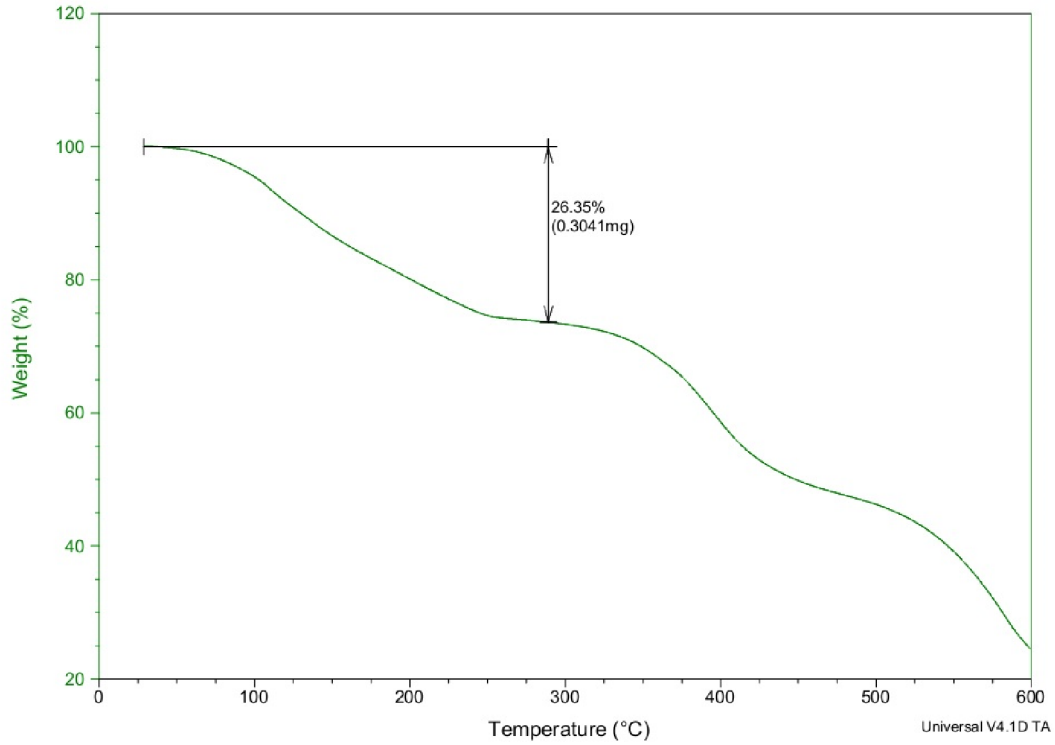

Figure 24. Thermal gravimetric profile for compound **1**·sol.

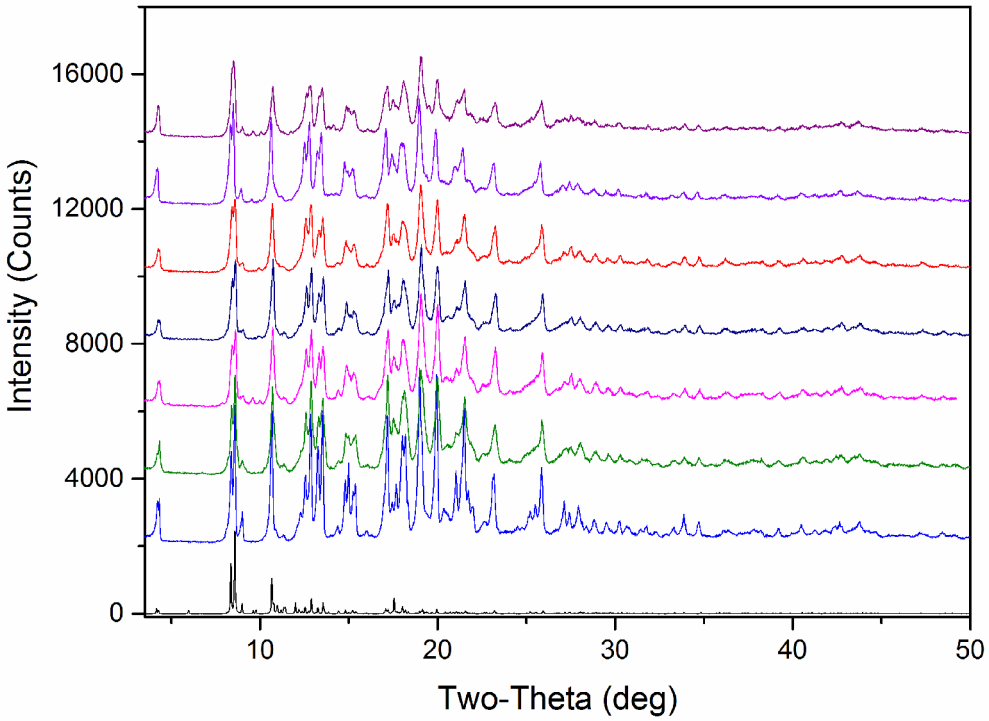

Figure 25. PXRD patterns of **TF@1** collected after being heated at various temperatures for 12 hours. From bottom to top: simulated, room temperature, 80 °C, 100 °C, 120 °C, 140 °C, 160 °C and 180 °C).

2.8 Solvent exchange study of Compound 1.

Solvent exchange of compound **1** was carried out at room temperature by soaking freshly as-made sample in various solvents for 2 days (replacing once with fresh solvent), followed by PXRD structural verification (Figure 26). PL emission spectra of the exchanged samples show shifted emission wavelengths and varying intensities (Figure 27). The fresh as-made sample (**1**·sol) has an emission maximum at 500 nm, which shifts to 540 nm with an accompanying intensity increase after drying in air (**1**). After solvent exchange with dimethylformamide (DMF), toluene (TO), 1,4-dioxane (DO), n-hexane

(HA), and ethyl acetate (EA), the emission maximum red-shifted by 8, 10, 16, 20, and 25 nm respectively, upon excitation at 440 nm. After soaking the exchanged **1**·EA and the air dried sample in DMA for 2 and 5 days, respectively, the samples' PL reverted to the original emission (Figure 27), indicating the process is fully reversible. QY measurements of the solvent exchanged samples (440 nm excitation) give the highest value for the air-dried sample, with a significant increase of 26.3% compared to that of the as-made sample, followed by **1**·DMF (increase of 7.5%). Other **1**·sol samples show a decrease in QY, with a descending order of **1**·DO, **1**·EA, **1**·HA and **1**·TO (see Table 6).

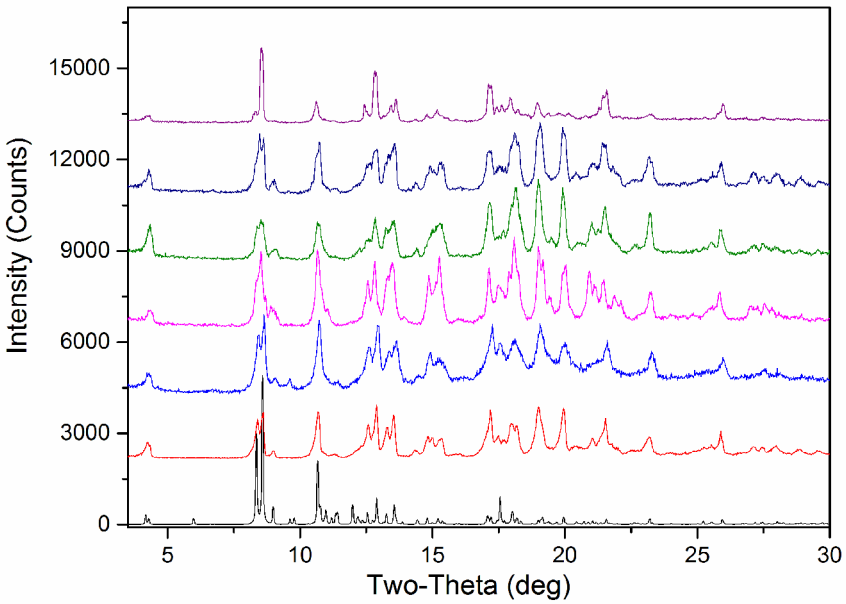

Figure 26. PXRD patterns of solvent exchanged compound **1**. From bottom to top: simulated, as-made (dimethylacetamide), samples exchanged with dimethyformamide, toluene, 1,4-dioxane, n-hexane, and ethyl acetate, respectively.

Table 6. Quantum yield values of tppe and compound 1 at various conditions.

Internal Quantum Yield (%)					
Sample	**λ_{ex} = 400 nm**	**λ_{ex} = 420 nm**	**λ_{ex} = 440 nm**	**λ_{ex} = 450 nm**	**λ_{em} (nm)**
tppe	57.2±0.6	40.2±1.0	33.2±1.1	32.1±1.3	500
1	90.7±0.7	72.9±0.5	67.9±0.6	63.9±0.2	540
TF@1$^{\alpha}$	88.8±0.6	-	65.3±0.2	62.6±0.1	540
TF@1$^{\beta}$	86.8±0.6	-	63.4±1.0	60.4±0.2	540
1·sol (as-made)	64.2±0.3	-	41.6±0.2	37.6±0.3	500
1·DMF	72.9±0.1	-	49.1±0.1	45.1±0.4	508
1·TO	31.6±0.8	-	24.7±0.1	21.4±0.2	510
1·DO	61.9±0.1	-	40.7±0.3	38.6±0.1	516
1·HA	50.1±0.1	-	33.8±0.2	29.1±0.1	520
1·EA	51.9±0.4	-	36.4±0.3	32.4±0.8	525

External Quantum Yield (expressed as % of Internal Quantum Yield, %)					
Sample	**λ_{ex} = 400 nm**	**λ_{ex} = 415 nm**	**λ_{ex} = 440 nm**	**λ_{ex} = 455 nm**	**λ_{em} (nm)**
1	96.0	95.3	91.4	84.7	540

Temperature Dependent Photoluminescence (Decrease in Intensity, ±1.0%)							
Sample	**80 °C**	**100 °C**	**120 °C**	**140 °C**	**150 °C**	**160 °C**	**λ_{em} (nm)**
TF@1 (λ_{ex} = 440 nm)	0.0	0.0	0.0	-3.0	-3.5	-6.0	540

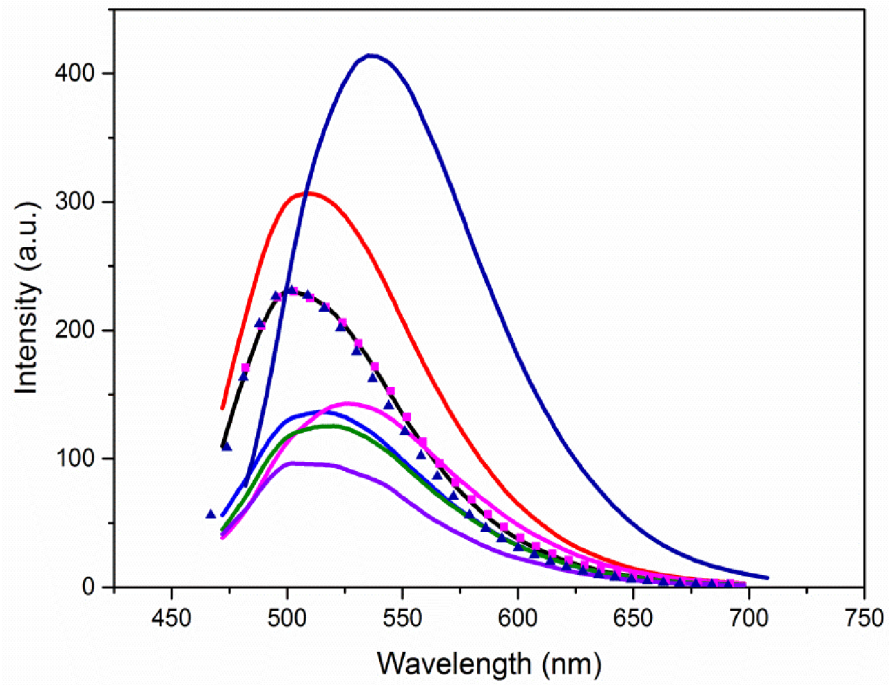

Figure 27. Emission spectra of compound **1** exchanged with different solvents. **1**·sol (black), **1** (navy blue), samples after exchange with dimethylformamide (red), toluene (purple), 1,4-dioxane (light blue), n-hexane (green), and ethyl acetate (pink); samples recovered in DMA after exchange with ethyl acetate (pink triangle) or drying in air (navy blue triangle); all excited at 440 nm. The PL intensity of the samples recovered in DMA is normalized.

2.8 Discussion and conclusion.

In this study, we have demonstrated a general designing strategy to achieve strong yellow emission of a MOF-based phosphor with desirable blue excitation. A strong green-emitting molecular fluorophore tppe is selected as a ligand because of its high emission quantum yield. A second ligand btc, with lower LUMO energy than that of tppe, is chosen as a bandgap modulator to reduce the energy gap of the resultant MOF in order to achieve a red-shift in both its absorption and emission energy. This enables the compound to be effectively excited by blue while emitting yellow light. In addition,

the immobilization of tppe ligand in a rigid and extended network structure leads to a substantial increase in the emission intensity and QY. This may be attributed to the stabilization of the tppe ligand, which can reduce non-radiative decay, as well as to the formation of framework structure, which can maximize the intra- and/or inter-molecular interactions among the organic ligands. The high external quantum yield (e.g. ~ 4% decrease with respect to that of internal quantum yield at λ_{ex} = 400 nm, see Table 6) suggests that compound **1** is an effective and strong energy absorber.

High moisture and thermal stability of phosphors are essential for their use in WLED devices . The instability of a phosphor's photoluminescence under moisture and high temperature conditions leads to intensity decrease and chromaticity degradation, thereby limiting their applications. **1** exhibits high moisture stability at room temperature, with less than 1% decrease in QY (λ_{ex} = 455 nm) after being exposed in air for more than three months. Under high temperatures, **TF@1** displayed high structural and PL stability as well, with < 6.7% QY (λ_{ex} = 440 nm) decrease after being heated at 150 °C for 12 hrs. These stability studies reinforce the notion that this material is suitable for PC-LEDs.

In summary, we have designed and synthesized a new type of yellow phosphor totally free of rare-earth elements. This was achieved by combining a highly emissive molecular fluorophore with a bandgap regulating co-ligand into a MOF structure, thus

tuning the HOMO-LUMO energy gap to attain desired excitation and emission properties. The new yellow phosphor can be effectively excited by a blue LED chip and assembled in a PC-WLED. **1** and selected solvent exchanged samples (**1**·sol) exhibit significantly enhanced emission compared to the constituent ligand (tppe). To the best of our knowledge, the RT quantum yield of compound **1** (90.7% at λ_{ex} = 400 nm) is the highest among all yellow emitting MOFs reported to date, and is approaching that of the commercial yellow phosphors such as YAG:Ce^{3+} (95%). In addition, the high solution processability of this compound enables its utility in flexible light fixtures. The exceptionally high performance of compound **1** and **1**·sol make them promising candidates for use as an alternate yellow phosphor in PC-WLEDs. The structure design and bandgap modulation approach can be generalized and applied to many other metal/ligand combinations.

2.9 Materials and Methods

Reagents and solvents were used as received from: Alfa Aesar - [1,1,2,2-tetraphenylethene (98%), bromide liquid (99.8%), dichloromethane (99.5+%), methanol (99.90%), palladium(II) acetate (99.98%), dimethylformamide (99%), chloroform (99.8%), sodium sulfate (99%), zinc nitrate hexahydrate (99%), benzene-1,3,5-tricarboxylic acid (99%), dimethylacetamide (99%), tetrafluoroboric acid (50% water solution), ethyl

acetate (99.5%), n-hexane (99%) 1,4-dioxane (99%) and tricyclohexylphosphine (98%)], Sigma Aldrich - [pyridine-4-boronic acid (90%), chloroform-d (99.9%), toluene (99+%) and potassium phosphate tribasic (98%)], and Global Tungsten & Powders Corp - [YAG:Ce3+, type 9800].

Methods of protecting sample with Teflon film

For prolonged heating at high temperatures, compound **1** was sealed within a Teflon film (American Durafilm) by MP-15 sealing equipment from Aline Heat Seal Corp.

Nuclear magnetic resonance measurement

Nuclear magnetic resonance (NMR) data was collected on a 300 MHz Oxford NMR.

Single-crystal synchrotron X-ray diffraction analysis

Single-crystal synchrotron X-ray diffraction data of **1**·sol were collected at 150 K on a D8 goniostat equipped with a Bruker APEXII CCD detector at Beamline 11.3.1 at the Advanced Light Source (ALS) in Lawrence Berkeley National Laboratory, using synchrotron radiation tuned to = 0.7749 Å. The structure was solved by direct methods and refined by full-matrix least-squares on F2 using the Bruker SHELXTL package. All guest molecule non-hydrogen atoms were located on a difference-Fourier map. All H atoms were placed in calculated positions.

Powder X-ray diffraction (PXRD) analysis

Powder X-ray diffraction (PXRD) analyses were carried out on a Rigaku D/M-2200T automated diffraction system (Ultima+) using Cu Kα radiation (= 1.5406 Å). The data were collected at room temperature in a 2θ range of 3-50° with a scan speed of 1 °/min. The operating power was 40kV/40mA.

Thermogravimetric analysis

Thermogravimetric analyses (TGA) of samples were performed using the TA Instrument Q5000IR thermal gravimetric analyzer with nitrogen flow and sample purge rate at 10 ml/min and 12 ml/min respectively. About 1 mg of sample was loaded onto a platinum sample pan and heated from room temperature to 600 °C at a rate of 10 °C/min under nitrogen flow.

Photolumenescence (PL) measurements

Photoluminescence measurements were carried out on a Varian Cary Eclipse spectrophotometer at room temperature. Powder samples were evenly distributed and sandwiched between two glass slides (which do not have emission in the visible range).

UV-Vis diffuse reflectance spectroscopy

Optical absorption spectra were measured at room temperature on a Schimadzu UV-3600 UV/VIS/NIR spectrometer. The reflectance data were converted to Kubelka-Munk function, $\alpha/S = (1-R)^2/2R$ (α is absorption coefficient, S is scattering coefficient and R is reflectance), and used to estimate the bandgap.

Internal quantum yield measurements

Internal quantum yield (QY) measurements were made on C9920-03 absolute quantum yield measurement system (Hamamatsu Photonics) with 150 W xenon monochromatic light source and 3.3 inch integrating sphere. Powder sample was placed in the sample holder and QY data were calculated by the instrument software package.

External quantum yield measurements

External quantum yields were measured by Otsuka Electronics Co. Ltd. on a QE-2000 measurement system with 150 W xenon lamp as light source, MCPD-9800 (2480) as detector and with a 6 inch integrating hemisphere. Barium sulfate ($BaSO_4$) was used as reference material.

Calculation of Commission International de I'Eclairage (CIE) coordinates

CIE coordinates of powder samples were calculated using GoCIE software. The room temperature PL data were used in these calculations.

Luminous efficacy

Luminous efficacy of the WLED assembly (sample **1** coated on the surface of 5 mm 455-460 nm blue LED chip) was measured on MCPD-9800(3683) P16 with halfmoon integrating sphere (HM500 base-down). The powder supply is DC 20 mA, 3V. An average number based on 180 measurements was calculated and reported.

3. Study the yellow emission of tppe based MOF structures.

3.1 Introduction

As discussed in chapter 2, the new MOF $[Zn_6(btc)_4(tppe)_2(DMA)_2]\cdot 11DMA\cdot 3H_2O$ (compound **1**·sol) is a promising candidate as a yellow phosphor. The emission maxima of compound **1** and tppe are 540 nm and 500 nm respectively, which correspond to the estimated energy gap of compound **1** and tppe (~2.38 eV and 2.69 eV, respectively) calculated from the optical absorption measurements. Both optical properties and DFT calculations show the origin of the photoluminescence of compound **1** came from the emission of tppe with the energy gap modulated by btc. Thus, it is natural and rational that other MOFs composed of tppe linker and a second linker may have similar or better photoluminescent properties suitable for yellow phosphors.

After various trials of synthesizing new MOFs with tppe as the following up study, three new tppe-related MOFs (Compound **2**, **3** and **4**) have been synthesized and characterized. Both compound **2** ($[Zn_2(btc)(tppe)(fa)]$) and **3** (Zn-fdc-tppe) outgassed structures emit yellow light upon blue light excitation, which construct a series of tppe-based new MOFs to serve as yellow phosphors for white light emitting diodes. However, compound **4** ($[Ni_2(bpdc)_2(tppe)]$), which is composed of Ni ions, is not luminescent. The study provides valuable information of the necessary elements to build tppe based yellow phosphors for WLEDs.

3.2 [Zn_2(btc)(tppe)(fa)] (Hfa=formic acid) (Compound 2)

A different phase of Zn-btc-tppe has been synthesized by a very similar procedure to that of compound **1**. The only difference between the syntheses method of compound **1** and compound **2** is the major solvent. Compound **1** contains DMA, while the latter phase included DMF. As discussed in Chapter 1, a few parameters such as solvent, temperature and time can affect the quality, size and even phase of the formed crystals. The phase difference between compound **1** and **2** is a good example here.

3.2.1 Synthesis of compound 2.

Solvothermal reactions of $Zn(NO_3)\cdot 6H_2O$, tppe, and btc in dimethylformamide (DMF) produced needle-shaped yellow crystals. 0.060 mmol (18 mg) zinc nitrate hexahydrate, 0.040 mmol (8.4 mg) benzene-1,3,5-tricarboxylic acid, and 0.02 mmol (12.8 mg) tppe were dissolved in 15 ml dimethylformamide (DMF) in a 20 ml glass vial, followed by 0.15 ml tetrafluoroboric acid. The vial was capped and ultrasonicated until the solution became transparent, and then heated in a 150 °C oven for 1 day. Needle shaped yellow crystals (Figure 28) were isolated and washed with 10 ml DMF 3 times. The yield is 75%.

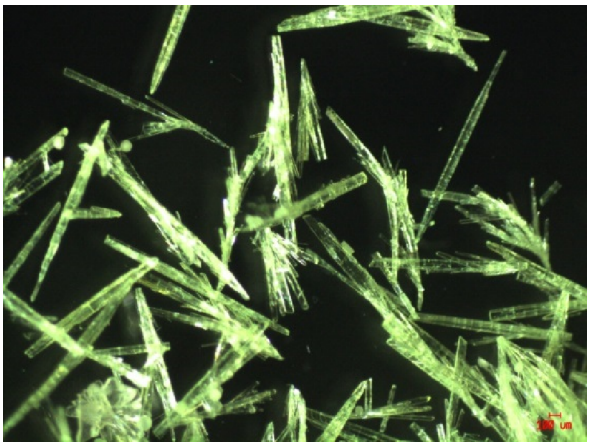

Figure 28. Crystal images of compound **2**.

3.2.2 Single Crystal Data of Compound 2.

Compound 2 crystallized in the monoclinic space group C 2/c with the general formula [Zn_2(btc)(tppe)(fa)]. The framework is built on two different primary building units comprised of tetrahedrally coordinated Zn^{2+}. One of the PBU (PBU 1, Figure 29A) is comprised of a Zn^{2+} coordinated to two nitrogen atoms (from two different tppe ligands) and two oxygen atoms (from two carboxylate groups of two different btc ligands). The second PBU (PBU 2, Figure 29B) is similar to the first PBU, but with Zn^{2+} coordinated to an oxygen atom from terminal fa molecule, instead of a carboxylate group from the btc ligand. Similar to compound **1**, the distance of Zn^{2+} to the other uncoordinated oxygen atoms that share the carboxylates are 2.656, 2.862 in PBU 1 and 2.865 Å in PBU 2, which are too long to be considered as bonds. A btc linker is connected

to two PBU 1 and one PBU 2 (Figure 29C) and a tppe linker is connected to two PBU 1 and two PBU 2 (Figure 29D). The two PBUs are connected by both btc and tppe to form

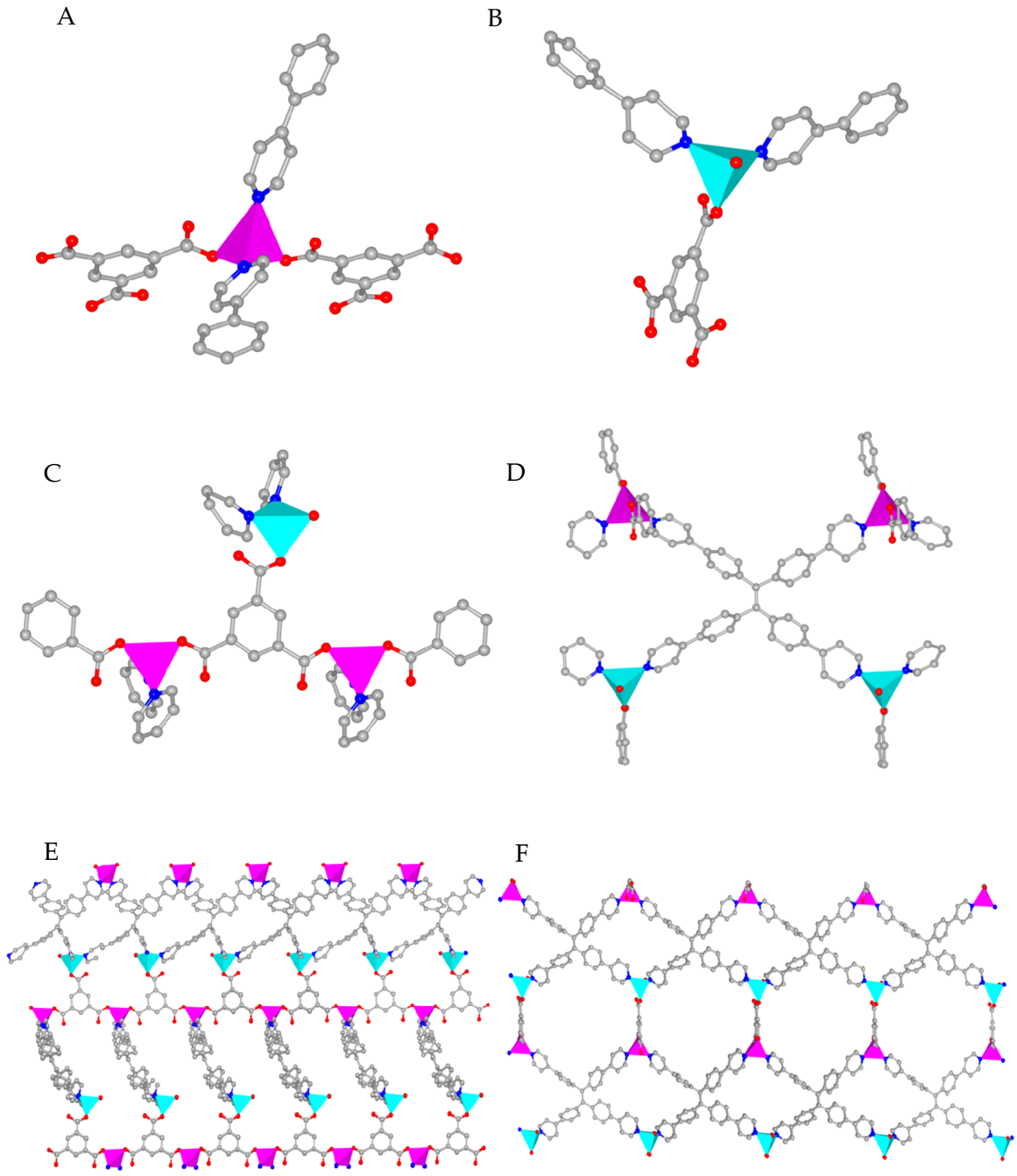
A
B
C
D
E
F

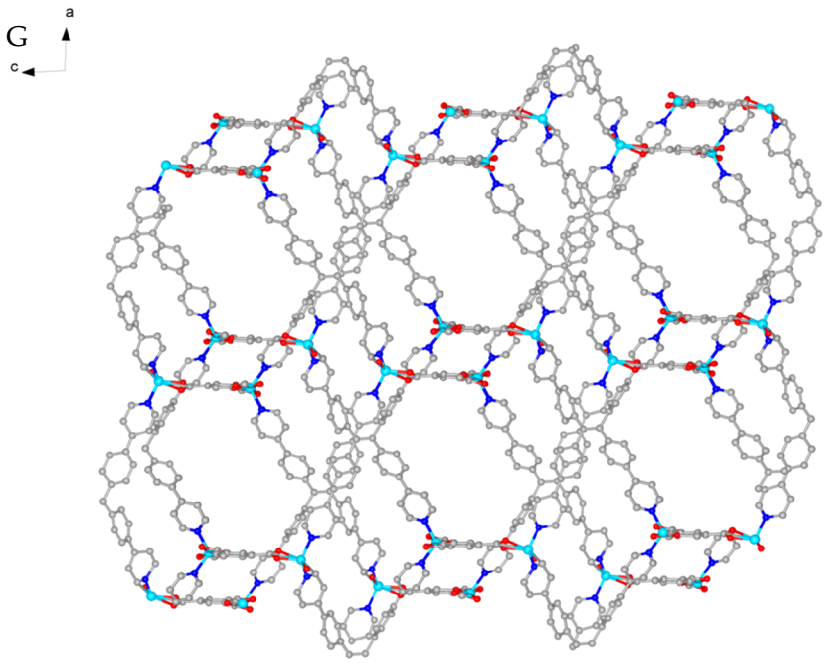

Figure 29. Structure plots of compound **2**: (A) Primary building unit type 1; (B) Primary building unit type 2; (C) A btc ligand connected to two type 1 primary building units and one type 2 primary building unit; (D) A tppe ligand connected to two type 1 and type 2 primary building units for each; (E) The connectivity of primary building units viewed from *a* axis; (F) The connectivity of primary building units viewed from *b* axis; (G) Two fold interpenetration of framework viewed from *b* axis.

a 3D net (Figure 29 E, F), and two nets interpenetrate to construct the overall 3D framework (Figure 29G).

The framework possesses a 1D channel along the *b*-axis (Figure 29G) with a cross section of 6.0 × 11.0 $Å^2$, measured as the closest distance between the two carbons on opposite sides of the internal wall, excluding van der Waals radius.

Table 7. Single crystal data of compound 2.

Empirical formula	C_{56} H_{36} N_4 O_8 Zn_2	
Formula weight	1023.65	
Temperature	100 K	
Wavelength	0.71073 Å	
Crystal system	Monoclinic	
Space group	C 2/c	
Unit cell dimensions	a = 34.519(4) Å	α= 90°.
	b = 10.1639(11) Å	β= 94.507(5)°.
	c = 36.422(4)Å	γ= 90°.
Volume	12739(2) $Å^3$	
Z	8	
F(000)	1872	

Theta range for data collection	1.122 to 18.396 deg
Index ranges	-30<=h<=30, -8<=k<=9, -32<=l<=32

3.2.2 Phase difference of compound 1 and 2.

The PXRD spectrum has been recorded for the as made sample of compound **2** and compared to the simulated pattern of compound **1** （Figure 30）. Differences in the peaks show even though both compound **1** and **2** are composed of zinc metal centers, btc and tppe linkers, their phase are totally different. The unit cell data of compound **2** has been collected from the single crystal X-ray study. The comparison of compound **1** and **2** is listed in Table 8. From the unit cell data, compound **2** has a larger unit cell compared to **1**.

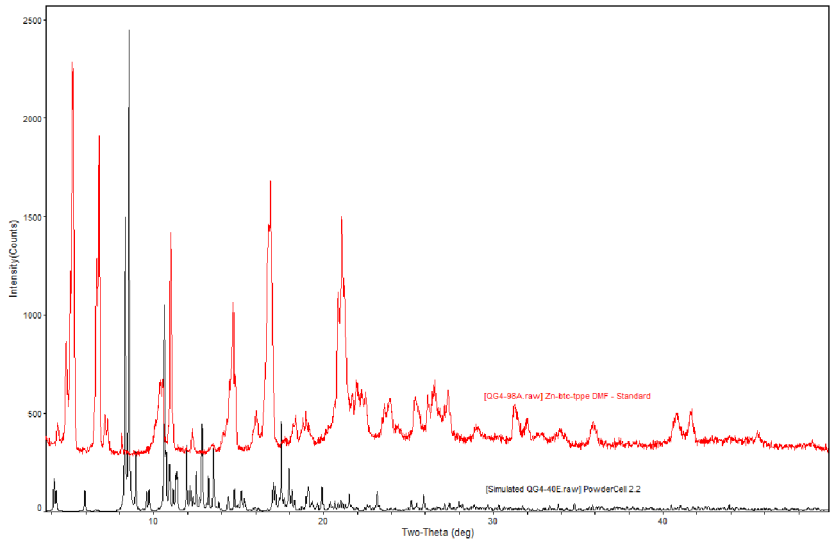

Figure 30. PXRD pattern of as-made compound **2** (top), along with simulated pattern of compound **1** (bottom).

Table 8. Unit cell data comparison of compound 1 and 2.

Unit Cell	Compound **1**	Compound **2**
a (Å)	10.117	34.519(4)
b (Å)	29.539	10.1639(11)
c (Å)	29.556	36.422(4)
α (degree)	91.446	90
β (degree)	93.321	94.507(5)
g (degree)	91.615	90
V ($Å^3$)	8811	12739(2)

3.2.3 Thermal stability of compound 2.

The thermal stability study of compound **2** was carried out via thermogravimetric analysis and PXRD measurement. The TGA curve (Figure 31) of as made compound **2** shows two different plateaus. The first one is from 60 °C to 100 °C with 3.0% weight loss, and the second one is from 250 °C to 360 °C with a further 18% weight loss from the first

plateau. The TGA curve of compound **1** only shows one plateau from 250 °C to 330 °C with a 25% weight loss, which corresponds to DMA guest molecules evacuating from the framework, confirmed by single crystal analysis. Compared to the as made compound **1** as made sample, there are two weight losses in **2**.

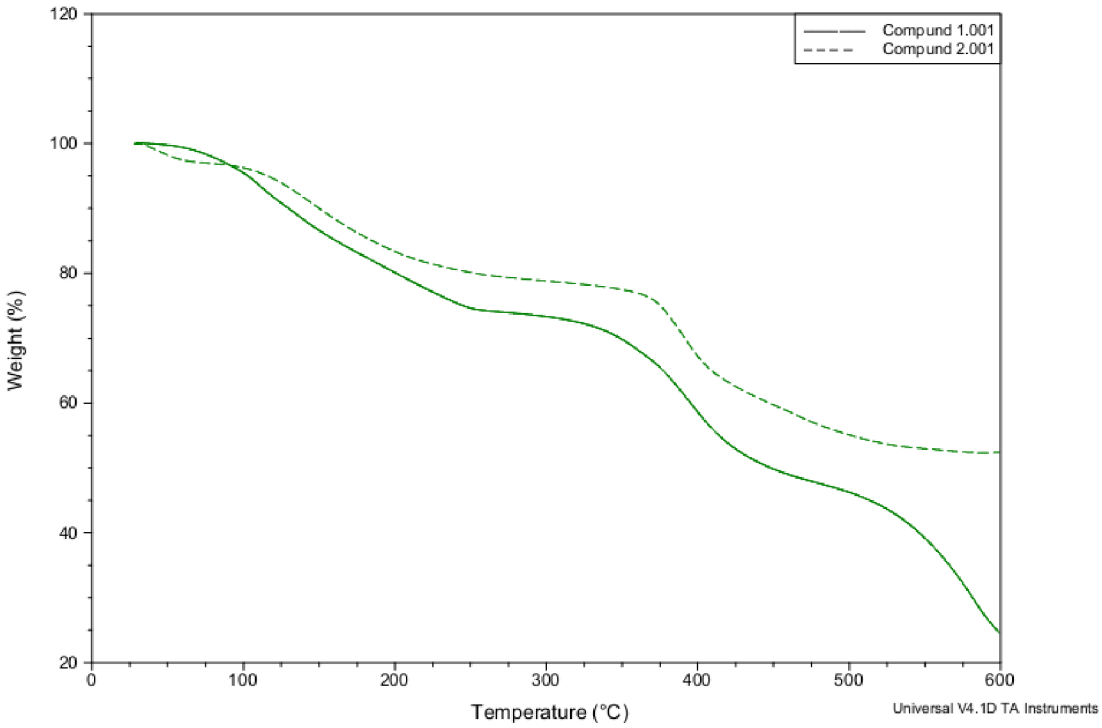

Figure 31. TGA of the as made sample of compound **1** (solid line) and **2** (dotted line).

The structural integrity of compound **2** after the removal of guest molecules has been studied. The major peaks of compound **2** sustain after the isotherms at 60 °C and 250 °C for 20 mins respectively. This shows the thermal stability of compound **2** is

actually better than compound **1** since the PXRD of **1** lost most of peaks after being heated at 250 °C directly (Figure 32). Thus compound **2** is a more robust structure than **1**.

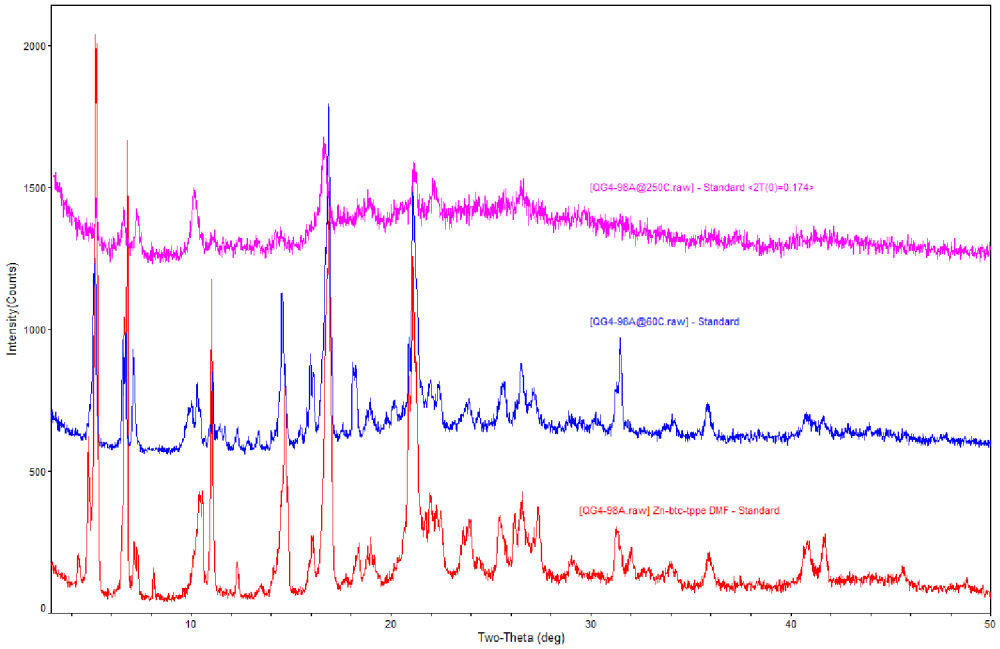

Figure 32. PXRD of compound **2** at different temperatures, room temperature (red), 80 °C (blue) and 250 °C(pink).

3.2.4 Optical properties of compound 2.

PL excitation and emission spectra of compound **2** have been measured at various temperatures (Figure 33) to study the optical properties of **2**. The emission maximum of compound **2** upon excitation with 440 nm light red shifts from 490 nm to 510 nm and 535 nm, at room temperature, 60 °C and 250 °C respectively. The excitation spectra of **2** at **r**oom temperature, 60 °C and 250 °C monitored at 480 nm, 500 nm and 525 nm emissions red shift, thus the intensity of the emission spectrum increases as the temperature increases. The UV spectrum (Figure 36) also indicates decreased band gap of compound **2** at 250 °C compared to it at room temperature and 60 °C.

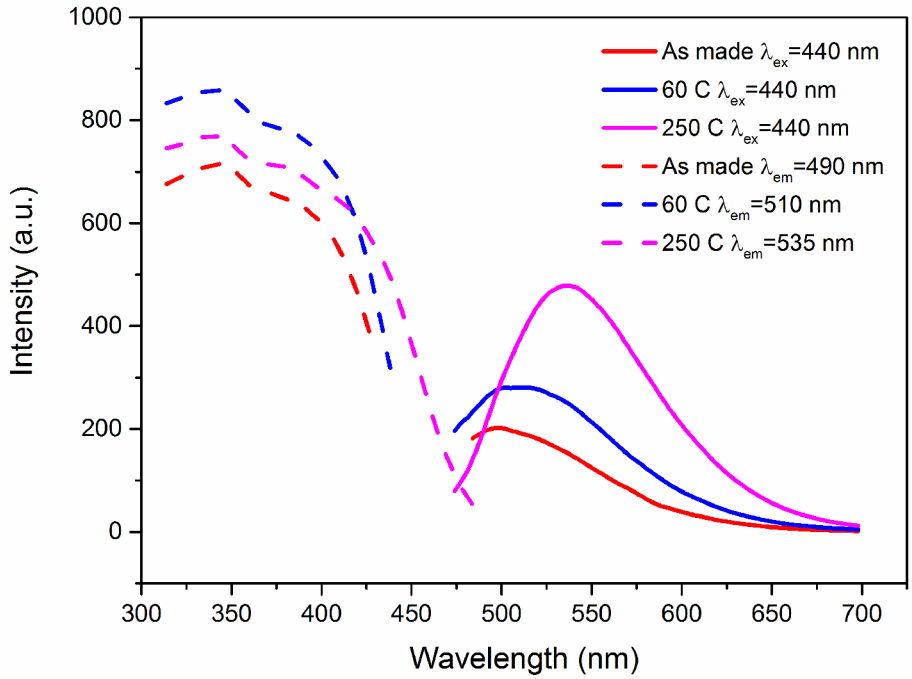

Figure 33. Emission spectra (solid lines) excited at 440 nm and excitation spectra (dotted lines) monitored at various emission wavelength (490 nm, 510 nm and 535 nm for room temperature, 80 °C and 250 °C respectively) of compound **2** at room temperature (red), 80 °C (blue) and 250 °C (pink).

Compound **2** shows 5 nm blue shift with both the emission and excitation spectra compared to **1** (Figure 34), which might be caused by the coordination condition difference between the two structures. The CIE coordinates of compound **2** is (0.35, 0.58), which is very close to that of YAG:Ce^{3+} (0.41, 0.56) (Figure 35).

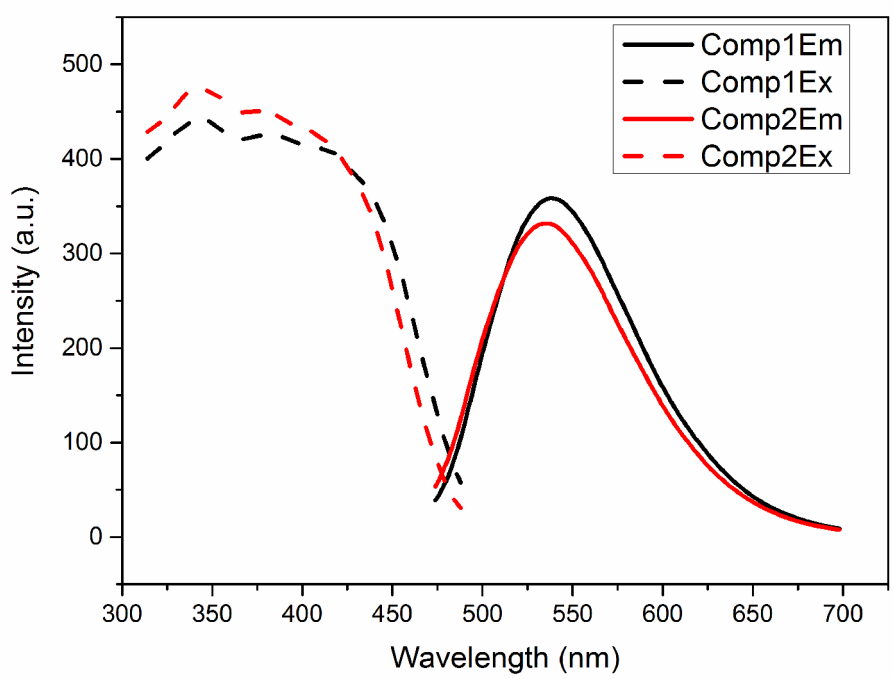

Figure 34. Emission spectra (solid line) excited at 440 nm and excitation spectra (dotted line) of compound **1** (black) and compound **2** (red, outgassed sample) monitored at 540 and 535 nm respectively.

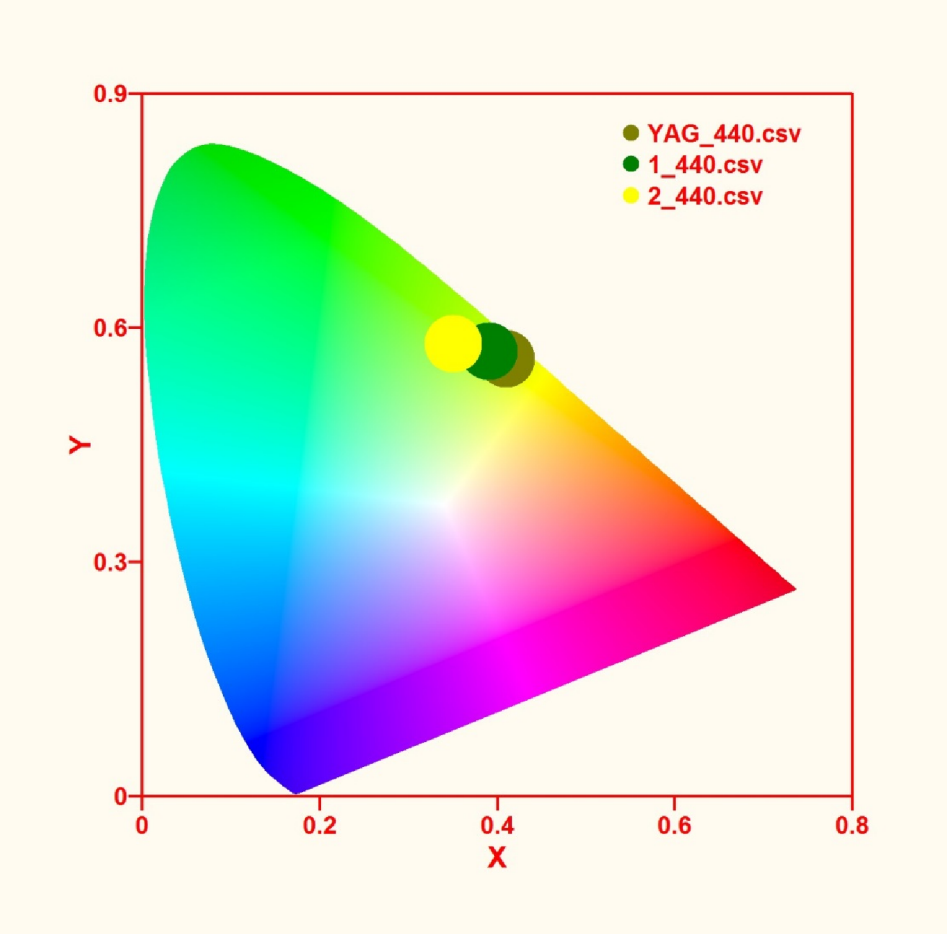

Figure 35. CIE coordinates of compound **2**: (0.35, 0.58), compound **1**: (0.39, 0.57) and YAG:Ce^{3+} (0.41, 0.56).

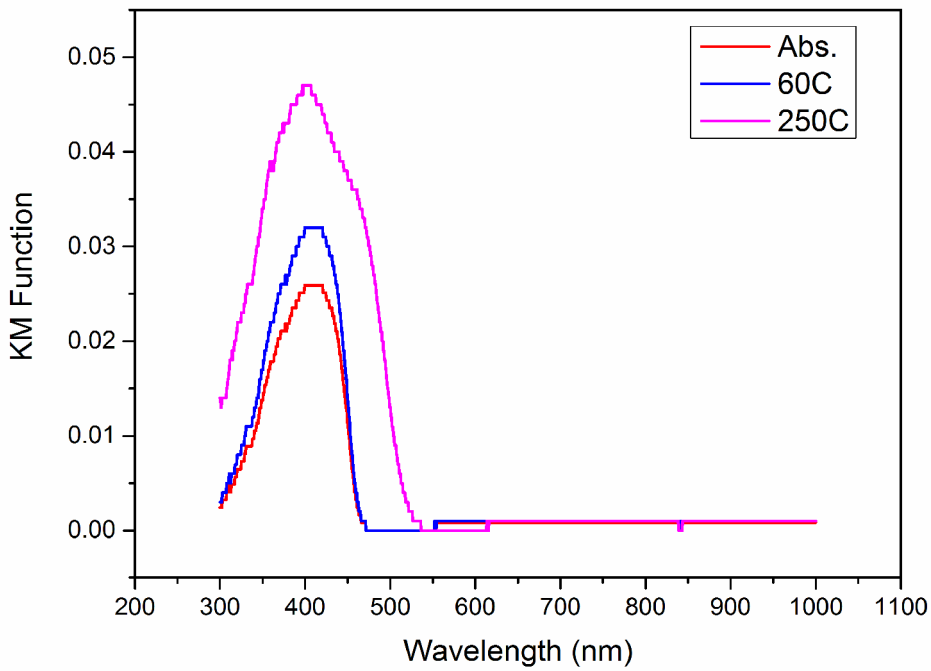

Figure 36. Optical absorption spectra of compound **2** at room temperature (red), 80 °C (blue) and 250 °C (pink).

3.3 Zn-fdc-tppe (Compound 3)

Compound **3**, composed of zinc ions, tppe and fdc (9-Fluorenone-2,7-dicarboxylate, Figure 37), has been synthesized and characterized. The ligand fdc is bidentate compared to the tridentate btc in compound **1** and **2**. Thus the structure of **3** is different from the previous two structures. The outgassed sample of 3 also emits yellow light upon excitation with blue light, indicating another potential candidate as a yellow phosphor for WLEDs.

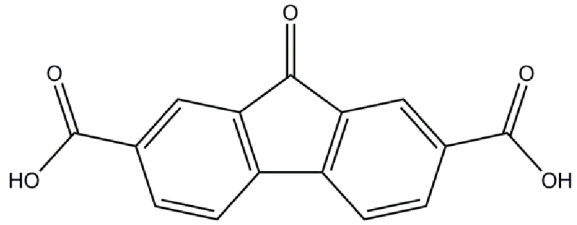

Figure 37. Ligand 9-Fluorenone-2,7-dicarboxylic acid (H_2fdc).

3.3.1 Synthesis of compound 3

Solvothermal reactions of $Zn(NO_3)_2 \cdot 6H_2O$, tppe, and 9-Fluorenone-2,7-dicarboxylic acid (H_2fdc) in dimethylacetamide (DMA) produced needle-shaped yellow crystals. 0.05 mmol (15 mg) $Zn(NO_3)_2 \cdot 6H_2O$, 0.05 mmol (13 mg) 9-Fluorenone-2,7-dicarboxylic acid, and 0.01 mmol (6.4 mg) tppe were dissolved in 14 ml dimethylacetamide (DMA) and 2ml isopropanol in a 20 ml glass vial. The vial was capped and ultrasonicated until the solution became transparent, and then heated in a 150 °C oven for 1 day. Needle shaped yellow crystals were isolated and washed with 10 ml DMA 3 times.

3.3.2 Phase comparison of compound 1-3.

The comparison of PXRD patterns of compound 1, 2 and 3 (Figure 38) show the phase difference of those three compounds.

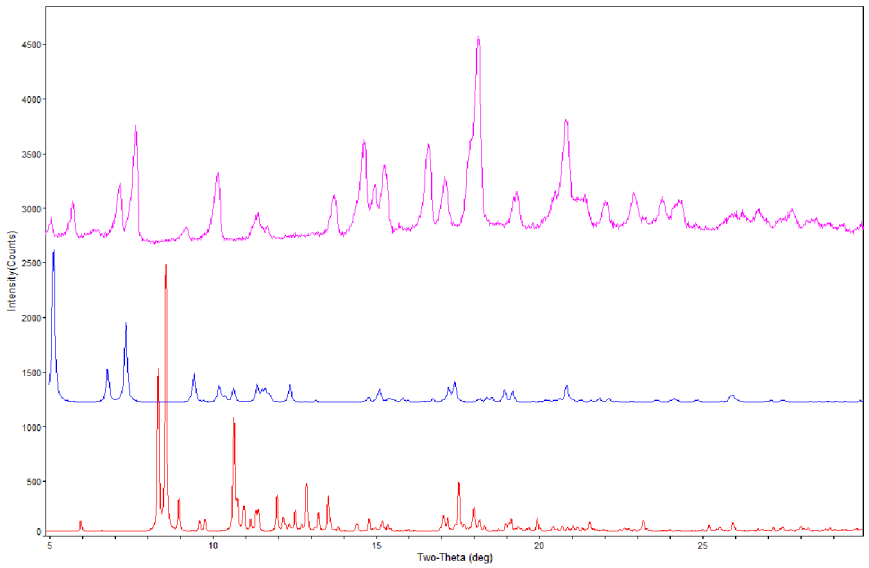

Figure 38. PXRD pattern of compound **1**(bottom, simulated), compound **2** (middle, simulated) and compound **3** (top, as made).

3.3.3 Thermal stability of compound 3.

Thermogravimetric analysis (Figure 39) exibits the two different weight losses, similar to compound **2**. The first plateau is from 50 °C to 80 °C with a 6% weight loss, while the second plateau is from 160 °C to 360 °C with a further 24% weight loss. The second plateau of compound **3** is much more flat than compound **2** and **1**. The PXRD of the as made sample after the isotherm at 200 °C for 20 mins (Figure 40) shows integrity of the structure, which indicates the good thermal stability of compound **3**.

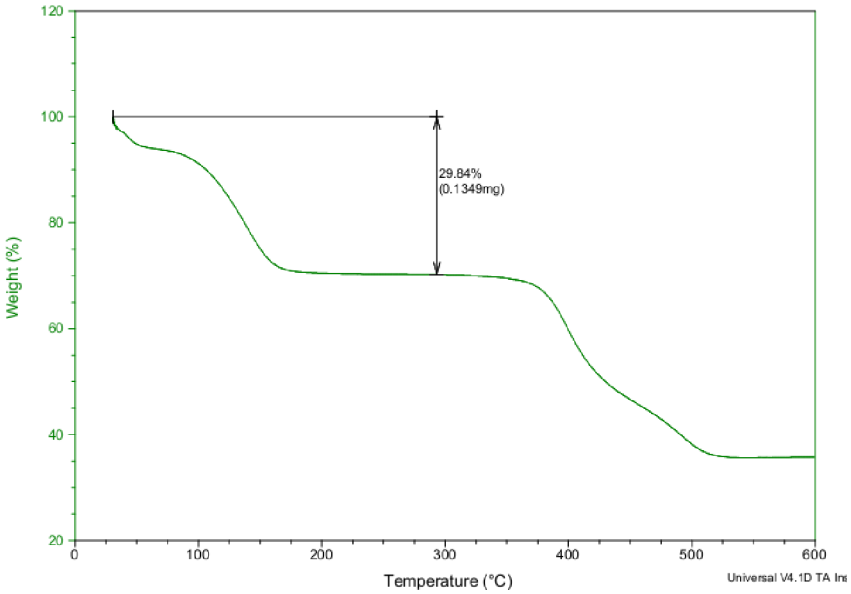

Figure 39. TGA of compound **3** as made sample.

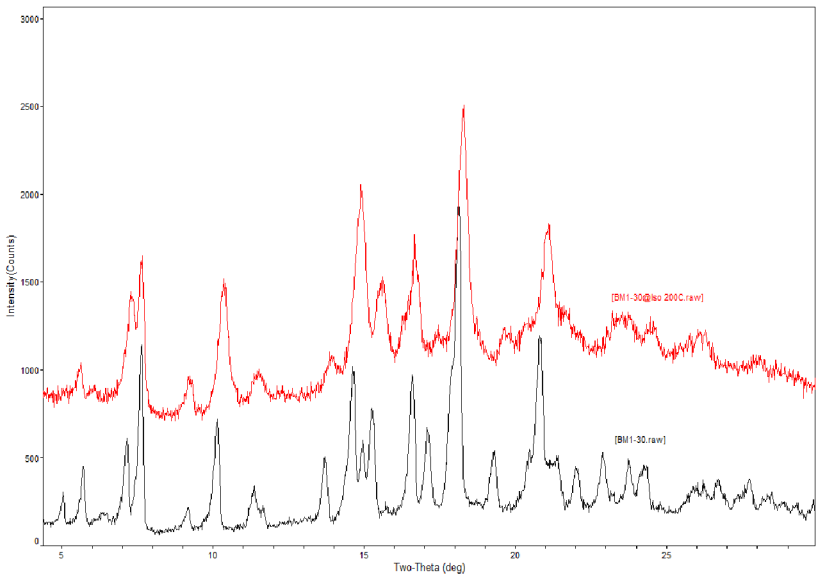

Figure 40. PXRD pattern of compound **3**, bottom (as made) and top (outgassed).

3.3.4 Optical properties of compound 3.

The PL spectra of tppe, as made and outgassed sample of compound **3** have been collected (Figure 41). While the as made sample of **3** emits 515 nm green light, the outgassed sample emits 525 nm light, both upon excitation of 365 nm wavelength light.

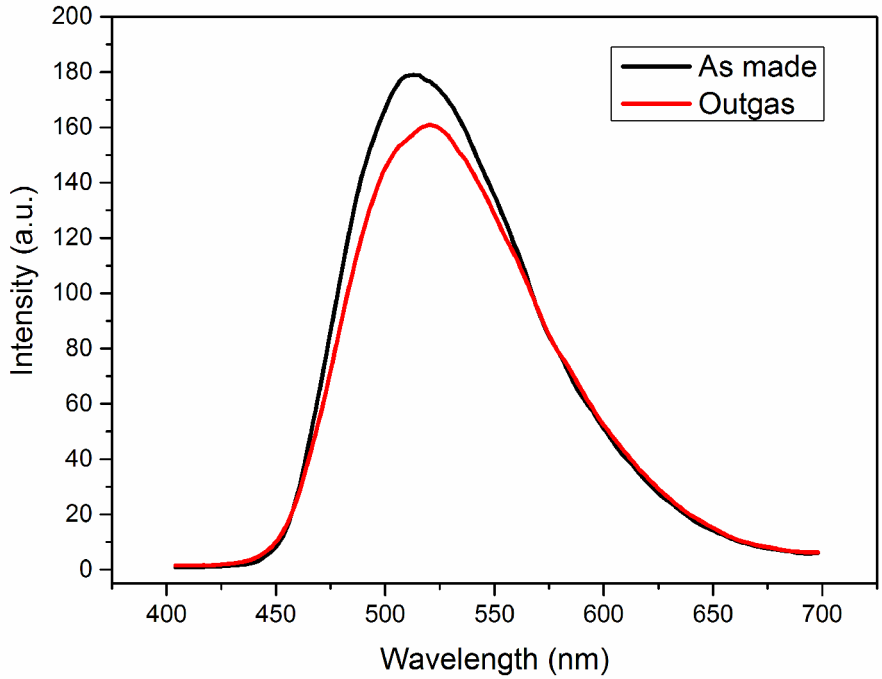

Figure 41. Emission spectra (solid lines) of tppe (red), compound **3** as made sample (black) and outgas sample (red) excited at 365 nm.

3.4 $Ni_2(bpdc)_2(tppe)$ (Compound 4)

Besides the 3 compounds described previously, another tppe based compound, $Ni_2(bpdc)_2(tppe)$ (compound **4**) has been synthesized and characterized too.

Our previous group member Jingming Zhang has synthesized and studied (Figure 42) a structure $Zn_2(bpdc)_2(tppe)$ (compound **5**). Compound **4** is synthesized as an analog structure of compound **5**. While compound **5** emits green light upon

excitation of near-violet light, compound **4** is not luminescent in visible range. This might be attributed to the fluorescent quenching effect of the paramagnetic Ni^{2+}, which is induced by the LMCT and the non-radiative relaxation of excitation energy.[8] The similar effect has been observed in other MOFs with paramagnetic metal centers, such as d^9Cu(II), d^7Co(II) and d^5Mn(II). The emission from paramagnetic transition metal compounds are usually not strong, which could be caused by the strong reabsorption of d-d transition of partially field d orbital.[31]

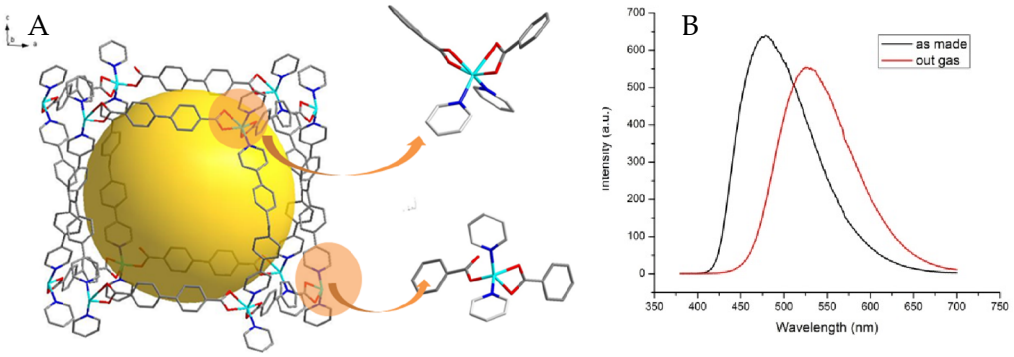

Figure 42. Compound **5**, synthesized, characterized and plotted by Jingming Zhang. A) Crystal structure of **5**. B) PL emission spectra (λ_{ex}=360 nm) of as made and outgassed sample of **5**.

3.4.1 Synthesis of compound 4.

Solvothermal reactions of $Ni(ClO_4)_2$, tppe, and bpdc in dimethylacetamide (DMA) produced needle-shaped green crystals. 0.05 mmol (14 mg) $Ni(ClO_4)_2$, 0.05 mmol (9 mg) biphenyl dicarboxylic acid, and 0.016 mmol (5 mg) tppe were dissolved in 10 ml dimethylacetamide (DMA) and 2ml isopropanol in a 20 ml glass vial. The vial was capped and ultrasonicated until the solution became transparent, and then heated in a

150 °C oven for 1 day. Needle shaped yellow crystals were isolated and washed with 10 ml DMA 3 times.

3.4.2 Single crystal data of compound 4.

Single-crystal synchrotron X-ray diffraction data of compound **4** were collected at 150 K on a D8 goniostat equipped with a Bruker APEXII CCD detector at Beamline 11.3.1 at the Advanced Light Source (ALS) in Lawrence Berkeley National Laboratory, using synchrotron radiation tuned to λ= 0.7749 Å. The structure was solved by direct methods and refined by full-matrix least-squares on F2 using the Bruker SHELXTL package.

Compound **4** crystallized in the monoclinic space group C 2/m with the general formula $[Ni_2(bpdc)_2(tppe)]$. The framework is built on primary building unit comprised

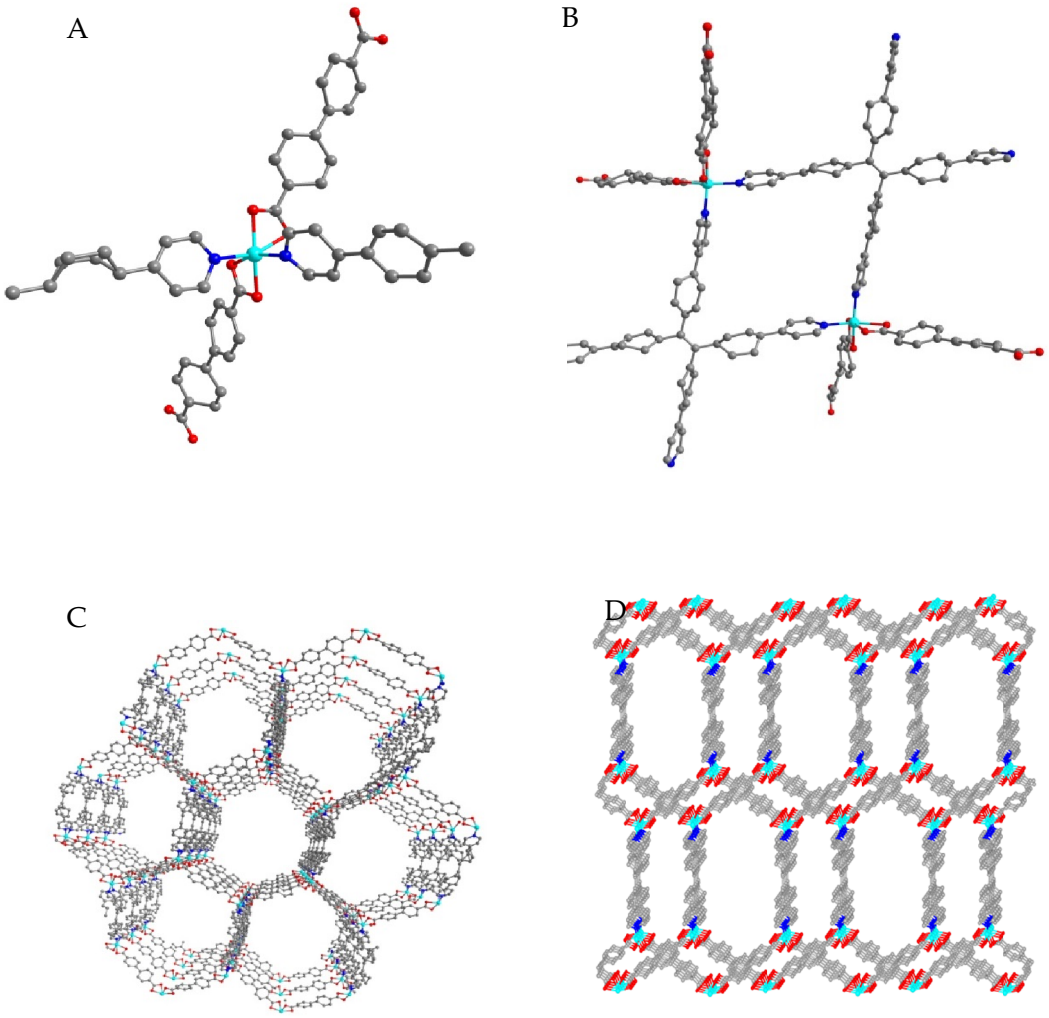

Figure 43. Crystal structure of compound **4**. A) Primary building unit. B) PBU connected by bpdc and tppe. C) 1D channel view along *c* axis. D) 2 fold interpenetration view along *c* axis.

Table 9. Single crystal data for compound 4.

Empirical formula	$Ni_2O_8C_{74}H_{48}N_4$
Formula weight	1238.54

Temperature	150(2) K	
Wavelength	0.7749 Å	
Crystal system	monoclinic	
Space group	C 1 2/m 1	
Unit cell dimensions	a = 26.410(7) Å	α= 90.000°.
	b = 41.365(13) Å	β= 120.718(3)°.
	c = 17.190(4) Å	γ= 90.000°.
Volume	16144.3(80)Å^3	
Z	4	

of octalhedrally coordinated Ni^{2+} (Figure 43A). A Ni^{2+} coordinated to two nitrogen atoms (from two different tppe ligands) and four oxygen atoms (from two carboxylate groups of two different bpdc ligands) (Figure 43B). A bpdc linker is connected to two PBUs and a tppe linker is connected to four PBUs (Figure 43B). The PBUs are coordinated by the linkers to form a 3D net with 1D channel along *c* axis (Figure 43C). Two such 3D nets interpenetrated to form the overall framework (Figure 43D).

3.4.3 Phase comparison of compound 4 and compound 5.

The PXRD patterns (Figure 44) of as made sample of compound **4** has less peaks compared to the simulated sample of compound **4**, which might be attributed to the incomplete solved single crystal structure. The comparison of both patterns to simulated pattern of **5** show the phase difference of **4** and **5**, even though both of them have the $[M_2(bpdc)_2(tppe)]$ formula.

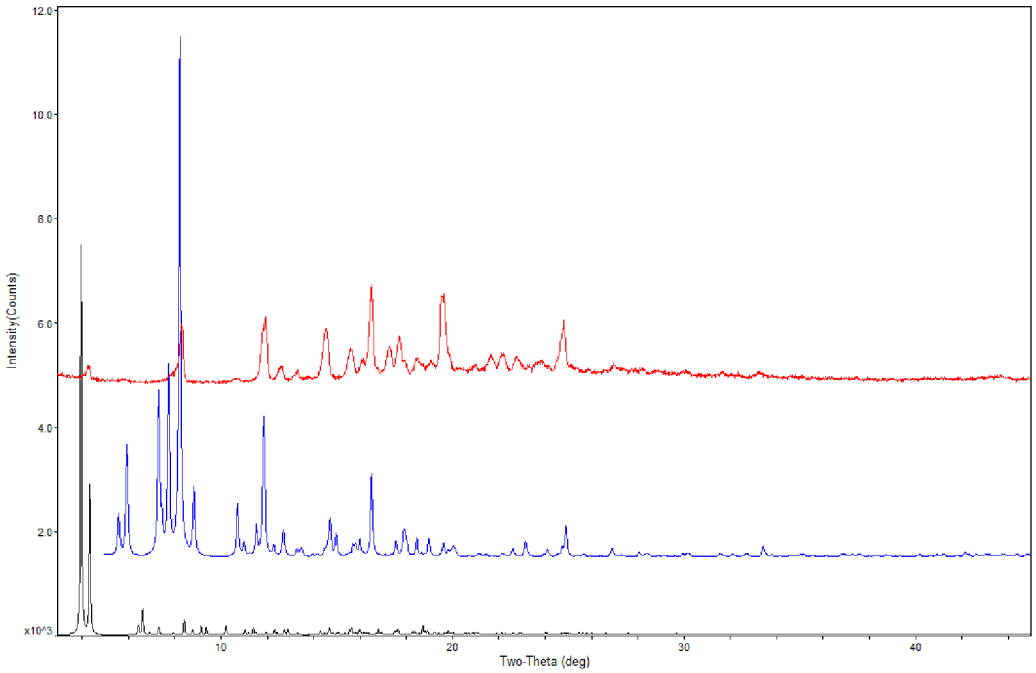

Figure 44. PXRD pattern of compound **4** (top), simulated pattern of **4** (middle), and simulated pattern for $Zn_2(bpdc)_2(tppe)$[74] (bottom).

3.3.4 Thermal stability of compound 4.

The TGA curve (Figure 45) shows compound **4** has a plateau from 200 °C to 380 °C. However, the PXRD at the plateau have lost all of the peaks, which means direct heating will cause the collapse of the structure.

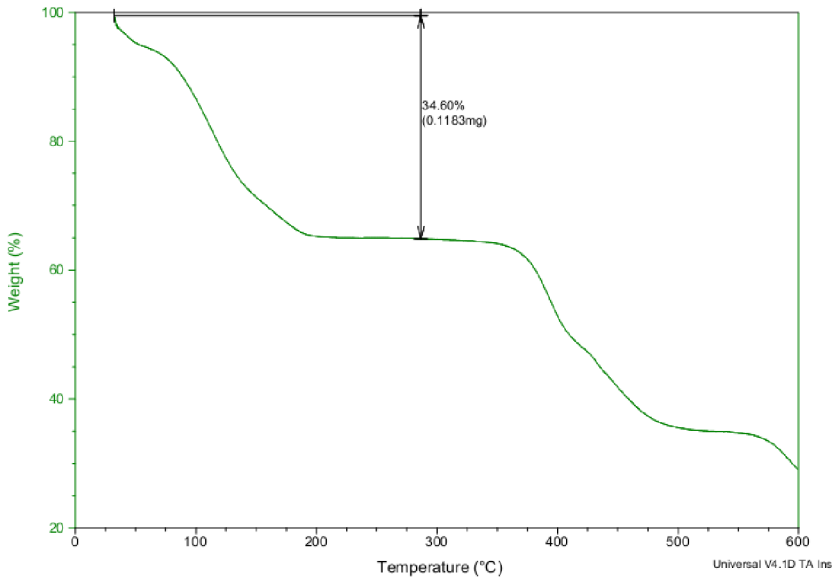

Figure 45. TGA of as-made sample of compound **4**.

3.5 Conclusion

Three new structures based on 1,1,2,2-tetrakis(4-(pyridin-4-yl)phenyl)ethene (tppe) have been synthesized and characterized. Both outgassed samples of **2** and **3** could emit yellow light upon excitation with blue light, which makes the two structures possible candidates as yellow phosphors for WLEDs. **4** doesn't have luminescence, which may be caused by the paramagnetic ion Ni^{2+}.

4. Hydrocarbon adsorption on metal organic frameworks

4.1 Introduction

As mentioned in chapter 1, metal organic frameworks have been intensively studied for their adsorption related properties and applications. Our group has made efforts not only in studying the adsorption applications of MOFs, but also understanding the fundamental aspects occurring during the adsorption process. Commensurate adsorption is a fundamentally important concept. Our group has studied a few examples of commensurate adsorption on MOFs, such as the propane/butane adsorption on Cu(hfipbb)(H_2hfipbb)$_{0.5}$; the ethanol, propanol and butanol adsorption on [$Co_3(HCOO)_6$]·DMF; and benzene adsorption on [$Zn_2(bpdc)_2(bpee)$]·2DMF. In this work, we continue to explore and investigate commensurate adsorption on two selected MOF compounds.

4.2 Commensurate to incommensurate transition of hydrocarbon adsorption in Ca(sdb)

Note: A manuscript resulted from this work is currently under preparation.

4.2.1 Introduction

As the adsorption amount, location and orientation of adsorbates are controlled by the pore size and shape of adsorbents in commensurate adsorption, commensurate

adsorption usually takes place when the pore sizes are small enough to confine the adsorbates. Ca(sdb) has been selected based on such consideration.

Ca(sdb) is a robust coordination framework with permanent microporosity (18% void space based on PLATON). It is a three-dimensional network with 1D chains of corner-sharing CaO6 octahedra along the crystallographic [010] direction. Remarkably, the activated form does not readsorb water vapor from the atmosphere and remains crystalline over a long period of time. The single crystal X-ray diffraction studies on the activated material show that it retains its structural connectivity, with an estimated pore size of ~5 × 5 Å. With this small pore size, it is highly possible that some adsorbates with suitable length and shape might have commensurate adsorption on the structure. Thus a preliminary study of the adsorption simulation on Ca(sdb) has been carried out.

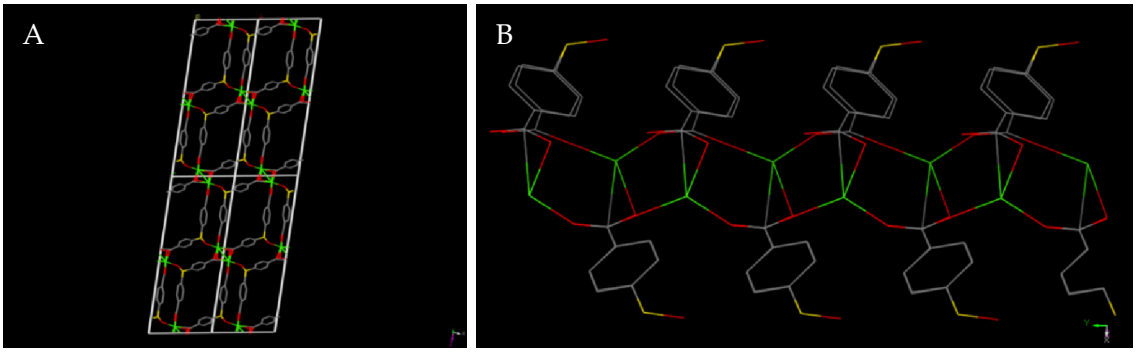

Figure 46. A) Supercell of Ca(sdb) view along the *b* axis; B) a channel of framework view along the *c* axis.

4.2.2 Simulations of alkanes adsorption on Ca(sdb)

Simulated adsorptions were computed using Accelrys Cerius2 Sorption software (Accelrys). A Monte Carlo method was used in this adsorption simulation, in which the position of adsorbates molecules were generated and accepted when their insertions are energetically favored. Burchard-Universal force-field was used (Burchard 1993).

Helium Simulation was carried out at the condition of 1 K, 100 atm on a 3×5×2 supercell of Ca(sdb) to make sure helium moves to the corners of the pore to show the pore shape. Simulated helium adsorption data illustrates that the channels of Ca(sdb) are zig-zag shaped, with a total of two segments (a “zig” and a “zag”) per unit cell (Figure 47).

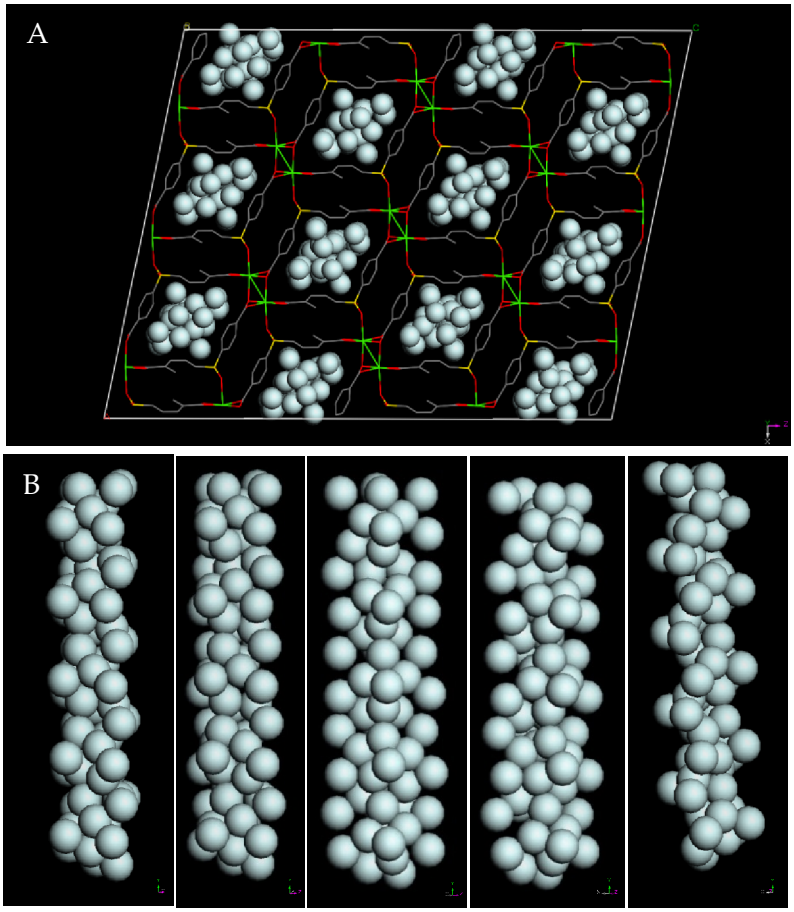

Figure 47. A) He simulation on RPM4 supercell view along *b* axis; B) He atoms showing the shape of the cage segment.

Considering the pore size and length, short chain alkanes have been chosen to be screened in the simulation. The simulated adsorptions of C1-C7 have been carried out on Cerius2 software. Figure 48, A-D shows random methanol uptake in the channel,

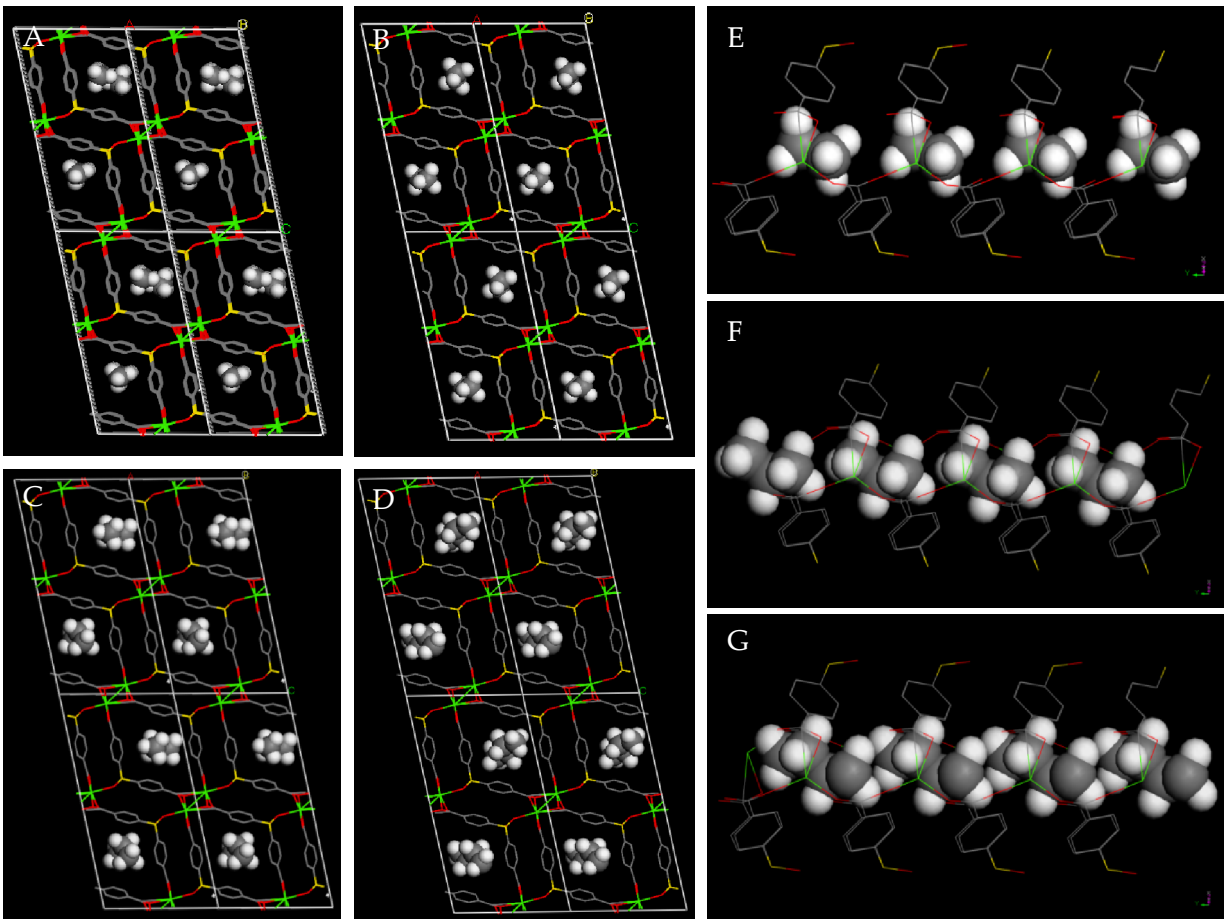

Figure 48. Methane (A), ethane (B), propane (C) and n-butane (D) adsorption simulation on Ca(sdb) view along b axis. Ethane (E), propane (F) and n-butane (G) adsorption simulation on Ca(sdb) view along *a* axis.

while ethane, n-propane and n-butane have only one molecule per cage. Thus it is highly possible that ethane, propane and n-butane adsorption on Ca(sdb) are commensurate adsorption. The assumption could be further confirmed by Figure 41, E-G, in which the molecules of ethane, propane and n-butane are packed along the framework with the same orientation of neighboring molecules. The length of n-butane is ~5.6 Å, which is close to the unit cell length along *b* axis, 5.54 Å (Table 10). It is suggested that longer hydrocarbons will straddle two segments and won't fit the pore shape, which is not commensurate adsorption. This has been confirmed by n-hexane adsorption simulation on Ca(sdb) (Figure 49).

Table 10. Molecular size of hydrocarbons.

Adsorbate	Size (Å)			
	Length		Diameter	
	L1	L2	D1	D2
Ethane	3.2	3.9	2.1	2.8
Propane	4.4	5.1	2.9	3.6
n-Butane	5.6	6.4	2.9	3.6
n-Pentane	6.9	7.7	2.9	3.6
n-Hexane	8.2	8.9	2.9	3.6

The size of each molecule is measured by its molecular length and cross section as described in Ref. 71 [J. Li et. al. Commensurate Adsorption of Hydrocarbons and Alcohols in Microporous Metal Organic Frameworks. *Chemical Reviews* **112**, 836-868 (2012)].

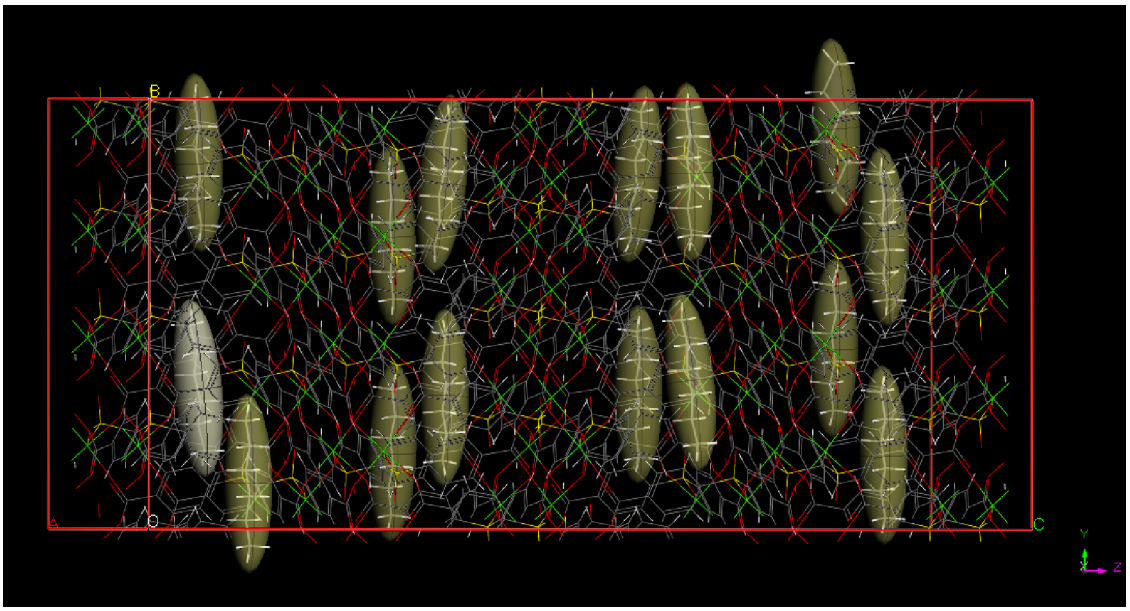

Figure 49. n-hexane adsorption simulation on Ca(sdb) view along *a* axis.

Thus, from the simulation data, there would be a commensurate to incommensurate transition of hydrocarbon adsorption on Ca(sdb). And we need to collect experimental data to further study this phenomenon.

4.2.3 Experimental Data on Ca(sdb).

In order to study the phenomenon in-depth, both adsorption experiments of C2-C7 alkanes/alkene on Ca(sdb) and C2-C7 adsorbed Ca(sdb) single crystal analysis have been carried out. Table 11 lists the experimental results.

Table 11. Summary and comparison of the C_2-C_7 adsorption in Ca(sdb) by gas-adsorption, simulation and single crystal X-ray diffraction techniques.

Adsorbate	Uptake [a] (wt %)	Uptake (mmol/g)	Uptake, no. molecule/unit cell (no.molecule/segment) Simulation	Adsorption Expt [a]	Crystallography	Heats of Adsorption (*Qst*)
Ethane (C_2)	4.26[a]	1.42	2(1)	1.95(0.97)	1.14 (0.64)	35.7
Propane (C_3^0)	5.1[a]	1.15	2(1)	1.62 (0.81)	0.66 (0.33)	48.8
Propene ($C_3^=$)	6.30[a]	1.50	2(1)	2.06 (1.03)	1.74 (0.87)	44.8
Butane (C_4)	8.18[a]	1.41	2(1)	1.94 (0.97)	1.19 (0.595)	52.6
Pentane (C_5)	5.47[b]	0.76	1(0.5)	1.08 (0.54)	1.26 (0.632)	55.8
Hexane (C_6)	5.79[b]	0.67	0.94(0.47)	1.00 (0.5)	0.42 (0.21)	72.9
Heptane (C_7)	6.38[b]	0.64	0.8(0.4)	0.9 (0.45)	0.34 (0.17)	88.8

[a] Uptake value for C_2H_6, C_3H_6, C_3H_8 and C_4H_{10} are calculated at 298 K and 1 atm pressure

[b] Uptake value for n-C_5H_{12}, n-C_6H_{14} and n-C_7H_{16} are calculated at 303 K and 180 Torr, 50 Torr and 15 Torr repectively.

[c] *Qst* values were calculated from the adsorption isotherms under experimental condition.

Note: the crystallography data was collected by Debasis Banerjee, the ethane-butane adsorption data was collected by Jacek Jagiello.

It is clear that C2-C3 are commensurate adsorption and n-C5-C7 are incommensurate adsorption on Ca(sdb), from the simulation, adsorption and crystallography data.

However, for n-C4, the simulation and adsorption results are close to commensurate adsorption, while the crystallography information, the n-C4 adsorption on Ca(sdb) is incommensurate adsorption. The investigation of the alkane/alkenes adsorption on Ca(sdb) via simulation, adsorption and crystallography study clearly show the commensurate to incommensurate transition of hydrocarbon adsorptions in MOFs, which is the first time.

4.2.4 Detail experimental data of n-C5, n-C6 and n-C7 adsorption on Ca(sdb).

The adsorptions of n-C5 on Ca(sdb) at low temperatures, 303, 313 and 323 K, have quite close uptakes and isotherms (Figure 50), which indicate the adsorption is close to pore filling adsorption. In order to obtain isosteric heat of adsorption, isotherms with larger difference are required. Thus n-C5 on Ca(sdb) isotherms at 363, 373, 383 and 393 K are collected (Figure 51). Figure 52 shows the adsorption and desorption

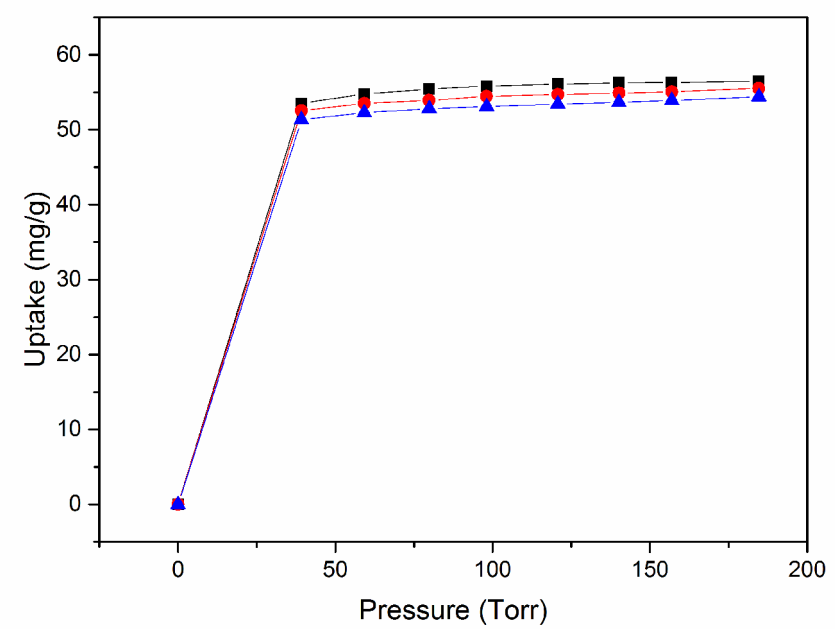

Figure 50. n-C5 adsorption on Ca(sdb) at 303 (black), 313 (red) and 323 (blue) K.

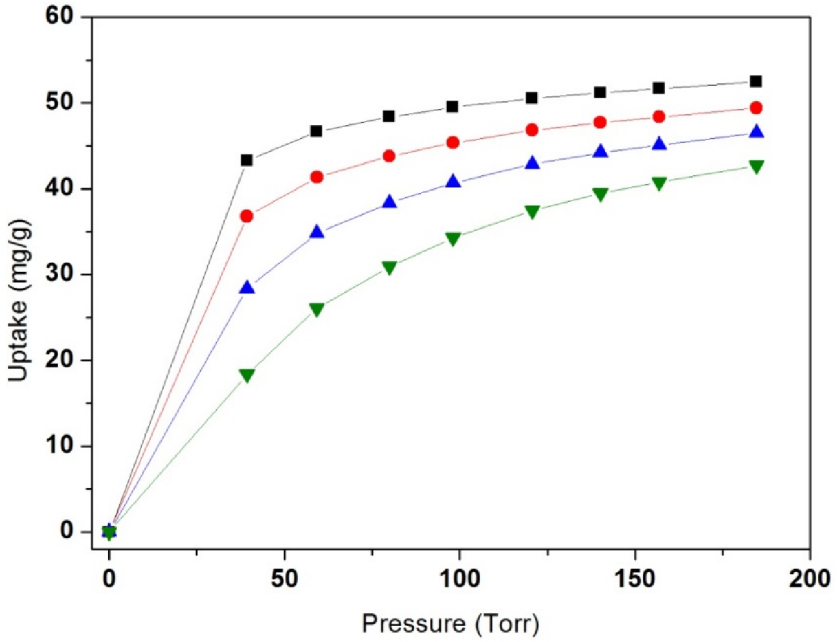

Figure 51. n-C5 adsorption at 363 (black), 373 (red) ,383 (blue) and 393 (green) K on Ca(sdb).

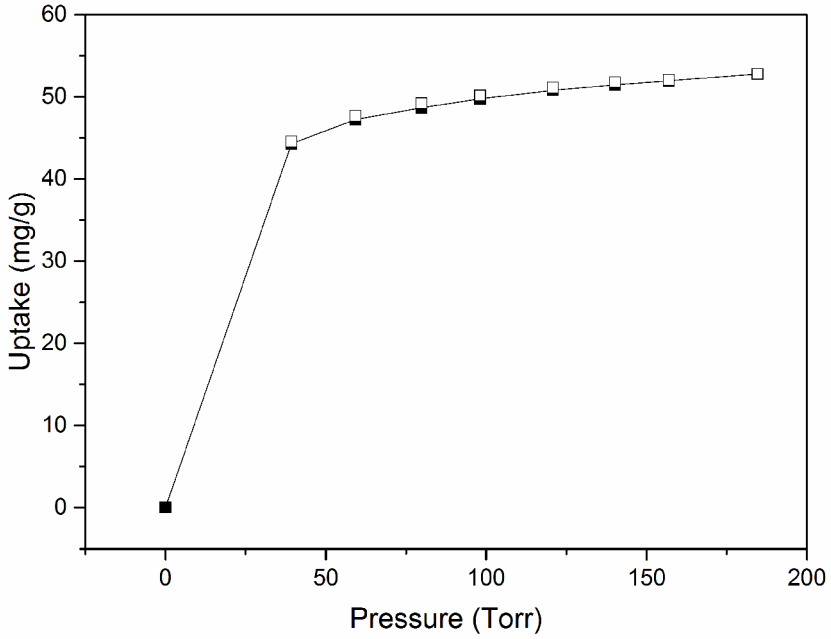

Figure 52. n-C5 adsorption and desorption isotherms at 363 K.

isotherms of the n-C5 adsorption on Ca(sdb), indicating equilibrium has been reached.

Similar to n-C5, the adsorptions of n-C6 and n-C7 on Ca(sdb) at low temperatures, 303, 313 and 323 K, have quite close uptakes and isotherms at each temperature as well (Figure 53, 55). n-C6 and n-C7 on Ca(sdb) isotherms at 363, 373, 383 and 393 K are collected separately (Figure 54, 56) to calculate the isosteric heat of adsorption. The powder X-ray diffraction patterns (Figure 57) of the sample before and after adsorption experiments have been collected to confirm the structure integrity upon adsorption measurement.

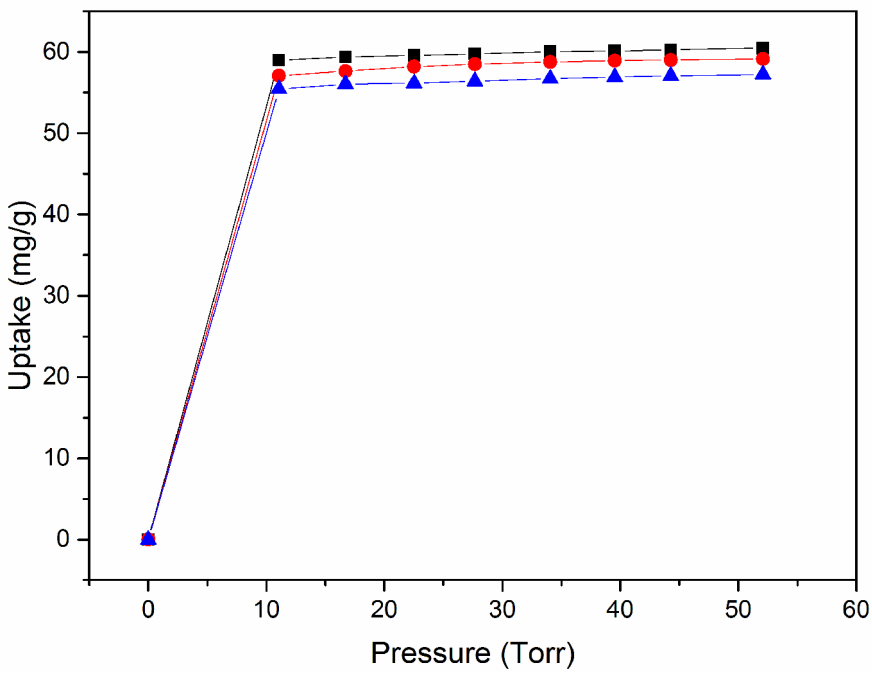

Figure 53. n-C6 adsorption on Ca(sdb) at 303 (black), 313 (red) and 323 (blue) K.

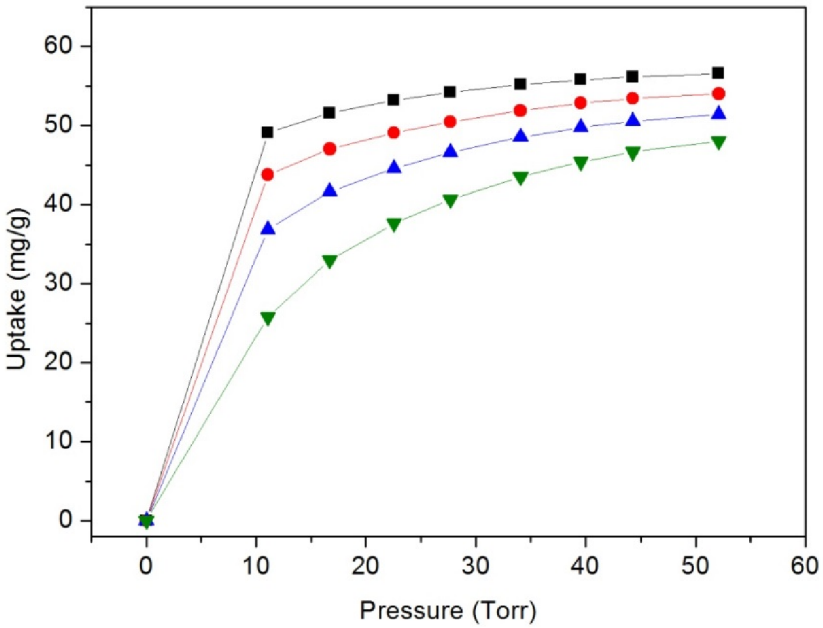

Figure 54. n-C6 adsorption at 363 (black), 373 (red) ,383 (blue) and 393 (green) K on Ca(sdb).

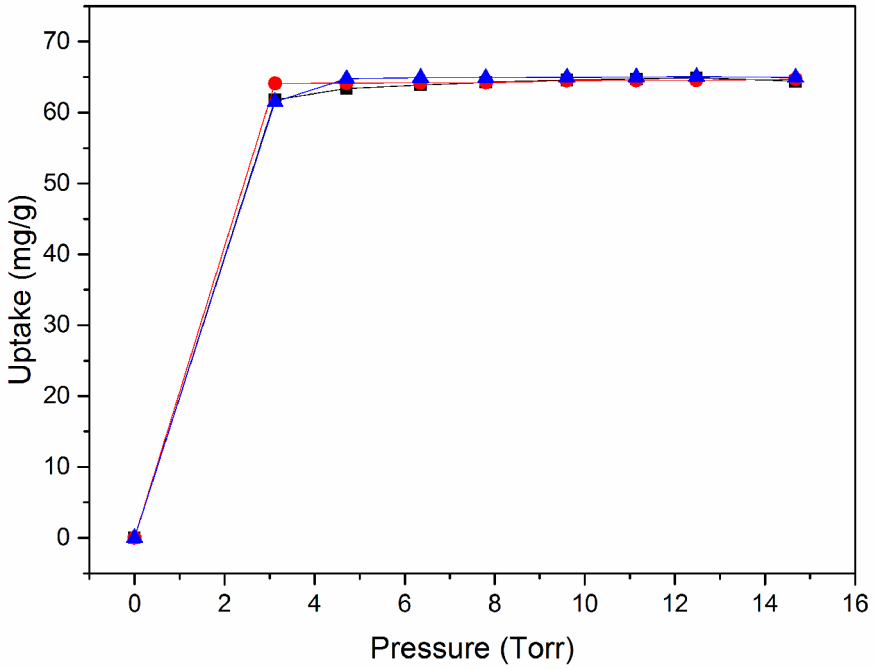

Figure 55. n-C7 adsorption on Ca(sdb) at 303 (black), 313 (red) and 323 (blue) K.

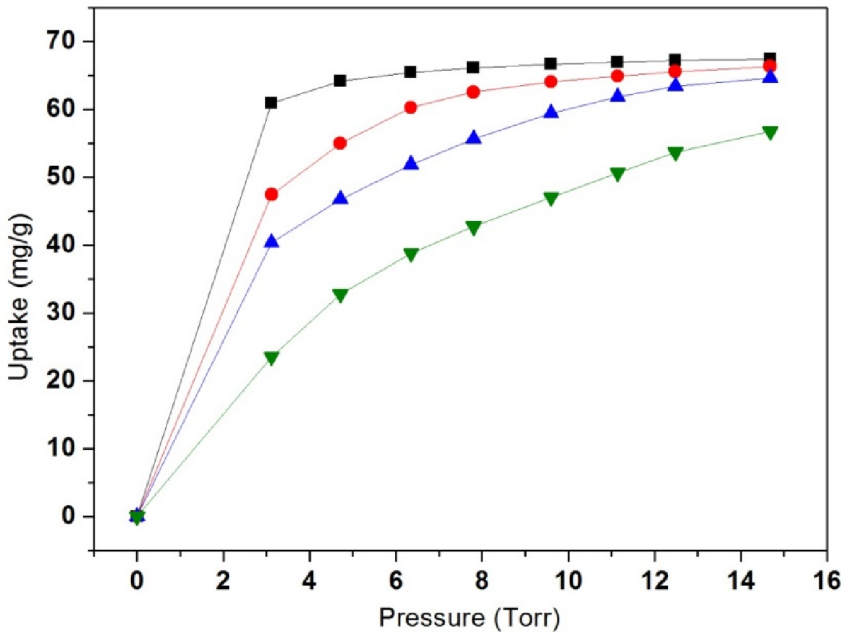

Figure 56. n-C7 adsorption at 363 (black), 373 (red) ,383 (blue) and 393 (green) K on Ca(sdb).

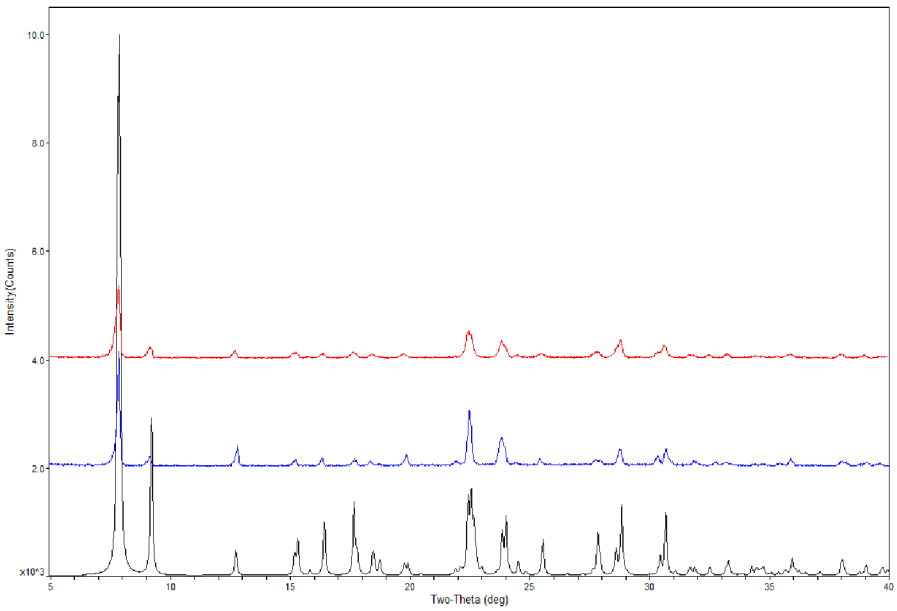

Figure 57. PXRD patterns of simulated (black), as made (blue) and post-adsorption (red) sample of Ca(sdb).

4.2.5 Conclusion.

In this study, the author and coauthor worked to study the commensurate to incommensurate transition of alkane/alkenes adsorption in Ca(sdb). Combining the simulation, adsorption and crystallography data, the C2-C3 adsorptions are commensurate adsorption and C5-C7 adsorptions are incommensurate adsorption. While n-C4 shows the transition from commensurate to incommensurate adsorption. This study is a comprehensive study of commensurate adsorption phenomenon and provides the direct evidence of the transition.

4.3 Commensurate Adsorption in $[Zn_2(bpdc)_2(bpe)]\cdot 2DMF$ (RPM4)

Note: This work has been published in the work of Ref. 71.

Previous study by our group shows that $[Zn_2(bpdc)_2(bpee)]\cdot 2DMF$ (RPM3-Zn), a flexible structure with a 1D channel along the *b*-axis with 6.75 Å segment, exhibit commensurate adsorption with benzene, p-xylene, o-xylene and C2-C4 alcohols. While RPM4 is an isotypic structure of RPM3, we are interested if commensurate adsorption also exists in RPM4.

4.3.1 Structure of RPM4.

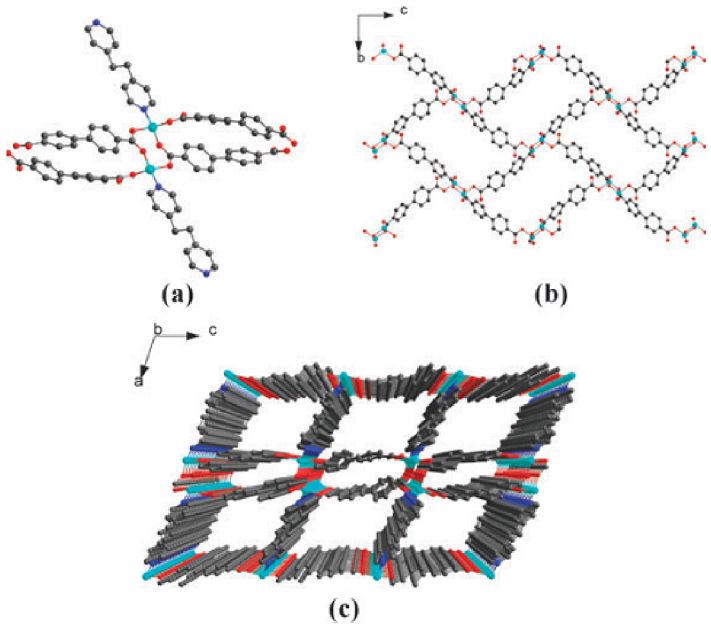

Figure 58. Views of the crystal structure of 1. (a) the SBU and the coordination around the Zn(II)2 pair; (b) the single 4^4 brick-like net; (c) perspective view of 1 showing the 1D channels along the b-axis(DMF molecules are removed for clarity). Zinc cyan, Carbon gray, Oxygen red, Nitrogen blue. Reprinted with permission of Ref. 75 Copyright @2010 Royal Society of Chemistry

As shown in Figure 56, each zinc atom is connected to three oxygen atoms from three bpdc and one nitrogen atom from a bpe ligand (Figure 58A). A secondary building unit composed of and eight atoms ring, - $Zn_2(COO)_2^{2+}$, is connected to four neighboring SBU to form a 4^4 brick-like net (Figure 58B). Bpe ligand serves as a pillar ligand to connect the 2D layer formed by the interpenetration of two identical nets and gives rise to an overall 3D structure with 1D open channels extending along the crystallographic b-axis (Figure 58C).[75] Adapted with permission of Ref. 75 Copyright @2010 Royal Society of Chemistry

4.3.2 Simulation on RPM4.

In order to predict if commensurate adsorption exists in RPM4, a simulation screening has been carried out on Cerius 2 software.

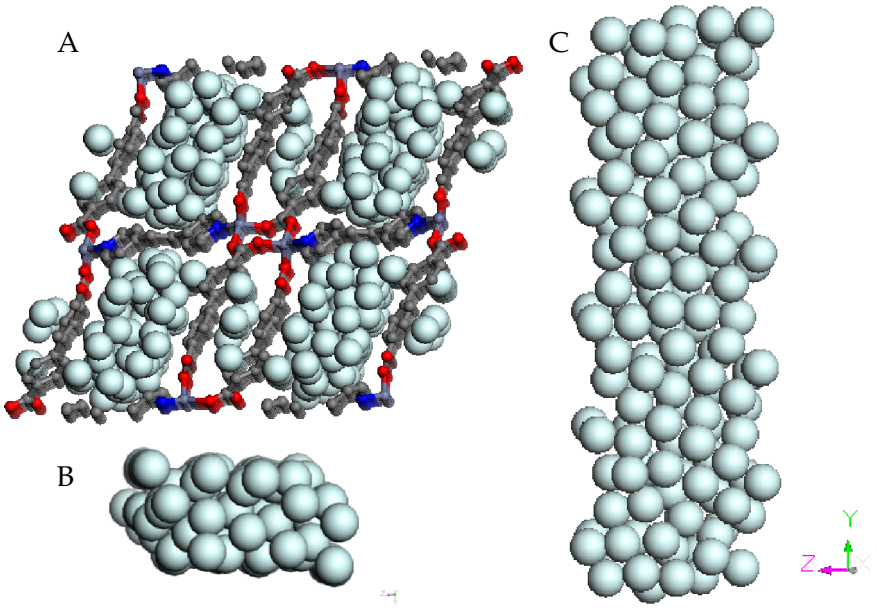

Figure 59. A) He simulation on RPM4 supercell view along *b* axis; B) He atoms showing the shape of the channel along *b* axis; C) He atoms showing the shape of the segments along *a* axis.

Helium simulation (Figure 59A) on a supercell of RPM4 at 1 K, 101 KPa with Burchart Universal as the forcefield shows the 1D channel along the *b* axis has a rectangular opening with ~4.5 x 8.0 Å (Figure 59B) and the segment along the b axis has a repeatable length that corresponds to the unit cell length of b axis, 6.75 Å (Figure 59C). Also, one unit cell possesses four cages/segments according to the simulation data.

The adsorption simulations of various hydrocarbons and alcohols on RPM4 have been carried out. Alcohols from C2 to C6, straight and branched alkanes, aromatic

hydrocarbons such as benzene, p-, o-xylene, and ethylbenzene adsorption simulations on RPM4 show that both ethanol and n-propanol have uptake ~ 2 molecules/segment, while the other hydrocarbons and alcohols have ~1 molecule/segment uptake. The adsorption simulation snapshots of benzene on RPM4 have been shown in Figure 60.

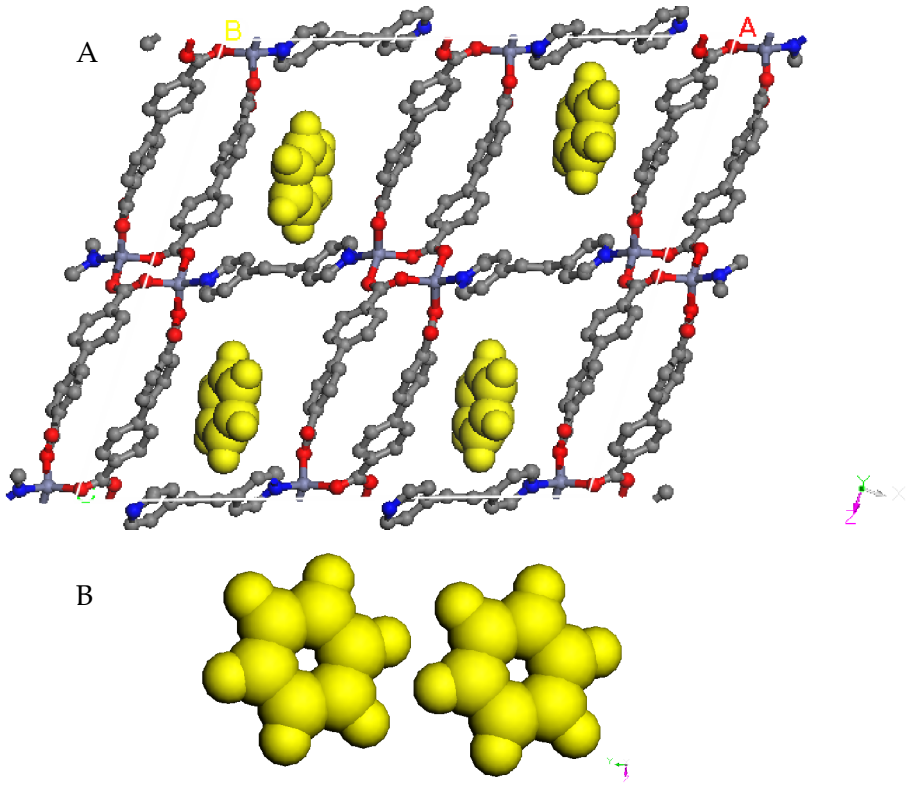

Figure 60. Benzene adsorption simulation on 1×2×1 supercell of RPM4. A) View from *b* axis; B) Benzene in one channel view from *a* axis.

4.3.3 Experimental data on RPM4.

The adsorption experiments of hydrocarbons and alcohols on RPM4 have been carried out at 303 K, under saturated vapor pressure of each hydrocarbon and alcohol at 291 K.

Table 12. Adsorption data on RPM4

Adsorbate	Qobs (mg/g)	Qobs (mol/cage)	Qsim (mol/cage)	Length (Å)	Width (Å)
Benzene	130.0	1.19	1.0	5.8	5.1
P-xylene	124.6	0.84	1.0	7.4	5.1
O-xylene	80.2	0.54	1.0	6.6	6.3
Ethylbenzene	78.8	0.53	1.0	7.9	5.1
MeOH	88.4	1.98	-	4.1	3.0
EtOH	91.7	1.43	2.0	5.1	3.0
n-PrOH	125.8	1.50	2.0	6.3	3.0
n-BuOH	128.0	1.24	1.0	7.6	3.0
n-Pentanol	106.6	0.87	1.0	8.8	3.0

The adsorption of Benzene and p-xylene show commensurate adsorption on RPM4, while two other isomers of p-xylene only show half amount of uptake of p-xylene, because of their incompatible molecular shape and length to the segment of RPM4 (o-xylene is bulkier than benzene and p-xylene, while ethylbenzene has longer molecular length than p-xylene which may prevent it from fitting the segment of RPM4).

The adsorption of alcohols shows methanol and n-pentanol have 2 and 1 molecules uptake per unit cell segment, which means they are commensurate adsorption. While the C2-C4 alcohols and have fewer than 2 molecules uptakes per unit cell segment and couldn't fit the structural segment well.

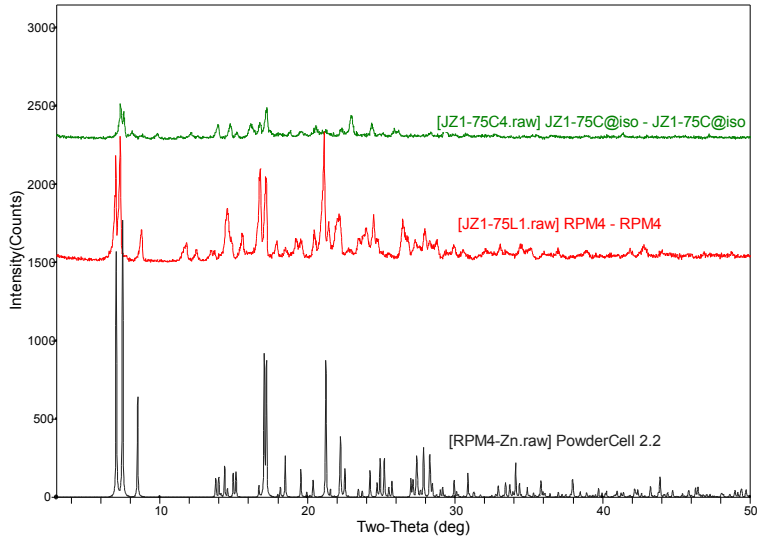

Figure 61. PXRD pattern of RPM4 from bottom to top: simulated (black), as made (red) and sample after adsorption experiments (green).

4.3.3 Conclusion.

Even though RPM3 and RPM4 are isotypic structures, the uptake of hydrocarbons and alcohols of RPM4 are much less than those on RPM3. This may be attributed to the more severe distortion of the RPM4 structure after the removal of guest molecules. This also changes the commensurate adsorption phenomenon in RPM4, in which only benzene, p-xylene and n-pentanol show commensurate adsorption.

Appendix A

Synthesis of Pt/AC doped Cu_3(tdpat) for catalysis

Note: A manuscript resulted from this work was accepted to the Journal of Catalysis.

Cu_3(tdpat) is a structure with Langmuir and BET surface area 2608 and 1938 m^2g^{-1} published by us. We are working to dope Platinum into the Cu_3(tdpat) structure using a chemical method to achieve H_2 spillover adsorption. It is expected that platinum in the MOFs may serve as a catalyst to cleave H_2 molecules and thus increase H_2 adsorption amount.

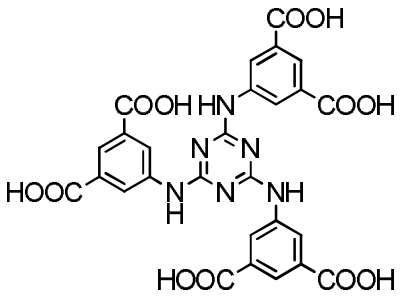

Figure A1. Structure of H_6tdpat

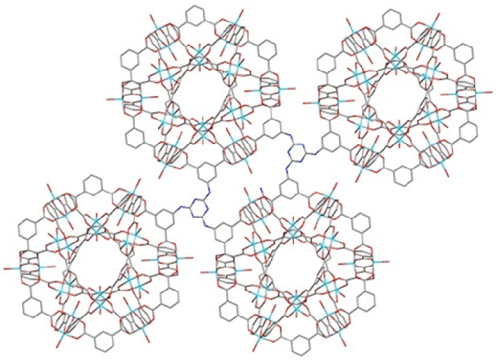

Figure A2. Portion of the structure of Cu-tdpat.

0.030 g (0.049 mmol) of H_6tdpat was dissolved in 2 mL DMA, 2 mL DMSO, 100 μL H_2O and 0.9 mL of HBF_4, excess 0.164 g (0.68 mmol) $Cu(NO_3)_2 \cdot 3H_2O$ and 1.8mg of Pt/Ac(with Pt 5wt%) (MOF: Pt/Ac ratio = 20:1) were then added. The mixture was first ultrasonicated for 0.5 hour and stirred overnight, then sealed in a small glass vial and heated at 85 °C for 3 days. After cooling down to room temperature, dark blue crystals were isolated and washed with DMA to give the final product Pt/Ac doped Cu_3(tdpat)$(H_2O)_3 \cdot 10H_2O \cdot 5$DMA (Pt/Ac@Cu-tdpat).

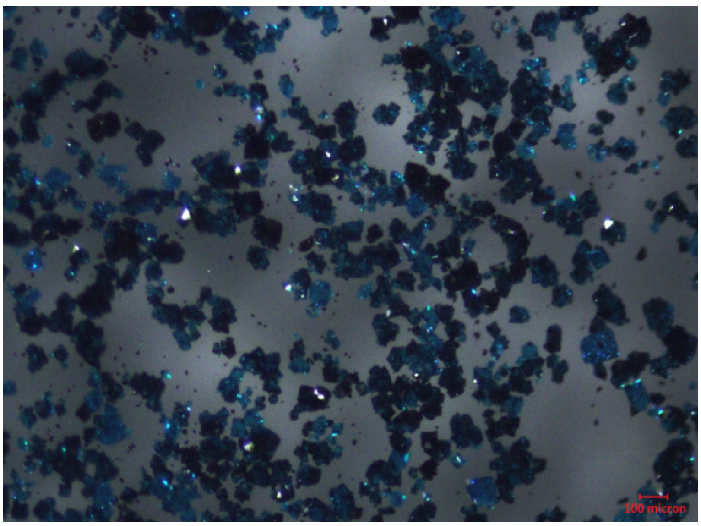

.

Figure A3. Crystal image of Pt/AC@Cu_3(tdpat)

The PXRD patterns (Figure A4) show the structure doesn't change after the Pt/AC doping on the Cu_3(tdpat) and solvent exchange. The TGA curve shows a flat plateau from 100 °C to 280 °C, which indicates the success of solvent exchange.

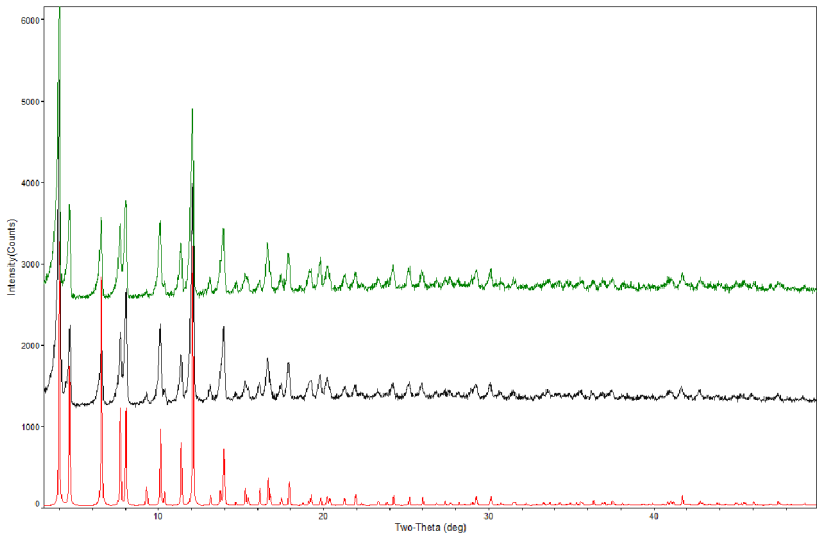

Figure A4. PXRD pattern of Pt/Ac@ Cu_3(tdpat) (from bottom to top: Simulated Cu_3(tdpat) pattern; as synthesized Pt/Ac@ Cu_3(tdpat) sample; sample after MeOH exchange).

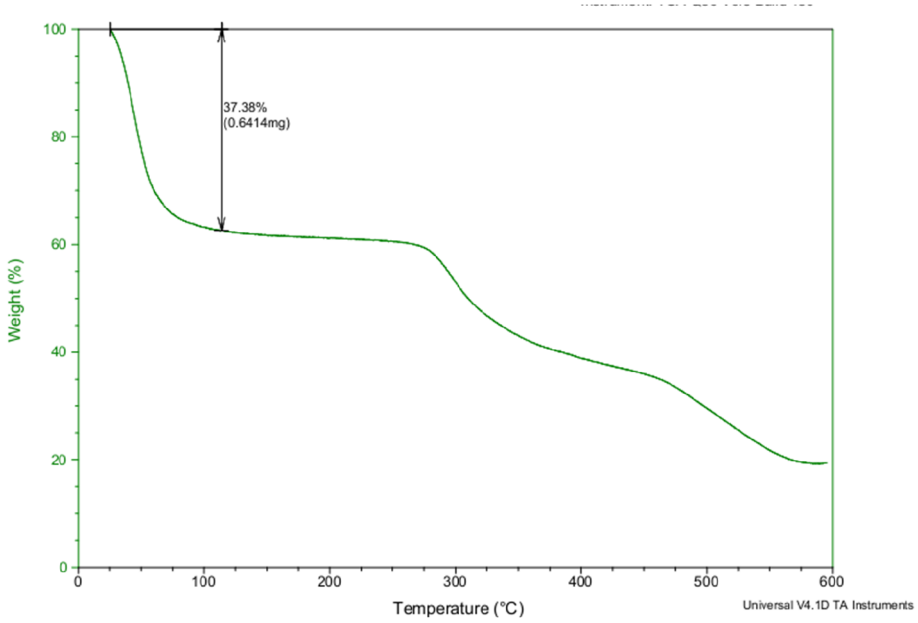

Figure A5. TGA plots of Pt/Ac@ Cu_3(tdpat) sample after MeOH-exchange sample.

From the adsorption data collected by our collaborator in Pennsylvania State University, the surface area of Pt/AC doped Cu_3(tdpat) is slightly smaller than that of pure Cu_3(tdpat). The room temperature low pressure H_2 adsorption uptake of Pt/AC@Cu_3(tdpat) is much higher than the pure Cu_3(tdpat) (Figure A6, PB-T for Pt/AC@Cu_3(tdpat) and T for pure Cu_3(tdpat)). This indicates the doping of Pt/AC on Cu_3(tdpat) via a prebridge method did improve the H_2 storage property.

Table A1. Surface area of Cu_3(tdpat) and Pt/AC@Cu_3(tdpat)

	Pt/AC@ Cu_3(tdpat)	**Pure Cu_3(tdpat)**
BET Surface Area (m^2/g)	1747.9157	1938

Langmuir Surface Area (m^2/g)	2014.5670	2608

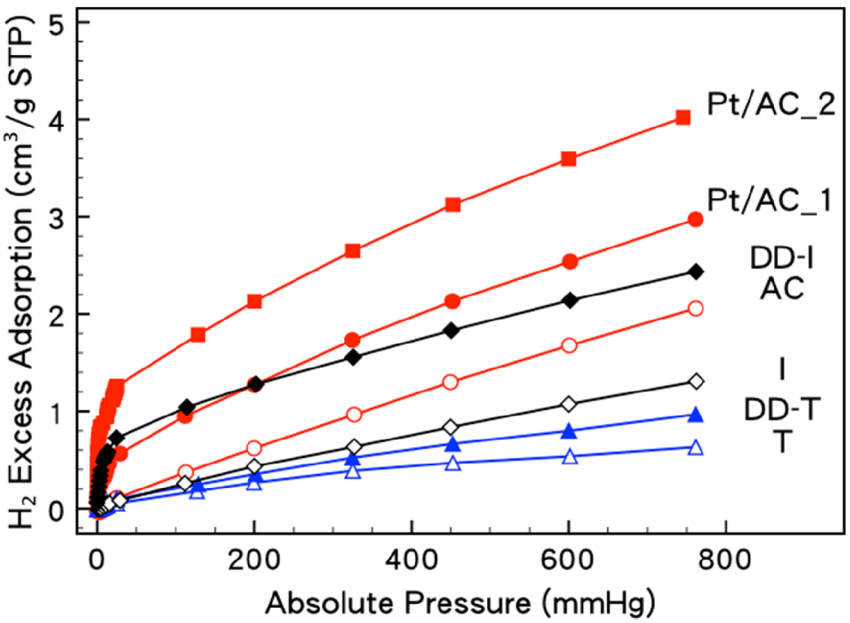

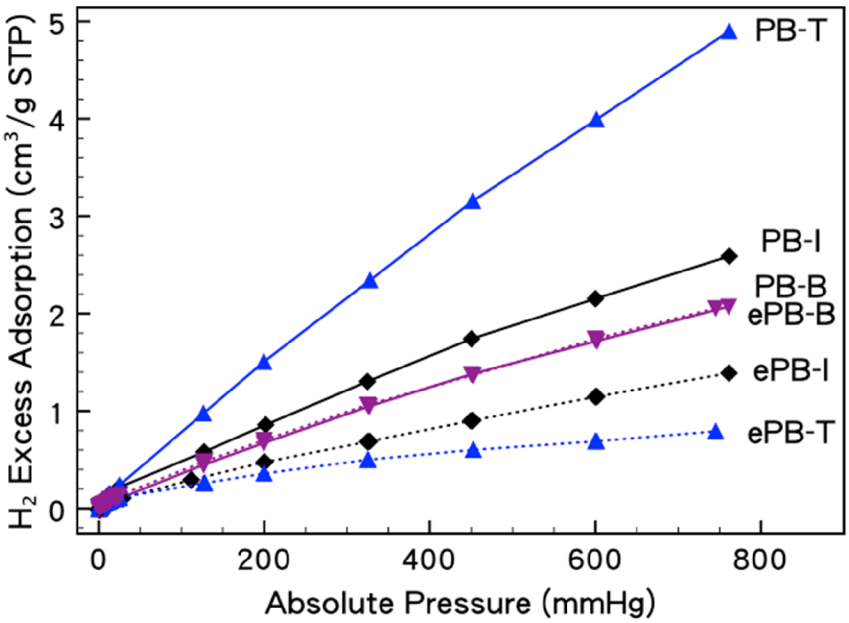

Figure A6. The hydrogen 300 K 1 bar isotherms of (A) AC (active cardon), **I** (IRMOF-8), **T** (Cu_3(tdpat)) with (solid legend) and without (empty legend) Pt direct doping, and (B) expected (dash line) PB-MOF (prebridged MOF) samples vs. experimental data (solid line). It is labeled as **I** (black ◆), **T** (blue ▲), and **B** (purple ▼). Data was collected by collaborator Chengyu Wang and Prof. Angela Lueking from Penn State University.

Ethylbenzene adsorption on CdMn(TPyP)($PW_{12}O_{40}$)

Note: A manuscript resulted from this work was accepted to the Journal of the American Chemical Society.

A new hybrid material named CdMn(TPyP)($PW_{12}O_{40}$) demonstrates remarkable capability for heterogeneous selective oxidation of alkylbenzenes with excellent product yields and 100% selectivity.[76] In order to examine if the reaction happens on the surface of the material or in the pores of the material, ethylbenzene was taken as an example to study its adsorption uptake on CdMn(TPyP)($PW_{12}O_{40}$). FigureA7 shows the structure and pore of the hybrid material.

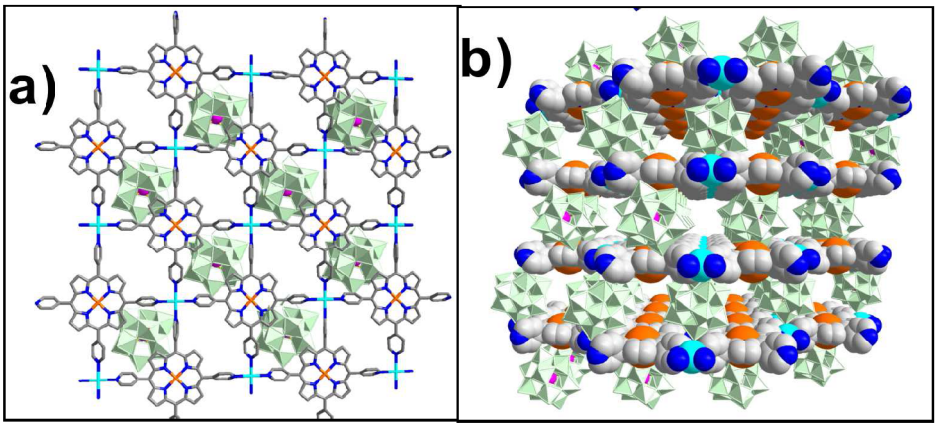

Figure A7. a) A view of the arrangement of two single layers of the lamellar framework of [Cd(DMF)2MnIII(DMF)2TPyP]n $^{3n+}$ and the polyanions of [PW12O40]3- down the *c* axis; b) A perspective view of the packing diagram of 1 along the [110] direction (Color scheme: MnIII: orange, Cd: cyan, {WO6}: green octahedra; P: purple, N: blue, C: gray; DMF molecules and hydrogen atoms are omitted for clarity). Reprinted with permission from Ref. 76. Copyright@2012 American Chemical Society

The ethylbenzene (EB) batch adsorption experiments were carried out at 25 C in 10 mL flask using binary solutions of EB (0.1 mL) in dry hexane as a solvent following a previously reported procedure[77,78]. A 10 mL of this solution is injected into an empty flask without adsorbent (as reference), and another 10 mL into a flask with 0.089 g of the adsorbent predried at 80 °C. After continuous shaking for 2h at room temperature, equilibrium is reached, and the supernatant of both flasks is tested by a GC equipped with a FID detector and HP-5 column. A series of standard binary solutions of EB in dry hexane with different EB bulk concentrations were also prepared and detected by GC. A standard curve with EB/n-hexane area ratio in GC data is obtained (Figure A8). The uptake of EB in the sample is calculated according the standard equation, which is 15.22 wt% at 25 °C. Reprinted with permission from Ref. 76. Copyright@2012 American Chemical Society.

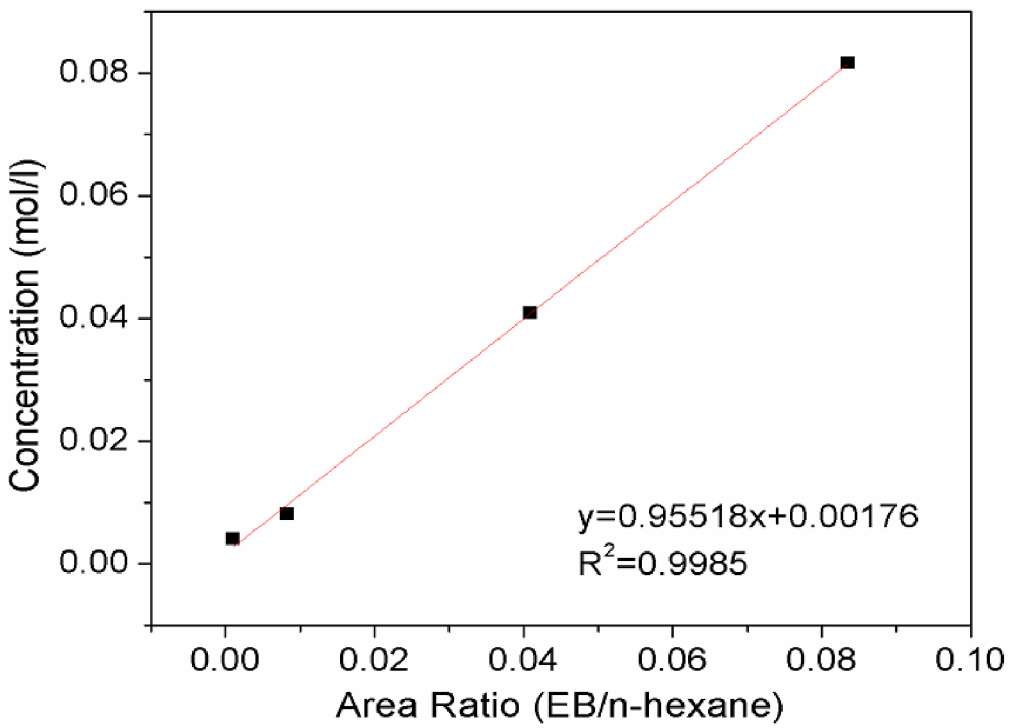

Figure A8. The standard curve of ethylbenzene and n-hexane binary solutions.The initial bulk concentration of ethylbenzene (EB) is 0.04 mol/L. Reprinted with permission from Ref. 76. Copyright@2012 American Chemical Society.

References

(1) Yabing He; Bin Li; O'Keeffe, M.; Chen, a. B. *Chem. Soc. Rev.* **2014**, *43*, 5618.

(2) Hoskins, B. F.; Robson, R. *J. Am. Chem. Soc.* **1990**, *112*, 1546.

(3) Abrahams, B. F.; Hoskins, B. F.; Robson, R. *J. Chem. Soc.-Chem. Commun.* **1990**, 60.

(4) Lee, J.; Farha, O. K.; Roberts, J.; Scheidt, K. A.; Nguyen, S. T.; Hupp, J. T. *Chem. Soc. Rev.* **2009**, *38*, 1450.

(5) Corma, A.; Garcia, H.; Xamena, F. X. L. I. *Chem. Rev.* **2010**, *110*, 4606.

(6) Yoon, M.; Srirambalaji, R.; Kim, K. *Chem. Rev.* **2012**, *112*, 1196.

(7) Kreno, L. E.; Leong, K.; Farha, O. K.; Allendorf, M.; Van Duyne, R. P.; Hupp, J. T. *Chem. Rev.* **2012**, *112*, 1105.

(8) Hu, Z.; Deibert, B. J.; Li, J. *Chem. Soc. Rev.* **2014**, *43*, 5815.

(9) Narayan, T. C.; Miyakai, T.; Seki, S.; Dinca, M. *J. Am. Chem. Soc.* **2012**, *134*, 12932.

(10) Sun, L.; Miyakai, T.; Seki, S.; Dinca, M. *J. Am. Chem. Soc.* **2013**, *135*, 8185.

(11) Li, Y. F.; Pang, A. Y.; Wang, C. J.; Wei, M. D. *J. Mater. Chem.* **2011**, *21*, 17259.

(12) Horcajada, P.; Gref, R.; Baati, T.; Allan, P. K.; Maurin, G.; Couvreur, P.; Ferey, G.; Morris, R. E.; Serre, C. *Chem. Rev.* **2012**, *112*, 1232.

(13) Horcajada, P.; Chalati, T.; Serre, C.; Gillet, B.; Sebrie, C.; Baati, T.; Eubank, J. F.; Heurtaux, D.; Clayette, P.; Kreuz, C.; Chang, J. S.; Hwang, Y. K.; Marsaud, V.; Bories, P. N.; Cynober, L.; Gil, S.; Ferey, G.; Couvreur, P.; Gref, R. *Nat. Mater.* **2010**, *9*, 172.

(14) Della Rocca, J.; Liu, D. M.; Lin, W. B. *Acc. Chem. Res.* **2011**, *44*, 957.

(15) Zhang, W.; Xiong, R. G. *Chem. Rev.* **2012**, *112*, 1163.

(16) Wang, C.; Zhang, T.; Lin, W. B. *Chem. Rev.* **2012**, *112*, 1084.

(17) Sun, C. Y.; Wang, X. L.; Zhang, X.; Qin, C.; Li, P.; Su, Z. M.; Zhu, D. X.; Shan, G. G.; Shao, K. Z.; Wu, H.; Li, J. *Nat. Commun.* **2013**, *4*, 2717.

(18) Stock, N.; Biswas, S. *Chem. Rev.* **2012**, *112*, 933.

(19) James, S. L. *Chem. Soc. Rev.* **2003**, *32*, 276.

(20) Zaworotko, M. J. *Nature Chem.* **2009**, *1*, 267.

(21) de Boer, W. D. A. M.; McGonigle, C.; Gregorkiewicz, T.; Fujiwara, Y.; Tanabe, S.; Stallinga, P. *Sci Rep-Uk* **2014**, *4*, 5235.

(22) Reshchikov, M. A.; Foussekis, M.; McNamara, J. D.; Behrends, A.; Bakin, A.; Waag, A. *J. Appl. Phys.* **2012**, *111*, 073106.

(23) Cui, Y. J.; Yue, Y. F.; Qian, G. D.; Chen, B. L. *Chem. Rev.* **2012**, *112*, 1126.

(24) Berezin, M. Y.; Achilefu, S. *Chem. Rev.* **2010**, *110*, 2641.

(25) KortUm, G. *Reflectance Spectroscopy Principles, Methods, Applications*; Springer-Verlag New York Inc. , 1969.

(26) Wendlandt, W. W.; Hecht, H. G. *Reflectance spectroscopy*; Interscience Publishers, 1966.

(27) SMITH, T.; M.A.; F.INsT.P; GUILD, J.; A.R.C.S.; F.INsT.P.; F.R.A.S. *TRANSACTIONS OF THE OPTICAL SOCIETY* **1931**, *33*, 73.

(28) CIE 1931 color space; Wikipedia: 2014.

(29) Eliseeva, S. V.; Bunzli, J. C. G. *Chem. Soc. Rev.* **2010**, *39*, 189.

(30) Reineke, S.; Lindner, F.; Schwartz, G.; Seidler, N.; Walzer, K.; Lussem, B.; Leo, K. *Nature* **2009**, *459*, 234.

(31) Allendorf, M. D.; Bauer, C. A.; Bhakta, R. K.; Houk, R. J. T. *Chem. Soc. Rev.* **2009**, *38*, 1330.

(32) D'Andrade, B. W.; Forrest, S. R. *Adv. Mater.* **2004**, *16*, 1585.

(33) Rivera, M. A.; UCDavis ChemWiki.

(34) Smet, P. F.; Parmentier, A. B.; Poelman, D. *Journal of the Electrochemical Society* **2011**, *158*, R37.

(35) Schubert, E. F.; Kim, J. K. *Science* **2005**, *308*, 1274.

(36) Life-Cycle Assessment of Energy and Environmental Impacts of LED Lighting Products; Department of Energy: 2012.

(37) Jang, H. S.; Jeon, D. Y. *Appl. Phys. Lett.* **2007**, *90*, 041906.

(38) Xie, R. J.; Hirosaki, N.; Sakuma, K.; Yamamoto, Y.; Mitomo, M. *Appl. Phys. Lett.* **2004**, *84*, 5404.

(39) Sheu, J. K.; Chang, S. J.; Kuo, C. H.; Su, Y. K.; Wu, L. W.; Lin, Y. C.; Lai, W. C.; Tsai, J. M.; Chi, G. C.; Wu, R. K. *IEEE Photonics Technol. Lett.* **2003**, *15*, 18.

(40) Dohner, E. R.; Hoke, E. T.; Karunadasa, H. I. *J. Am. Chem. Soc.* **2014**, *136*, 1718.

(41) Roushan, M.; Zhang, X.; Li, J. *Angew. Chem. Int. Ed.* **2012**, *51*, 436.

(42) Muthu, S.; Schuurmans, F. J. P.; Pashley, M. D. *IEEE J. Sel. Top. Quantum Electron.* **2002**, *8*, 333.

(43) LED BASICS; Department of Energy: 2014.

(44) Pimputkar, S.; Speck, J. S.; DenBaars, S. P.; Nakamura, S. *Nat. Photonics* **2009**, *3*, 179.

(45) Allen, S. C.; Steckl, A. J. *Appl. Phys. Lett.* **2008**, *92*, 143309.

(46) Ye, S.; Xiao, F.; Pan, Y. X.; Ma, Y. Y.; Zhang, Q. Y. *Mater. Sci. Eng. R-Rep* **2010**, *71*, 1.

(47) Wang, M. S.; Guo, S. P.; Li, Y.; Cai, L. Z.; Zou, J. P.; Xu, G.; Zhou, W. W.; Zheng, F. K.; Guo, G. C. *J. Am. Chem. Soc.* **2009**, *131*, 13572.

(48) He, J.; Zeller, M.; Hunter, A. D.; Xu, Z. T. *J. Am. Chem. Soc.* **2012**, *134*, 1553.

(49) Luo, F.; Wang, M. S.; Luo, M. B.; Sun, G. M.; Song, Y. M.; Li, P. X.; Guo, G. C. *Chem. Commun.* **2012**, *48*, 5989.

(50) Sava, D. F.; Rohwer, L. E. S.; Rodriguez, M. A.; Nenoff, T. M. *J. Am. Chem. Soc.* **2012**, *134*, 3983.

(51) Zhang, X. J.; Ballem, M. A.; Hu, Z. J.; Bergman, P.; Uvdal, K. *Angew. Chem. Int. Ed.* **2011**, *50*, 5728.

(52) Dang, S.; Zhang, J. H.; Sun, Z. M. *J. Mater. Chem.* **2012**, *22*, 8868.

(53) Rao, X. T.; Huang, Q.; Yang, X. L.; Cui, Y. J.; Yang, Y.; Wu, C. D.; Chen, B. L.; Qian, G. D. *J. Mater. Chem.* **2012**, *22*, 3210.

(54) Liu, Z. F.; Wu, M. F.; Wang, S. H.; Zheng, F. K.; Wang, G. E.; Chen, J.; Xiao, Y.; Wu, A. Q.; Guo, G. C.; Huang, J. S. *Journal of Materials Chemistry C* **2013**, *1*, 4634.

(55) Liu, Y.; Pan, M.; Yang, Q. Y.; Fu, L.; Li, K.; Wei, S. C.; Su, C. Y. *Chem. Mater.* **2012**, *24*, 1954.

(56) Rybak, J. C.; Hailmann, M.; Matthes, P. R.; Zurawski, A.; Nitsch, J.; Steffen, A.; Heck, J. G.; Feldmann, C.; Gotzendorfer, S.; Meinhardt, J.; Sextl, G.; Kohlmann, H.; Sedlmaier, S. J.; Schnick, W.; Muller-Buschbaum, K. *J. Am. Chem. Soc.* **2013**, *135*, 6896.

(57) Zhang, H. B.; Lin, P.; Shan, X. C.; Du, F. L.; Li, Q. P.; Du, S. W. *Chem. Commun.* **2013**, *49*, 2231.

(58) Zhang, Y. H.; Li, X.; Song, S. *Chem. Commun.* **2013**, *49*, 10397.

(59) Wei, Y. Q.; Li, Q. H.; Sa, R. J.; Wu, K. C. *Chem. Commun.* **2014**, *50*, 1820.

(60) Critical Materials Strategy; Department of Energy: 2011.

(61) Kulprathipanja, S. *Zeolites in Industrial Separation and Catalysis*; Wiley-VCH, 2010.

(62) Li, J. R.; Kuppler, R. J.; Zhou, H. C. *Chem. Soc. Rev.* **2009**, *38*, 1477.

(63) DeCoste, J. B.; Peterson, G. W. *Chem. Rev.* **2014**, *114*, 5695.

(64) Yabing He; Wei Zhou; Qian, G.; Chen, B. *Chem. Soc. Rev.* **2014**, *43*, 5657.

(65) Getman, R. B.; Bae, Y. S.; Wilmer, C. E.; Snurr, R. Q. *Chem. Rev.* **2012**, *112*, 703.

(66) Suh, M. P.; Park, H. J.; Prasad, T. K.; Lim, D. W. *Chem. Rev.* **2012**, *112*, 782.

(67) Zhang, Z. J.; Zhao, Y. G.; Gong, Q. H.; Li, Z.; Li, J. *Chem. Commun.* **2013**, *49*, 653.

(68) Sumida, K.; Rogow, D. L.; Mason, J. A.; McDonald, T. M.; Bloch, E. D.; Herm, Z. R.; Bae, T. H.; Long, J. R. *Chem. Rev.* **2012**, *112*, 724.

(69) Li, J. R.; Sculley, J.; Zhou, H. C. *Chem. Rev.* **2012**, *112*, 869.

(70) Wu, H. H.; Gong, Q. H.; Olson, D. H.; Li, J. *Chem. Rev.* **2012**, *112*, 836.

(71) Gregg, S. J.; Sing, K. S. W. *Adsorption, Surface Area and Porosity*; Academic Press, 1982.

(72) Xu, R.; Pang, W.; Yu, J.; Huo, Q.; Chen, J. *Chemistry of Zeolites and Related Porous Materials: Synthesis and Structure (Cambridge, MA, United States)*; John Wiley & Sons (Asia) Pte Ltd, 2007.

(73) Bansal, R. C.; Goyal, M. *Activated Carbon Adsorption*; CRC Press Taylor & Francis Group 2005.

(74) Z. Hu, J. Z. **2014**, under preparation.

(75) Zhang, J. M.; Wu, H. H.; Emge, T. J.; Li, J. *Chem. Commun.* **2010**, *46*, 9152.

(76) Zou, C.; Zhang, Z. J.; Xu, X.; Gong, Q. H.; Li, J.; Wu, C. D. *J. Am. Chem. Soc.* **2012**, *134*, 87.

(77) Maes, M.; Vermoortele, F.; Alaerts, L.; Denayer, J. F. M.; De Vos, D. E. *Journal of Physical Chemistry C* **2011**, *115*, 1051.

(78) Alaerts, L.; Kirschhock, C. E. A.; Maes, M.; van der Veen, M. A.; Finsy, V.; Depla, A.; Martens, J. A.; Baron, G. V.; Jacobs, P. A.; Denayer, J. E. M.; De Vos, D. E. *Angew. Chem. Int. Ed.* **2007**, *46*, 4293.